Extending the Reach of Collider Searches for Dark Matter

SOFIE NORDAHL ERNER

Extending the Reach of Collider Searches for Dark Matter

Distinguishing Invisible States at Belle II

& ANUBIS Sensitivity Studies

Sofie Nordahl Erner

A Thesis presented for the degree of
Doctor of Philosophy

Institute for Particle Physics Phenomenology
Department of Physics
Durham University
United Kingdom

31st of March 2024

Extending the Reach of Collider Searches for Dark Matter

Distinguishing Invisible States at Belle II

& ANUBIS Sensitivity Studies

Sofie Nordahl Erner

Submitted for the degree of Doctor of Philosophy

31st of March 2024

Abstract: The Standard Model (SM) has done an excellent job at predicting the outcomes of experiments, but many questions remain unanswered. Neutrino masses and the existence of dark matter (DM) are two of these, both of which are not included in the Standard Model. The particle physics community, together with the rest of the world, faces difficult decisions and obstacles presented by the increasing threat of climate change. Making the most of the experiments, which have already been built, is therefore an important endeavour for exploiting all possibilities of New Physics (NP). This thesis presents two projects which are opportunities to extend the reach of two existing particle colliders in the search for dark matter.

The searches for dark matter particles at the ATLAS detector at the LHC have a limited reach for long-lived Particles (LLPs) due to the finite width of the detector. The ANUBIS detector will extend these searches through measuring decays in the cavern above ATLAS. SET-ANUBIS sets out to calculate the sensitivity projections for the detector for various long-lived particle models. In this thesis, the development of the sensitivity study, with the considerations and choices made, are presented. The specific case of heavy neutral leptons is used for the development and is discussed.

Considering a wider dark sector for which an invisible state is the portal, the production of the invisible state X together with a photon, $e^+e^- \to \gamma + X$, at electron positron colliders is one of the strongest searches for $m_X \in [0.1, 10]$ GeV. This thesis presents measurement strategies that can detect the spin of the invisible state as well as the underlying production mechanism. Based on the angular distribution of the final state photon, the cross-sections for polarised initial states and the photon polarisation, the measurement strategy can be used to identify whether the invisible state is a dark photon or an axion-like particle (ALP). The results are compared with a detailed analysis of the Standard Model background, and the sensitivity reach for searches for axion-like particles and dark photons at Belle II are calculated. It is found that the sensitivity of the ALP coupling the electrons can be improved when both incoming beams are polarised.

Contents

List of Figures

List of Tables

Declaration

The work in this thesis is based on research carried out in the Department of Physics at Durham University. No part of this thesis has been submitted elsewhere for any degree or qualification.

Chapter 5 is based on yet-to-be-published work undertaken with the ANUBIS collaboration; Anna Jane Mullin and Paul Nathaniel Swallow at Cambridge University and Théo Reymermier at Université de Lyon. SET-ANUBIS is a combined effort of the aforementioned people, where the author of this thesis was responsible for the theoretical inputs, and implementation of long-lived particle models. This included the calculations of branching ratios for both production and decay modes of the long-lived particles. Anna Mullin implemented the ANUBIS geometry and selection cut, and Paul Swallow and Théo Reymermier modified Pythia to include meson production and decays.

Chapter 6 is based on work undertaken in collaboration with Martin Bauer entitled "*How to measure the spin of invisible states in* $e^+e^- \to \gamma + X$" [1]. This thesis author's contributions consisted of the helicity amplitude calculations, performing simulations, and writing analyses for these results.

Acknowledgements

To begin with, I would like to thank my supervisor, Martin Bauer, for his support, guidance, and taking me on as a student halfway through my PhD.

The cohort of PhD students at the IPPP throughout my stay have been integral to my PhD, together with the pillars of the IPPP, whom the entire institute would fall apart without, Trudy and Joanne. My collaborators Anna Mullin, Paul Swallow and Théo Reymermier of the ANUBIS collocation, whom I have greatly enjoyed working with. I am saddened to leave so soon after joining. In particular, I would like to thank Guillaume Rostagni, Lois Flower, Oscar Braun-White, and Paul Swallow for reading my thesis.

I would like to thank Anke Biekötter for her help and support, and my friends Antonio, Leah, and Elliot, whom I would never have had the courage to change supervisor without.

Sidst men ikke mindst, jeg vil gerne takke min familie for deres støtte. For at lade mig følge min drøm, selvom det betød, at jeg har boet i et andet land i næsten 10 år. Tusind tak for at prøve at lytte og forstå mit arbejde.

"Pick a Star on the Dark Horizon and Follow the Light"

— from *The Call* by Regina Spektor

Abbreviations, Notations, & Physical Constants

The following list describes the abbreviations, units, and symbols used within the body of this thesis. Unless stated otherwise, throughout this thesis natural units, $c = \hbar = 1$, will be used. The values and units of the constants were found at [2].

Physical Constants

α_{EW}	Fine-structure constant	$7.297\,352\,569\,3 \times 10^{-3}$
$\sin\theta_w$	Weinberg angle	$0.227\,736$
c	Speed of light in a vacuum	$299\,792\,458\,\mathrm{m\,s^{-1}}$
G_F	Fermi coupling constant	$1.166\,378\,7 \times 10^{-5}\,(\hbar\mathrm{c})^3/\mathrm{GeV}^2$
h	Planck constant	$6.62607015 \times 10^{-34}\,\mathrm{J\,s}$
m_e	Electron mass	$0.510\,998\,950\,00\,\mathrm{MeV/c^2}$
m_H	Higgs boson mass	$125\,\mathrm{GeV/c^2}$
m_T	Top quark mass	$172\,\mathrm{GeV/c^2}$
m_Z	Z^0 boson mass	$91.1876\,\mathrm{GeV/c^2}$

Abbreviations

BSM	Beyond Standard Model

CDF Cumulative Density Function

CERN European Organization for Nuclear Research

CL Confidence Level

CMB Cosmic Microwave Background

CMS Centre-of-mass

DM Dark Matter

ECL Electromagnetic Calorimeter

EM Electromagnetic

EoM Equations of Motion

EW Electroweak

EWSB Electroweak symmetry breaking

GWS Glashow-Weinberg-Salam

HCAL Hadronic Calorimeter

IP Interaction Point

LHC Large Hadron Collider

LIPS Lorentz-invariant phase space

LLP Long-Lived Particles

LO Leading order

MC Monte Carlo

MS Muon Spectrometer

NLO Next to leading order

NP New Physics

PDF Parton Distribution Function

PMNS Pontecorvo-Maki-Nakagawa-Sakata

QCD Quantum Chromodynamics

RHN Right-Handed Neutrino

SM Standard Model

SSB Spontaneous Symmetry Breaking

SUSY Supersymmetry

Notation

h.c. Hermitian conjugate

a^μ	Four-vector	$\left(a^0, a^1, a^2, a^3\right) = (E, x, y, z)$
$g_{\mu\nu}$	Metric tensor	Diagonal$(1, -1, -1, -1)$

Chapter 1

Introduction

In the 1970s, the *Standard Model* (SM) was formulated as the theory for the fundamental particles and their interactions. It combined the theories at the time, creating a common language between particle physicists across the globe. The resulting model described particles which had already been experimentally observed, but also several that were only theorised and had yet to be discovered. In the following years, the $W-$ and $Z-$bosons were detected in 1983, whereas the heaviest quark, the top quark, was discovered in 1995, and finally the last fundamental particle in 2012 was the Higgs boson [3].

Experiments over the last decades have done an excellent job at confirming the Standard Model, but there are a number of issues that are still unexplained or not included; neutrino masses and oscillations, *dark matter* (DM), cosmological inflation, and many more. Neutrinos are observed to oscillate between their different flavours, which implies that they must have masses, contradicting the Standard Model, see section 2.5 [4]. Through evidence presented below, it is known that a large proportion of the matter in the universe is unaccounted for by the Standard Model. The *Cosmic Microwave Background* (CMB) consists of photons emitted during *recombination*, when the universe was cold enough for neutral atoms to form [5]. From the CMB, it is observed that the universe exponentially inflated in the early times, and is experiencing accelerated expansion currently. Inflation will not be described further

in this thesis, for a review see [6]. The densities of matter, radiation, and dark energy, which infer the existence of DM, are extracted from the CMB [5], see the next section for further detail.

Many ideas have been proposed to solve each of these problems, though few manage to explain all, and none have been experimentally proven yet. In general, most of the ideas describe *New Physics* (NP) or *Beyond the Standard Model* (BSM) which differs from the Standard Model through, for example, the introduction of new particles or interactions. A category of New Physics is *Effective-Field Theories* (EFTs) which have a broad application, even when only considering Standard Model particles (SMEFT) [7]. Introducing new interactions and/or particles at energy scales much larger than what is currently experimentally possible to probe, EFTs provide a framework for seeing how these effect smaller energy scales [8]. See section 4.2 for further detail.

The remainder of this thesis is structured as follows. At first, an introduction to the evidence for dark matter and particle colliders is presented. Chapter 2 describes the Standard Model theory relevant for the remaining chapters, in particular the particle content, the Higgs mechanism, and the theory of weak interactions. Chapter 3 contains a brief introduction to particle colliders with their layout and components, followed by an overview of New Physics searches at colliders. In particular the Belle II and ATLAS detectors are the two main detectors considered. The principles of dark matter models will be presented in chapter 4, including the theories of the dark photon, axion-like particles, and heavy neutral leptons. Building on the foundation of general New Physics searches, the specifics of dark matter searches at particle colliders are described. Chapter 5 outlines the sensitivity studies carried out for the ANUBIS detector at CERN. A brief review of the detector setup, together with the considerations gone into the development of the SET-ANUBIS software, are included. The issue of distinguishing different dark matter signals in colliders is addressed in chapter 6, where the polarisation of the incoming beams and the outgoing photon are utilised to determine the spin of invisible states in $e^+e^- \to \gamma + X$.

1.1 Evidence for Dark Matter

Throughout the years evidence has been accumulating, which all points to that fact that 84.4% of the total matter density in the universe has an unknown constitution [2].

This has been observed through rotation curves of spiral galaxies, where the rotational speed of the galaxy is expected to fall as $r^{-1/2}$ with the distance from the galactic centre. However, the speed is found to be constant instead, implying that the parts of the spiral galaxies visible to us are surrounded by an invisible halo of matter. The distribution of masses can also be infered using gravitational lensing, where it is observed that light is bent around large masses that are not luminous. Merging clusters provide another example, where it is observed that the clusters must contain large amounts of weakly to non-interacting matter [9].

The evidence presented above can be explained by a lack in the understanding of *general relativity*. But the following will outline why dark matter cannot be fully explained by modifying gravity. The universe can be described as containing different fluids; matter (dark and *baryonic* [1]), radiation (relativistic particles such as photons and neutrinos), and unknown sources of negative pressure, called *dark energy*. Throughout the history of the universe, these three different components have each dominated at different times as they each scale differently with the expansion of the universe [5]. The early universe was *radiation-dominated*, a gas of relativistic particles, but as the universe cooled down non-relativistic matter eventually started to dominate, *matter-domination* [2]. Today, the total energy density of the universe is dominated by dark energy.

The formation of the stellar objects observed today, known as *structure formation*, occurred mainly during matter-domination. During this formation, the balance between the attraction from the gravitational interactions between matter and the

[1] In the field of astronomy, baryonic matter does not only refer to baryons, such as protons and neutrons, but includes all visible particles [2].

repulsion from the expansion of the universe can be disturbed. For example, if neutrinos, which are relativistic particles, were to explain all of the dark matter observed, the stellar structures in the universe would look significantly different. Therefore, dark matter cannot be radiation and must be matter with non-relativistic velocities, also known as *cold* dark matter [5].

There are several production mechanisms for dark matter, where the two most commonly used are *freeze-out* and *freeze-in*. Generally, freeze-out has the dark matter existing in the universe in great quantities that then decrease over time. The number density is determined by the production of dark matter from the annihilation of lighter particles and the reverse process of dark matter annihilating into lighter particles. As the universe expands and cools, these eventually balance out, and the number density becomes fixed. Freeze-in initially has a low number of DM particles, but the quantity increases over time through production by annihilation of Standard Model particles until an equilibrium is again reached [10].

The *local density* of our neighbourhood of the universe is measured by a range of methods to be $\rho_0 = [0.2, 1.5]$ GeV/cm^3, see [11] for a review. Regardless of the production mechanism, number of dark particles, and interactions in the dark sector, the predicted dark matter population cannot exceed the observed quantity. Hence, this restricts large areas of parameter space for proposed models, as it is possible for more than one model to make up the dark matter observed, hence only parameters that underestimate the density are allowed.

From the observations described, conclusions can be drawn about the properties of dark matter. Firstly, it must have minimal electric charge, known as *milli-electric* charge, given by the upper bounds depending on the dark matter mass

$$Q_{\mathrm{DM}} \leq 3.5 \times 10^{-7} \left(\frac{m_{\mathrm{DM}}}{\mathrm{GeV}}\right)^{0.58} e \qquad \text{for} \qquad m_{\mathrm{DM}} > 1\,\mathrm{GeV}\,, \tag{1.1.1}$$

$$Q_{\mathrm{DM}} \leq 4.0 \times 10^{-7} \left(\frac{m_{\mathrm{DM}}}{\mathrm{GeV}}\right)^{0.35} e \qquad \text{for} \qquad m_{\mathrm{DM}} < 1\,\mathrm{GeV}\,. \tag{1.1.2}$$

Here e is the electric charge of the electron and m_{DM} the dark matter mass. Hence,

the interactions between dark matter and charged particles in the Standard Model must be limited [2]. From merging clusters, the interaction of dark matter with itself is restricted to be

$$\frac{\sigma_{\mathrm{DM-DM}}}{m_{\mathrm{DM}}} < 0.47 \frac{\mathrm{cm}^2}{g} \simeq 0.84 \frac{\mathrm{barn}}{\mathrm{GeV}}\,, \tag{1.1.3}$$

for the cross-section of DM-DM interactions $\sigma_{\mathrm{DM-DM}}$ [2].

In general, the evidence presented above only require DM particles to gravitationally interact with the Standard Model. It is therefore possible, that this is the only interaction between the SM and the dark sector. This greatly restricts the methods for detecting dark matter, and it is therefore often assumed that dark matter interacts weakly with the SM [2].

1.2 Colliders

A powerful category of experiments used to examine particle physics are *particle colliders*, which collide particles together at high speeds and observe the resultant showers of produced particles. The first prototypes of colliders were built in the 1960s by the Midwestern Universities Research Association (MURA). Since then, colliders have become bigger and bigger in order to collide particles with increasing energies, allowing for the production of particles with larger masses [3].

Scientists have a duty to consider the wider community and be responsible for their choices and actions, whilst using their resources to progress the scientific knowledge with consideration. The construction of particle colliders and detectors is a resource-intensive endeavour, has a significant environmental impact, and their power-consumption when running is extensive. Therefore, existing experiments should be maximally utilised to explore all possibilities and reduce future environmental impact. This thesis addresses this through the introduction of two methods that increase the reach and effectiveness of two different particle detector experiments.

Chapter 2

The Standard Model

2.1 Introduction

The Standard Model is described by the symmetry group $SU(3)_c \times SU(2)_L \times U(1)_Y$ where the group represents *Quantum Chromodynamics* (QCD) (also known as the strong interactions), the weak interactions, and hypercharge respectively. The parts of the SM covered in this thesis are contained in the Lagrangian,

$$\mathcal{L}_{\text{SM}} \supset \mathcal{L}_{\text{gauge}} + \mathcal{L}_{\text{Fermion}} + \mathcal{L}_{\text{Yukawa}} + \mathcal{L}_{\text{Higgs}} \,, \tag{2.1.1}$$

each described in the following sections where section 2.2 will briefly outline the particles in the Standard Model. Section 2.3 contains the theoretical motivations and detail of the *Higgs mechanism*, which subsequently introduces the *Glashow-Weinberg-Salam* (GWS) theory in section 2.4. The detail of neutrino physics can be found in section 2.5, and finally the calculations of amplitudes and particle decays are reviewed in section 2.6.

2.2 Particle Content

Firstly, the gauge bosons and fermions in the Standard Model and the couplings between the two will be presented. The concepts of spin, helicity, and polarisation

for both groups of particles will then be introduced, followed by the issue of their masses.

2.2.1 Gauge Fields

Each of the three symmetry groups in the SM have a number of associated gauge fields which are spin-1 particles called *bosons*. $SU(3)_c$ has eight called *gluons* (g), the c stands for colour and therefore any particle which interacts with gluons is called *coloured* and have an associated colour charge, either red, blue, or green [12] As the strong interactions of QCD are not relevant for the remainder of this thesis, they will not be described in any further detail.

The combined $SU(2)_L \times U(1)_Y$ group describes the *electroweak* (EW) gauge symmetry where L stands for left-handed, which will be discussed further in section 2.4, and Y represents *hypercharge*. The group has four associated fields; three from $SU(2)_L$,

$$W^a_{\mu\nu} = \partial_\mu W^a_\nu - \partial_\nu W^a_\mu + g\epsilon^{abc} W^b_\mu W^c_\nu \,, \tag{2.2.1}$$

and an additional field from $U(1)_Y$,

$$B_{\mu\nu} = \partial_\mu B_\nu - \partial_\nu B_\mu \,. \tag{2.2.2}$$

Here $a \in \{1, 2, 3\}$, ϵ^{abc} is the Levi-Civita tensor, and g the coupling constant to $SU(2)_L$. The four gauge fields will later be shown in section 2.4 to become the *photon* (γ), $W^\pm$, and Z bosons through *spontaneous symmetry breaking* (SSB). Together with the gluon, the four gauge fields can be seen on the right column in Figure 2.1 [13]. Using the $SU(2)_L \times U(1)_Y$ gauge fields, the *covariant derivative* is constructed,

$$D_\mu = \partial_\mu - igW^a_\mu \tau^a - ig' Y B_\mu \,, \tag{2.2.3}$$

for coupling constants g and g' to $SU(2)_L$ and $U(1)_Y$ respectively, $SU(2)_L$ generators τ^a, and the hypercharge quantum number Y.

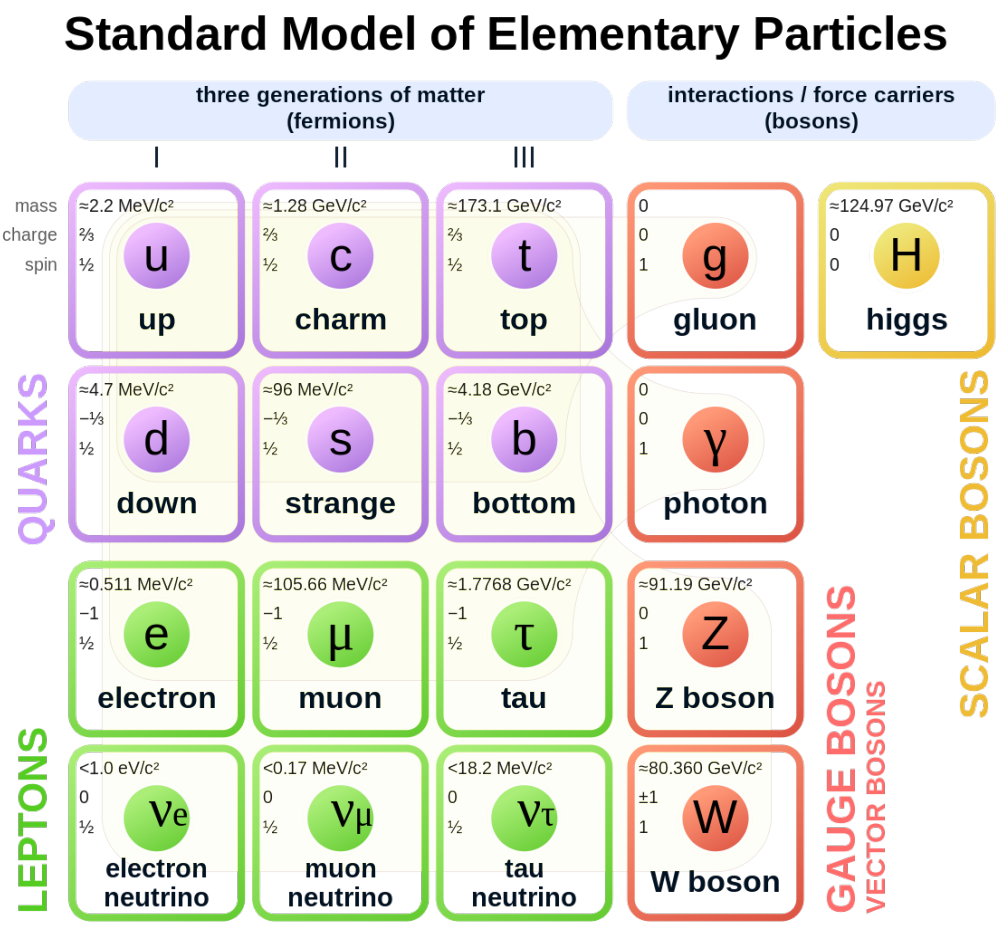

Figure 2.1: Depiction of all particles in the Standard Model with their respective quantum numbers (from [14]).

The Lagrangian with the kinetic terms for the gauge fields is constructed,

$$\mathcal{L}_{\text{gauge}} = -\frac{1}{4}G^a_{\mu\nu}G^{a\mu\nu} - \frac{1}{4}W^a_{\mu\nu}W^{a\mu\nu} - \frac{1}{4}B_{\mu\nu}B^{\mu\nu}\,, \tag{2.2.4}$$

where $G^a_{\mu\nu}$ are the gluon fields [15].

2.2.2 Fermions

The main contributions of the matter in the SM are spin-$\frac{1}{2}$ particles known as *fermions* which are categorised by their couplings to $SU(3)_c \times SU(2)_L \times U(1)_Y$. Fermions which do not couple through the strong interaction are called *leptons* (l) and consist of the electron e, muon μ, tau τ, and their neutrino counterparts $\nu_{e,\mu,\tau}$. The strongly interacting fermions are *quarks* (q) of which there are six; up, down,

charm, strange, top, and bottom [13]. The quarks and leptons are grouped by their *flavours*,

$$u = \{u, c, t\}, \quad d = \{d, s, b\}, \quad e = \{e, \mu, \tau\}, \quad \text{and} \quad \nu = \{\nu_e, \nu_\mu, \nu_\tau\}\,, \tag{2.2.5}$$

where u and d are referred to as *up* and *down* type quarks respectively.

The flavours are grouped together into $i \in \{1, 2, 3\}$ families or generations represented by the columns labelled "|", "||", and "|||" in Figure 2.1. All fermions have a corresponding antiparticle, and the quarks a colour charge due to their interactions with $SU(3)_c$.

Fermion fields can be constructed as *Dirac spinors* which can be split into left- and right-handed parts,

$$\psi = \psi_L + \psi_R = P_L\psi + P_R\psi\,, \tag{2.2.6}$$

for *projection operators* $P_{R/L} = \frac{1}{2}\left(1 \pm \gamma^5\right)$, and left- and right-handed Chiral Dirac spinors ψ_L and ψ_R [13]. The *chirality* of a fermion field is described by its handedness [16].

Coupling to Gauge Fields

Due to their interactions with $SU(2)_L$, fermions can be represented as doublets and singlets,

$$L_L^i = \begin{pmatrix} \nu_L^i \\ e_L^i \end{pmatrix}, \qquad e_R^i, \qquad \nu_R^i, \qquad Q_L^i = \begin{pmatrix} u_L^i \\ d_L^i \end{pmatrix}, \qquad u_R^i, \qquad d_R^i\,, \tag{2.2.7}$$

where L/R refer to the chirality of the field, left- and right-handed fermions respectively, and u^i, d^i, ν^i, and e^i are as defined in eq. (2.2.5) [16]. L_L and Q_L transform as the *fundamental* representation of $SU(2)_L$, the simplest representations of the group, and are therefore 2-dimensional vectors [12].

The couplings between the fermion and gauge fields, excluding the couplings to

gluons, are described by Lagrangian,

$$\begin{aligned}\mathcal{L} \supset \; & i\bar{L}_L^i \left(\not{\partial} - ig\not{W}^a\tau^a - ig'Y_L\not{B}\right) L_L^i + i\bar{Q}_L^i \left(\not{\partial} - ig\not{W}^a\tau^a - ig'Y_Q\not{B}\right) Q_L^i \\ & + i\bar{e}_R^i \left(\not{\partial} - ig'Y_e\not{B}\right) e_R^i + i\bar{\nu}_R^i \left(\not{\partial} - ig'Y_\nu\not{B}\right) \nu_R^i \\ & + i\bar{u}_R^i \left(\not{\partial} - ig'Y_u\not{B}\right) u_R^i + i\bar{d}_R^i \left(\not{\partial} - ig'Y_d\not{B}\right) d_R^i \,,\end{aligned} \tag{2.2.8}$$

for the covariant derivative in eq. (2.2.3) and *slash*-notation ($\not{p} = p_\mu\gamma^\mu$) [16]. Here the individual coupling strengths between the fields and the hypercharge group, $U(1)_Y$, also referred to as the *charge*, are displayed using Y_f for $f \in \{e, \nu, u, d\}$. The values of the charges can be found in Table 2.1, where it is worth noting that the right-handed neutrino has zero couplings to both $SU(2)_L$ and $U(1)_Y$ [12]. They have also not been experimentally observed yet, but are included here for completeness. Neutrinos will be described further in sections 2.5 and 4.2.4. All other fermions couple to the hypercharge gauge boson [16].

Field	L_L^i	e_R^i	ν_R^i	Q_L^i	u_R^i	d_R^i
$SU(3)_c$	-	-	-	□	□	□
$SU(2)_L$	□	-	-	□	-	-
$U(1)_Y$	$-\frac{1}{2}$	-1	0	$\frac{1}{6}$	$\frac{2}{3}$	$-\frac{1}{3}$

Table 2.1: The charges of the fermion fields for each SM gauge group, □ symbolises that the field transforms in the fundamental representation [16].

All together, the Lagrangian with the fermion sector kinetic terms can be constructed,

$$\mathcal{L}_{\text{Fermion}} = \sum_{\text{quarks}} i\bar{q}\gamma^\mu D_\mu q + \sum_{\psi_L} i\bar{\psi}_L\gamma^\mu D_\mu\psi_L + \sum_{\psi_R} i\bar{\psi}_R\gamma^\mu D_\mu\psi_R \,, \tag{2.2.9}$$

for covariant derivatives D_μ [15].

2.2.3 Hadrons

For low energies, quarks have small momenta and hence the potential energy, arising from the exchange of gluons, is larger than their kinetic energy. They are therefore

attracted to each other and form bound states, which is called *colour confinement*. These colour-neutral bound states of quarks are called *hadrons*, where *mesons* are quark-antiquark pairs and *baryons* have three quarks [1] [16]. The masses of hadrons are not just the sum of the masses of its constituents, but also include their binding energies. The lightest mesons are the *pions*, either charged π^+ and π^-, or neutral π^0. Whereas, the lightest baryons are the proton (uud) and neutron (udd). The constituents of hadrons are called *partons*.

Mesons have quantum numbers $J^{PC} = 0^{-+}$ (Pseudo-scalars) and $J^{PC} = 1^{--}$ (Pseudo-vectors) with relation to representations of the subgroup $SU(3)_f$ which describes the low energy hadrons. Here f stands for flavour, J is the total angular momentum, P *parity*, and C *charge conjugation*. Charge conjugation exchanges a particle for its anti-particle, $Ce^{\mp} = e^{\pm}$, whereas parity reverses the handedness of a field, $Pe^-_{L/R} = e^-_{R/L}$. Therefore, CP results in $CPe^{\mp}_{L/R} = e^{\pm}_{R/L}$. For CP conserved symmetries, all interactions would be the same for matter and anti-matter [2]. Baryons will not be discussed further in this thesis, with the exception of protons used in particle colliders in section 3.2.

For energies much larger than the binding energy of hadrons, the quarks can be assumed to be free [13]. This is due to *asymptotic freedom* which refers to theories where the coupling constant tends to zero as the energy scale increases [12].

Running of Couplings

When calculating diagrams of particle processes/interactions, an arbitrary number of loops, which are corrections to the tree-level process/interaction, can be considered. An example can be seen for the photon propagator seen in Figure 2.2, where the tree-level propagator is depicted on the left panel. The addition of a fermion loop can be seen in the middle panel, for loop momentum k. For an arbitrary number of insertions, represented by the blob on the right panel, a series of diagrams is created

[1] The Particle Data Group has full lists of known mesons and baryons [2].

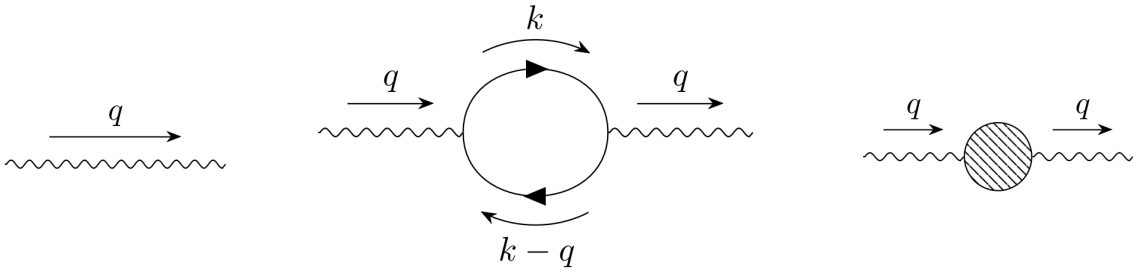

Figure 2.2: Photon propagator (left) with a fermion loop (middle), and arbitrary insertions (right).

with increasing orders in the coupling constant(s). From this, momentum/energy dependent (coupling) constants, that are said to be *running*, can be derived. An example of the phenomena of running coupling constants is the inclusion of heavy particles, that can appear in loops in leading order calculations. As the energy scale of the process increases, more and more heavy particles can be included in loops. As the momentum of the photon in Figure 2.2 increases, the number of quarks which can appear in the loop increases. But if the momentum considered is 10 GeV, the top quark with $m_t \approx 173$ GeV is not included. This effect can be seen in eq. (2.2.10). In the rest of this thesis, the coupling value for the relevant scale will be used.

The running of the strong coupling constant, α_s, will be presented without proof as this is beyond the scope of this thesis, see [17] for further information. At one-loop, the dependence of α_s on the energy scale Q is given by

$$\alpha_s(Q^2) = \frac{4\pi}{\beta_0 \ln\left(\frac{Q^2}{\Lambda^2}\right)}, \tag{2.2.10}$$

for scale parameter Λ and *beta*-function $\beta_0 = 11 - \frac{2}{3}n_f$, where n_f is the number of active quark flavours at the energy scale ($m_q^2 \ll Q^2$). As the energy scale increases, more and more quarks have to be taken into consideration as they start to appear in loops. Depending on the degree of accuracy needed in a calculation or measurement, the number of loops used when deriving the running of coupling constants should be increased.

Unless proper care is taken, the active number of quarks causes sudden changes in

α_s. This can be avoided by matching the value of α_s below and above the new quark masses,

$$\alpha_s^{n_f-1}(Q^2 = m_q^2) = \alpha_s^{n_f}(Q^2 = m_q^2)\,, \tag{2.2.11}$$

where m_q the quark mass. From this, equations for the scale parameter Λ are constructed. For leading order running of α_s, the dependence of Λ on the quark mass and n_f is given by [18]

$$\Lambda^{n_f} = \Lambda^{n_f-1}\left(\frac{\Lambda^{n_f-1}}{m_q}\right)^{\frac{2}{33-2n_f}}\,. \tag{2.2.12}$$

2.2.4 Spin, Helicity & Chirality

Up to now, the handedness, or chirality, of fermion fields and the spin of gauge bosons and fermions have been mentioned. But, the last concept connected to spin has not been introduced yet; *helicity*. The helicity operator projects a particle's spin onto its momentum, $\hat{h} = \hat{p}\cdot\vec{S}$ for momentum p and spin vector S and has eigenvalues $\pm\frac{1}{2}$ for fermions and $\{-1, 0, +1\}$ for vector bosons [12]. The foundations for the inclusion of spin and helicity in amplitude calculations will be presented here, for first fermions and afterwards gauge bosons.

Fermions

For massless fermions, it can be shown that the helicity eigenstates are the same as the chirality eigenstates, but for massive particles one can boost into a frame where the momentum is in the opposite direction, and thus helicity and chirality have to be distinguished [12].

For processes with initial or final state fermions, the Dirac field is written as a linear combination of plane waves,

$$\psi(x) = u(p)\cdot e^{-ip\cdot x} \qquad \text{and} \qquad \psi(x) = v(p)\cdot e^{+ip\cdot x}\,, \tag{2.2.13}$$

for column vectors $u(p)$ and $v(p)$ and momentum $p^2 = m^2$. Using the Dirac equation,

$\left(i\gamma^\mu\partial_\mu - m\right)\psi(x) = 0$, the momentum space equations are obtained,

$$0 = (\not{p} - m)u^s(p) = \bar{u}^s(p)(\not{p} - m)\,, \tag{2.2.14}$$

$$0 = (\not{p} + m)v^s(p) = \bar{v}^s(p)(\not{p} + m)\,. \tag{2.2.15}$$

Here, the notation $u^s(p)$ is introduced to include the helicities of the particle with $\bar{u}^r(p)u^s(p) = 2m\delta^{rs}$ and $\bar{v}^r(p)v^s(p) = -2m\delta^{rs}$. This requires the helicity of the particle to remain constant in the absence of interactions. u and v are orthogonal resulting in $\bar{u}^r(p)v^s(p) = 0 = \bar{v}^r(p)u^s(p)$. When performing amplitude calculations, the summation over all possible spin states is often required,

$$\sum_s u^s(p)\bar{u}^s(p) = \not{p} + m\,, \tag{2.2.16}$$

$$\sum_s v^s(p)\bar{v}^s(p) = \not{p} - m\,, \tag{2.2.17}$$

for particles with momentum p and mass m [12]. Spin-$\frac{1}{2}$ particles with four-momentum $p^\mu = (E, \boldsymbol{p})$ have a corresponding spin four-vector,

$$\text{Massive}: \; S^\mu = \frac{2\lambda}{m}\,(|\boldsymbol{p}|, E\,\hat{\boldsymbol{p}})\;, \tag{2.2.18}$$

$$\text{Massless}: \; S^\mu = 2\lambda\,(1, \hat{\boldsymbol{p}})\,, \tag{2.2.19}$$

where $\lambda = \pm\frac{1}{2}$ is the helicity of the particle [19]. Using the spin vectors, the following helicity projection expressions can be written,

$$u(p,\lambda)\bar{u}(p,\lambda) = \frac{1}{2}\,(1 + \gamma^5\not{S})(\not{p} + m) \tag{2.2.20}$$

$$\underset{m\to 0}{\Rightarrow} u(p,\lambda)\bar{u}(p,\lambda) = \frac{1}{2}\,(1 + 2\lambda\,\gamma^5)\not{p}\,, \tag{2.2.21}$$

$$v(p,\lambda)\bar{v}(p,\lambda) = \frac{1}{2}\,(1 + \gamma^5\not{S})(\not{p} - m) \tag{2.2.22}$$

$$\underset{m\to 0}{\Rightarrow} v(p,\lambda)\bar{v}(p,\lambda) = \frac{1}{2}\,(1 - 2\lambda\,\gamma^5)\not{p}\,, \tag{2.2.23}$$

which are used to implement the fermion's helicity into amplitudes [20].

Using these, the spinors of massless fermions can be re-written,

$$\bar{v}(p,\lambda) = \frac{1}{2}\bar{v}(p)(1 - 2\lambda\gamma^5) \qquad \text{and} \qquad u(p,\lambda) = \frac{1}{2}(1 + 2\lambda\gamma^5)u(p)\,. \tag{2.2.24}$$

Gauge Bosons

A spin-1 particle with four-momentum $k^\mu = (k_0, \boldsymbol{k})$ and helicity λ has a polarisation four-vector basis given by

$$\epsilon_1^\mu(k) = \frac{1}{|\boldsymbol{k}|k_T}\left(0, k_x k_z, k_y k_z, -k_T^2\right), \tag{2.2.25}$$

$$\epsilon_2^\mu(k) = \frac{1}{k_T}\left(0, -k_y, k_x, 0\right), \tag{2.2.26}$$

$$\epsilon_3^\mu(k) = \frac{k_0}{|\boldsymbol{k}|\sqrt{k^2}}\left(\frac{\boldsymbol{k}^2}{k_0}, k_x, k_y, k_z\right), \tag{2.2.27}$$

$$\epsilon_4^\mu(k) = \frac{1}{\sqrt{k^2}}\left(k_0, k_x, k_y, k_z\right), \tag{2.2.28}$$

where $k_T = \sqrt{k_x^2 + k_y^2}$ [21]. The longitudinal polarisation vector for a boson with $\lambda = 0$ is described by eq. (2.2.27), and the helicity eigenvectors with $\lambda = \pm 1$ are

$$\epsilon^\mu(k, \lambda) = \frac{1}{\sqrt{2}}\left[-\lambda\, \epsilon_1^\mu(k) - i\, \epsilon_2^\mu(k)\right]. \tag{2.2.29}$$

The last vector in the basis, $\epsilon_4^\mu(k)$, is equal to the normalised momentum of the particle. It is the unphysical time-like polarisation and completes the basis.

In order to sum over all possible polarisations for a massless gauge boson with momentum k, the polarisation sum rule is given by

$$\sum_s \epsilon_\mu^*(k)\epsilon_\nu(k) = -g_{\mu\nu}\,. \tag{2.2.30}$$

For massive gauge bosons, where the longitudinal polarisation modes have to be considered, the sum becomes

$$\sum_s \epsilon_\mu^*(k)\epsilon_\nu(k) = -g_{\mu\nu} + \frac{k^\mu k^\nu}{m_V^2}\,, \tag{2.2.31}$$

for mass m_V of the particle [12].

2.2.5 Particle Masses

One particle in Figure 2.1 remains to be explained; the only scalar particle in the SM, which is known as the *Higgs boson*. It is introduced as the solution to the following

problems.

The left-handed fermions are doublets under $SU(2)_L$ whereas the right-handed fermions are singlets under $SU(2)_L$, hence the fermionic mass term has the form,

$$\mathcal{L} \supset -m_f \bar{\psi}\psi = -m_f \left(\bar{\psi}_L \psi_R + \bar{\psi}_R \psi_L\right) , \tag{2.2.32}$$

using the notation introduced in eq. (2.2.6). This is not invariant under $SU(2)_L$ due to the product of a doublet and a singlet not being a gauge invariant scalar [22]. The same is true for the gauge bosons, where under $SU(2)_L$ gauge transformations the mass term is not invariant,

$$\mathcal{L} \supset \frac{1}{2} M_a^2 A_\mu A^\mu \to \frac{1}{2} M_a^2 \left(A_\mu - \frac{1}{e}\partial_\mu \alpha\right)\left(A^\mu - \frac{1}{e}\partial^\mu \alpha\right) \neq \frac{1}{2} M_a^2 A_\mu A^\mu \, . \tag{2.2.33}$$

This implies that fermions and gauge bosons are massless, though the masses of fermions, W, and Z bosons have been measured experimentally. Therefore, a piece of the theory is not covered by $SU(3)_C \times SU(2)_L \times U(1)_Y$ alone. The discrepancy is solved through the introduction of a $SU(2)_L$ doublet scalar field, which causes the $SU(2)_L \times U(1)_Y$ symmetry to spontaneously break; the Higgs boson [15, 23].

2.3 Spontaneous Symmetry Breaking & the Higgs Mechanism

The spontaneous breaking of $SU(2)_L \times U(1)_Y \to U(1)_{\mathrm{EW}}$ is performed by the *ABEGHHK'tH* mechanism (Anderson, Brout, Englert, Guralnik, Hagen, Higgs, Kibble, and 't Hooft), usually shortened to the *Higgs Mechanism* [24]. The following section will show how the Higgs boson introduces mass terms for the fermions and gauge bosons through *Spontaneous Symmetry Breaking* (SSB). A simplified example, the Linear Sigma Model, is used first to describe the concept of symmetry breaking.

2.3.1 The Linear Sigma Model

Consider N real scalar fields ϕ^i with a Lagrangian given by

$$\mathcal{L} = \frac{1}{2}(\partial_\mu \phi^i)^2 + \frac{1}{2}\mu^2(\phi^i)^2 - \frac{\lambda}{4}\left[(\phi^i)^2\right]^2 , \tag{2.3.1}$$

with a sum over i for each ϕ^i. The potential,

$$V(\phi^i) = -\frac{1}{2}\mu^2(\phi^i)^2 + \frac{\lambda}{4}\left[(\phi^i)^2\right]^2 , \tag{2.3.2}$$

has minimum for $(\phi_0^i)^2 = \mu^2/\lambda$ which fixes the length of the vector ϕ_0^i but not the direction. Choosing $\phi_0^i = (0, 0, ..., 0, v)$ for *vacuum expectation value* or *vev* $v = \mu/\sqrt{\lambda}$, the shifted fields are defined by the set

$$\left\{\pi^k(x), v + \sigma(x)\right\}, \tag{2.3.3}$$

for $k \in [1, N-1]$. The Lagrangian is re-written in terms of the shifted fields,

$$\begin{aligned}\mathcal{L} = \frac{1}{2}(\partial_\mu \pi^k)^2 + \frac{1}{2}(\partial_\mu \sigma)^2 - \frac{1}{2}(2\mu^2)\sigma^2 \\ - \sqrt{\lambda}\mu\sigma^3 - \sqrt{\lambda}\mu(\pi^k)^2\sigma - \frac{\lambda}{4}\sigma^4 - \frac{\lambda}{2}(\pi^k)^2\sigma^2 - \frac{\lambda}{4}\left[(\pi^k)^2\right]^2 .\end{aligned} \tag{2.3.4}$$

Field σ requires mass ($m_\sigma = \sqrt{2}\mu$) whereas π^k are $N-1$ massless fields. The original Lagrangian is invariant under symmetry $\phi^i \to R^{ij}\phi^j$ for $N \times N$ orthogonal matrix R. This symmetry is hidden in the new Lagrangian, but can be restored by using linear combinations of the fields σ and π^k. The final Lagrangian is invariant to the rotation of the fields π^k amongst themselves, and hence the original $\mathcal{O}(N)$ symmetry is spontaneously broken to a $\mathcal{O}(N-1)$ subgroup.

2.3.2 Higgs Mechanism

Having shown how spontaneous symmetry breaking is introduced by a scalar field acquiring a non-zero vacuum expectation value, it will now be shown how this leads to the introduction of mass terms for both fermions and vector bosons in the SM.

Gauge Boson Masses

Consider a complex scalar boson ϕ and a massless gauge boson A^μ with Lagrangian,

$$\mathcal{L} \supset (D_\mu \phi)^* (D^\mu \phi) + \mu^2 \phi^* \phi - \lambda (\phi^* \phi)^2 - \frac{1}{4} F^{\mu\nu} F_{\mu\nu} \,, \tag{2.3.5}$$

for $F^{\mu\nu} = \partial^\mu A^\nu - \partial^\nu A^\mu$, $\lambda > 0$, and $\mu^2 > 0$. Requiring local gauge transformations,

$$\phi \to \phi' = e^{igX(x)\phi} \qquad \text{and} \qquad A^\mu \to A'^\mu = A^\mu - \partial^\mu X(x) \,, \tag{2.3.6}$$

for some function $X(x)$, the covariant derivative is found to be $D^\mu = \partial^\mu + igA^\mu$. The scalar field potential,

$$V(\phi) = -\mu^2 \phi^* \phi + \lambda (\phi^* \phi)^2 \,, \tag{2.3.7}$$

has minimum at $\phi = v_H/\sqrt{2} = \sqrt{\mu^2/2\lambda}$ for vev v_H. Expanding around the minimum, the complex scalar field is written in terms of real field $h(x)$,

$$\phi = \frac{1}{\sqrt{2}} \begin{pmatrix} 0 \\ v_H + h(x) \end{pmatrix} \,, \tag{2.3.8}$$

which results in a Lagrangian given by

$$\begin{aligned} \mathcal{L} = \frac{1}{2} \left[\left(\partial_\mu - igA_\mu \right) (v_H + h) \left(\partial^\mu + igA^\mu \right) (v_H + h) \right] \\ + \frac{1}{2} \mu^2 (v_H + h)^2 - \frac{1}{4} \lambda (v_H + h)^4 - \frac{1}{4} F^{\mu\nu} F_{\mu\nu} \,. \end{aligned} \tag{2.3.9}$$

From this Lagrangian, the mass terms for the gauge boson $\left(\mathcal{L} \supset g^2 v_H^2 / 2 A_\mu^A \mu \right)$ and the scalar boson $\left(\mathcal{L} \supset -\lambda v_H^2 h^2 \right)$ are found, together with the interaction terms proportional to higher-order combinations of the fields. The theory with a complex scalar boson and a massless gauge boson has therefore been rewritten in terms of a real scalar boson and a massive gauge boson due to the non-zero scalar potential minimum.

The Higgs field is a $SU(2)_L$ doublet of complex scalars, consisting of four real fields and the SM contains four massless gauge bosons, W^a and B, with two polarisation states each ($\lambda = \pm 1$). The vacuum expectation value causes symmetry breaking

resulting in one real Higgs field, one massless gauge boson, and three massive gauge bosons with three polarisation states ($\lambda \in \{-1, 0, +1\}$). Similarly to the linear sigma model presented above, the spontaneous symmetry breaking results in $SU(2)_L \times U(1)_Y \to U(1)_{\mathrm{EW}}$, called *Electroweak Symmetry Breaking* (EWSB) [15].

Fermion Masses

The Higgs boson is a doublet under $SU(2)_L$ with $Y = \frac{1}{2}$, which allows for the construction of the gauge invariant Lagrangian term given by

$$\mathcal{L} \supset -\lambda_l \left(\bar{L}_L \cdot \phi\right)\ l_R + \text{h.c.}\,, \tag{2.3.10}$$

for Higgs field ϕ, lepton doublet L_L, singlet l_R, and constant λ_l. After EWSB this becomes

$$\mathcal{L} \supset -\frac{1}{\sqrt{2}}\lambda_l v_H \bar{L}_L l_R + \text{h.c.}\,, \tag{2.3.11}$$

where the Higgs field has been replaced by its vev. The Lagrangian term corresponds to a lepton with mass given by

$$m_l = \frac{1}{\sqrt{2}}\lambda_l v_H\,. \tag{2.3.12}$$

As right-handed neutrinos do not interact with the Higgs doublet, it is not possible to construct the same term for neutrinos only, and hence in the SM neutrinos are massless. It will later be shown in section 2.5 how this is one of the unsolved puzzles of particle physics.

The mass terms for quarks are introduced,

$$\mathcal{L} \supset -\lambda_d \left(\bar{Q}_L \cdot \phi\right)\ d_R - \lambda_u \epsilon^{ab} \bar{Q}_{La} \phi_b^\dagger u_R + \text{h.c}\,, \tag{2.3.13}$$

for matrices $\lambda_{u,d}$, quark doublet Q_L, singlets d_R and u_R, and two-dimensional Levi-Civita symbol ϵ^{ab}. Here a second construction, which is invariant under $SU(2)_L$, is used,

$$\epsilon^{ab} \bar{Q}_{La} \phi_b^\dagger = i \bar{Q}_L \sigma_2 \phi^* = \bar{Q}_L \tilde{\phi}\,, \tag{2.3.14}$$

for the second *Pauli matrix* σ_2, from $SU(2)_L$ generators $\tau^a = \frac{\sigma^a}{2}$, and $\tilde{\phi} = i\sigma_2\phi^*$. After EWSB, the Higgs' vev is introduced, leading to

$$\mathcal{L} \supset -\frac{v_H}{\sqrt{2}}\left(\lambda_d \bar{d}_L d_R + \lambda_u \bar{u}_L u_R\right) + \text{h.c}\,, \tag{2.3.15}$$

for quark masses given by

$$m_d = \frac{1}{\sqrt{2}}\lambda_d v_H \qquad \text{and} \qquad m_u = \frac{1}{\sqrt{2}}\lambda_u v_H\,. \tag{2.3.16}$$

The treatment of quarks in the SM will not be described further in this thesis [12]. Finally, the Yukawa Lagrangian is constructed,

$$\mathcal{L}_{\text{Yukawa}} = -\lambda_l \bar{L}_L\,\phi\, l_r - \lambda_d \bar{Q}_L\,\phi\, d_R - \lambda_u \bar{Q}_L\,\tilde{\phi}\, u_R + \text{h.c.}\,. \tag{2.3.17}$$

2.4 Glashow-Weinberg-Salam Theory

As alluded to earlier, the four gauge boson fields initially seen in the Standard Model are not the same as the ones detected by experiments. The Glashow-Weinberg-Salam Theory describes how the photon, W, and Z boson fields are composed of the initial four gauge fields. First, the derivation of the mass eigenstates of the gauge boson fields is presented, followed by the couplings between these and the fermion sector.

2.4.1 Gauge Boson Mass Eigenstates

The covariant derivative from eq. (2.2.3) and the scalar definition from eq. (2.3.8) are inserted into the kinetic term of the Higgs boson, $(D_\mu\phi)^\dagger D^\mu\phi$,

$$\mathcal{L} \supset \frac{1}{2}\begin{pmatrix}0 & v_H\end{pmatrix} \cdot \left(gW^a_\mu\tau^a + \frac{1}{2}g'B_\mu\right)\left(gW^{b\mu}\tau^b + \frac{1}{2}g'B^\mu\right) \cdot \begin{pmatrix}0\\ v_H\end{pmatrix}, \tag{2.4.1}$$

where the Higgs field h is neglected. Using generator definitions $\tau^a = \frac{\sigma^a}{2}$ for Pauli matrices σ^a, the Lagrangian is re-written to be

$$\mathcal{L} \supset \frac{1}{2}\frac{v_H^2}{4}\left[g^2(W^1_\mu)^2 + g^2(W^2_\mu)^2 + \left(-gW^3_\mu + g'B_\mu\right)^2\right]. \tag{2.4.2}$$

The four mass eigenstates are the one massless A_μ and the three massive $W_\mu^\pm$ and Z_μ^0 vector bosons given by

$$W_\mu^\pm = \frac{1}{\sqrt{2}}\left(W_\mu^1 \mp iW_\mu^2\right) , \tag{2.4.3}$$

$$Z_\mu^0 = \frac{1}{\sqrt{g^2+(g')^2}}\left(gW_\mu^3 - g'B_\mu\right) , \tag{2.4.4}$$

$$A_\mu = \frac{1}{\sqrt{g^2+(g')^2}}\left(g'W_\mu^3 + gB_\mu\right) , \tag{2.4.5}$$

for masses $m_W = \frac{1}{2}g\,v_H$ and $m_Z = \frac{1}{2}v_H\sqrt{g^2+(g')^2}$.

The W bosons are found straightforwardly from the Lagrangian, whereas the Z boson and the photon are found through the mixing of W_μ^3 and B_μ. For angle θ_W, called the *weak mixing* or *Weinberg* angle, the mixing matrix is given by

$$\begin{pmatrix} Z_\mu^0 \\ A_\mu \end{pmatrix} = \begin{pmatrix} \cos\theta_W & -\sin\theta_W \\ \sin\theta_W & \cos\theta_W \end{pmatrix} \begin{pmatrix} W_\mu^3 \\ B_\mu \end{pmatrix} , \tag{2.4.6}$$

with

$$\cos\theta_W = \frac{g}{\sqrt{g^2+(g')^2}} . \tag{2.4.7}$$

The W boson mass can be written as $m_W = m_Z\cos\theta_W$ and used to define the *Fermi constant*, $G_F = \frac{\sqrt{2}}{8}\left(\frac{g}{m_W}\right)^2$. Finally, defining the *electron charge*,

$$e = \frac{gg'}{\sqrt{g^2+(g')^2}} , \tag{2.4.8}$$

the coupling constant g is simplified, $g = \frac{e}{\sin\theta_W}$ [12].

2.4.2 Gauge Bosons Couplings

Having derived the gauge boson mass eigenstates, their couplings to fermions can be determined from the fermion kinetic terms,

$$\mathcal{L} \supset i\left[\bar{L}_L \not{D} L_L + \bar{Q}_L \not{D} Q_L + \bar{e}_R \not{D} e_R + \bar{u}_R \not{D} u_R + \bar{d}_R \not{D} d_R\right] , \tag{2.4.9}$$

where the covariant derivatives contain the physical gauge fields of $W^{\pm}_{\mu}$, Z^0_{μ}, and A_{μ}. This allows for the extraction of the interactions between gauge fields and fermions,

$$\mathcal{L} \supset g\left(W^+_{\mu} J^{\mu+}_W + W^-_{\mu} J^{\mu-}_W + Z^0_{\mu} J^{\mu}_Z\right) + eA_{\mu} J^{\mu}_{\mathrm{EM}}\,. \tag{2.4.10}$$

Here, the couplings are constructed using the *currents* given by

$$J^{\mu+}_W = \frac{1}{\sqrt{2}}\left(\bar{\nu}_L \gamma^{\mu} e_L + \bar{u}_L \gamma^{\mu} d_L\right)\,, \tag{2.4.11}$$

$$J^{\mu-}_W = \frac{1}{\sqrt{2}}\left(\bar{e}_L \gamma^{\mu} v_L + \bar{d}_L \gamma^{\mu} u_L\right)\,, \tag{2.4.12}$$

$$\begin{aligned} J^{\mu}_Z = \frac{1}{\cos\theta_w}\Bigg[&\frac{1}{2}\bar{\nu}_L \gamma^{\mu} \nu_L + \left(-\frac{1}{2} + \sin^2\theta_w\right)\bar{e}_L \gamma^{\mu} e_L + \sin^2\theta_w \bar{e}_R \gamma^{\mu} e_R \\ &+ \left(\frac{1}{2} - \frac{2}{3}\sin^2\theta_w\right)\bar{u}_L \gamma^{\mu} u_L - \frac{2}{3}\sin^2\theta_w \bar{u}_R \gamma^{\mu} u_R \\ &+ \left(-\frac{1}{2} + \frac{1}{3}\sin^2\theta_w\right)\bar{d}_L \gamma^{\mu} d_L + \frac{1}{3}\sin^2\theta_w \bar{d}_R \gamma^{\mu} d_R\Bigg]\,, \end{aligned} \tag{2.4.13}$$

$$J^{\mu}_{EM} = -\bar{e}\gamma^{\mu} e + \frac{2}{3}\bar{u}\gamma^{\mu} u - \frac{1}{3}\bar{d}\gamma^{\mu} d\,. \tag{2.4.14}$$

It can be recognised, that the constants in the electromagnetic current J^{μ}_{EM} are the associated fields' charges under $U(1)_Y$, which can also be seen in J^{μ}_Z though it is more hidden there [12].

2.5 Neutrinos

Having provided a general introduction to neutrinos, a more in-depth description will now follow. As described previously in section 2.3.2, right-handed neutrinos do not interact with the remaining SM particle content, whilst the SM left-handed neutrino interactions consist of two separate contributions; leptonically universal gauge interactions,

$$\mathcal{L} \supset -\left(\frac{g}{\sqrt{2}} W^+_{\mu} \sum_{a=1}^{3} \bar{\nu}_{aL} \gamma^{\mu} l_{aL} + \mathrm{h.c.}\right) - \frac{g}{2\cos\theta_W} Z_{\mu} \sum_{a=1}^{3} \bar{\nu}_{aL} \gamma^{\mu} v_{aL}\,, \tag{2.5.1}$$

and gauge-invariant Yukawa interactions,

$$\mathcal{L} \supset - \sum_{a_1,a_2=1}^{3} f^l_{a_1 a_2} \bar{L}_{a_1\, L}\, \phi\, l_{a_2\, R} + \text{h.c.}\,, \tag{2.5.2}$$

which depend on the lepton doublet L_{aL}, singlet l_{aR}, Higgs field ϕ, and matrix f^l [25].

In W-boson decays the neutrinos are produced in association with a charged lepton, see eq. (2.5.1), and therefore they are produced in flavour eigenstates [13]. It has been proven experimentally that neutrinos go through *flavour oscillations*, where the flavour (weak) eigenstates (ν_e, ν_μ, or ν_τ) evolve over time; the originally produced neutrino flavour may not be the same as that detected some time later. The cause of these oscillations is the difference between the neutrino flavour eigenstates and mass eigenstates, which can be written $\nu_{1,2,3}$ for masses $m_{1,2,3}$. The probability of oscillation between the different flavour eigenstate is proportional to the difference in mass between the mass eigenstates, and hence the existence of oscillations infer that the masses differ and that not all three neutrino states can be massless [13]. The lack of neutrino masses in the SM is a major disagreement between experiment and theory. Many models have been introduced with the aim to give the neutrinos masses, one of which will be described later in section 4.2.4.

The neutrino flavour states can be written as a linear composition of the mass eigenstates,

$$|\nu_\alpha\rangle = \sum_j U^{\text{PMNS}}_{\alpha j} |\nu_j\rangle \qquad \Rightarrow \qquad \begin{pmatrix} \nu_e \\ \nu_\mu \\ \nu_\tau \end{pmatrix} = U^{\text{PMNS}} \begin{pmatrix} \nu_1 \\ \nu_2 \\ \nu_3 \end{pmatrix}, \tag{2.5.3}$$

where U^{PMNS} is the *Pontecorvo-Maki-Nakagawa-Sakata* matrix given by [26]

$$|U^{\mathrm{PMNS}}| = \begin{pmatrix} |U_{e1}| & |U_{e2}| & |U_{e3}| \\ |U_{\mu 1}| & |U_{\mu 2}| & |U_{\mu 3}| \\ |U_{\tau 1}| & |U_{\tau 2}| & |U_{\tau 3}| \end{pmatrix}, \tag{2.5.4}$$
$$= \begin{pmatrix} [0.801, 0.845] & [0.513, 0.579] & [0.143, 0.156] \\ [0.233, 0.507] & [0.461, 0.694] & [0.631, 0.778] \\ [0.261, 0.526] & [0.471, 0.701] & [0.611, 0.761] \end{pmatrix},$$

for parameters $U_{\alpha i}$ with $i \in \{1, 2, 3\}$ and $\alpha \in \{e, \mu, \tau\}$ [27]. Each entry in the PMNS matrix has a complex value, the real parts have been shown here, where the phases and further detail can be found in [2]. It can be seen that there is no considerable pattern to the values of the PMNS matrix; none of the elements are significantly bigger or smaller than the rest.

At collider scale energies and distances, neutrino oscillations do not have to be taken into account as the characteristic oscillation length is much larger than the radius of the detectors [13].

2.6 Cross-sections & Scattering Amplitudes

The Standard Model has now been introduced, with its particles and their interactions, and now the methodology to calculate expectations for experiments can be described. To begin with, the concept of amplitudes and cross-sections will be introduced following the most commonly used method of calculating these. Finally, a description of particle decay is included.

When considering particle colliders, there is an initial state $|i\rangle$ with the two incoming beam particles and a final state $|f\rangle$ with all outgoing particles. It is assumed that the initial state consists of free particles existing at time $t \to -\infty$, whereas the free final state particles are at $t \to +\infty$ with interactions happening in-between the two

times. The initial and final states are used to measure the transition probability,

$$P = \frac{|\langle f|i\rangle|^2}{\langle f|f\rangle \langle i|i\rangle}, \tag{2.6.1}$$

which describes the probability of the initial state $|i\rangle$ ending up as the final state $|f\rangle$. The *S-matrix* is defined to be

$$S_{fi} = \langle f|i\rangle = \delta_{if} + i(2\pi)^4 \delta^{(4)}(P_f - P_i)\mathcal{M}_{fi}, \tag{2.6.2}$$

for the sum of initial and final state four-momenta $P_{i,f}$ and the *Lorentz invariant matrix element* $\mathcal{M}$. Here momentum conservation is enforced using the Dirac delta function δ. It can be seen that the S-matrix describes two scenarios; the initial and final state are the same (δ_{if}), or something happens such that the state changes, which is described by $\mathcal{M}$ [28].

In an experiment, the probability of a process is dependent on more than the matrix element; it is described by the *cross-section*,

$$\sigma = \frac{N}{T\Phi} \qquad \Rightarrow \qquad d\sigma = \frac{dN}{T\Phi}, \tag{2.6.3}$$

for the running time of the experiment T, incoming *flux* Φ, number of particles scattered N, and dN the probability of N particles to scatter. The flux describes the number of incoming particles per unit time per unit area. The cross-section can be imagined as the probability of a projectile hitting a surface, and hence it has units *barns* ($1\,\text{barn}\,[b] = 10^{-24} cm^2$ [29]).

The derivation of the *differential cross-section* for $2 \to 2$ scattering is now briefly described, for further detail see [16]. Starting from an arbitrary $2 \to n$ scattering, $p_1 + p_2 \to p_j$ for $j \in [1, n]$, the cross-section,

$$d\sigma = \frac{1}{(2E_1)(2E_2)|\vec{v}_1 - \vec{v}_2|} |\mathcal{M}|^2 \, d\Pi_{\text{LIPS}}, \tag{2.6.4}$$

is defined for initial energies $E_{1,2}$ and velocities $\vec{v}_{1,2}$, and the *Lorentz-invariant phase space* (LIPS),

$$d\Pi_{\text{LIPS}} = (2\pi)^3 \delta^{(4)}\left(\sum p\right) \prod_j \frac{d^3 p_j}{(2\pi)^3} \frac{1}{2E_j}\,. \tag{2.6.5}$$

Here $\delta^{(4)}\left(\sum p\right) = \delta^{(4)}\left(\sum p_i^\mu - \sum p_f^\mu\right)$ is the momentum conservation for initial and final state momenta. For $2 \to 2$ processes, the phase space is given by

$$d\Pi_{\text{LIPS}} = \frac{1}{16\pi^2}\, d\Omega\, \frac{p_f}{E_{\text{CMS}}} \Theta(E_{\text{CMS}} - m_3 - m_4)\,, \tag{2.6.6}$$

for the solid angle Ω, masses of the two final states $m_{3,4}$, *centre-of-mass* (CMS) energy for the process,

$$E_{\text{CMS}} = \sqrt{(p_1^\mu + p_2^\mu)\left(p_{1\mu} + p_{2\mu}\right)}\,, \tag{2.6.7}$$

see section 3.2.2 for further detail, and *Heaviside function*,

$$\Theta(x) = \begin{cases} 1 & x \geq 0\,, \\ 0 & \text{otherwise}\,. \end{cases} \tag{2.6.8}$$

The differential cross-section in the centre-of-mass frame, where the incoming particles have the same momentum, is given by [16]

$$\left(\frac{d\sigma}{d\Omega}\right)_{\text{CMS}} = \frac{1}{64\pi^2 E_{\text{CMS}}^2} \frac{p_f}{p_i} |\mathcal{M}|^2 \Theta(E_{\text{CMS}} - m_3 - m_4)\,. \tag{2.6.9}$$

2.6.1 Amplitudes for Polarised Initial & Final States

Due to its use in chapter 6, the effects of the initial and final state polarisation in the process $e^+e^- \to \gamma + X$ are commented upon. In particular, for incoming electron and positrons, the amplitudes for right-and left-handed fermions are defined as

$$|\mathcal{M}_{RR}|^2 = |\mathcal{M}|^2\left(\lambda_{e^-} = +\frac{1}{2}, \lambda_{e^+} = +\frac{1}{2}\right), \tag{2.6.10}$$

$$|\mathcal{M}_{LR}|^2 = |\mathcal{M}|^2\left(\lambda_{e^-} = -\frac{1}{2}, \lambda_{e^+} = +\frac{1}{2}\right), \tag{2.6.11}$$

similarly for $|\mathcal{M}_{LL}|^2$ and $|\mathcal{M}_{RL}|^2$. For longitudinally polarised fermion beams, the amplitude can be separated into parts proportional to the four combinations of

fermion helicities,

$$|\mathcal{M}|^2 = \frac{1}{4}\Big\{ \left(1+P_{e^-}\right)\left(1+P_{e^+}\right)|\mathcal{M}_{RR}|^2 + \left(1-P_{e^-}\right)\left(1-P_{e^+}\right)|\mathcal{M}_{LL}|^2 \\ + \left(1+P_{e^-}\right)\left(1-P_{e^+}\right)|\mathcal{M}_{RL}|^2 + \left(1-P_{e^-}\right)\left(1+P_{e^+}\right)|\mathcal{M}_{LR}|^2 \Big\}, \tag{2.6.12}$$

where $P_{e^\pm}$ is the degree of electron and positron polarisation given by

$$P_{e^\pm} = \frac{n_{e^\pm_R} - n_{e^\pm_L}}{n_{e^\pm_R} + n_{e^\pm_L}}, \tag{2.6.13}$$

Here $n_{e^\pm_{R,L}}$ denote the number of left- and right-handed electrons and positrons in each beam. An unpolarised beam has $P_{e^\pm} = 0$, and $P_{e^\pm} = \pm 1$ are 100% left- and right-handed polarised beams respectively.

Using the degree of photon polarisation,

$$\alpha_\gamma = \frac{\gamma_R - \gamma_L}{\gamma_R + \gamma_L}, \tag{2.6.14}$$

the amplitude can again be separated into parts,

$$|\mathcal{M}|^2 = \frac{1}{2}\left\{(1+\alpha_\gamma)\gamma_R + (1-\alpha_\gamma)\gamma_L\right\}, \tag{2.6.15}$$

where $\gamma_L = |\mathcal{M}|^2(\lambda_\gamma = -1)$ and $\gamma_R = |\mathcal{M}|^2(\lambda_\gamma = +1)$.

2.6.2 Feynman Rules

The most common method to calculate matrix elements is through the visualisation and formation of diagrams for processes, called *Feynman Diagrams*. These are space-time representations of particle interactions, and are used for the construction of matrix element calculations which consists of *Feynman rules*. Given a Lagrangian, like the ones presented above, expressions for the Feynman rules can be derived. The Feynman rules in Feynman gauge for incoming and outgoing external particles (fermions and vector bosons) and their propagators can be seen in Table 2.2, for further detail see [12]. Each interaction vertex has a corresponding Feynman Rule found from the interactions in the Lagrangian, for example the coupling between a

photon and an electron-pair is found from eq. (2.4.14) to be $-ie\gamma^{\mu}$.

The derivation of Feynman rules is a laborious process, and hence softwares like FeynRules [30] have been developed in order to automatise the derivations. For the remainder of this thesis, FeynRules will be utilised for the extraction of Feynman rules from the Lagrangians of New Physics.

Particle	Fermion	Anti-Fermion	Polarisation Vector	Scalar
Incoming	$u(p)$	$\bar{v}(p)$	$\epsilon_{\mu}(p)$	1
Outgoing	$\bar{u}(p)$	$v(p)$	$\epsilon^{*}_{\mu}(p)$	1
Propagators	$\frac{i(\not{p}+m)}{p^2-m^2}$		$\frac{-i\left(g_{\mu\nu}-\frac{p_{\mu}p_{\nu}}{m_V^2}\right)}{p^2-m_V^2}$	$\frac{i}{p^2-m^2}$

Table 2.2: Incoming and outgoing particle notation and particle propagators for fermions, vector bosons, and scalars.

2.6.3 Decays

The decay width of a particle is the probability that the particle will decay to n decay products. It is given by

$$d\Gamma = \frac{1}{2\gamma_1 m_1}|\mathcal{M}|^2 d\Pi_{\text{LIPS}}\,, \tag{2.6.16}$$

for m_1 the mass of the initial particle, γ_1 the gamma factor $\gamma = (1-\beta^2)^{-1/2}$ with $\beta = \frac{v}{c}$, $d\Pi_{\text{LIPS}}$ the phase space, and $|\mathcal{M}|^2$ the amplitude for the decay [16]. Summing over all possible decays for the particle, the total decay width Γ is derived.

Due to time dilation, the proper time for a particle produced in a collider is $t = \gamma\tau$ for gamma factor γ, and the lifetime of the particle $\tau = \frac{\hbar}{\Gamma}$, which is given by its total decay width Γ. The decay length of the particle is given by its velocity and the proper time,

$$\lambda = vt = \beta\gamma c\tau\,, \tag{2.6.17}$$

for the *boost* of the particle $\beta\gamma$. These can re-write in terms of the energy, momentum, and mass of the decaying particle; $\gamma = \frac{E}{m}$ and $\beta = \frac{p}{E}$ [28]. Hence, the decay length of a particle can be expressed for the momentum p and mass m,

$$\lambda = \frac{p}{m} c\tau \,. \tag{2.6.18}$$

The decay length is not certain and therefore the probability for particle to decay at a distance l is given by

$$P(l) = \frac{e^{-l/\lambda}}{\lambda} \,, \tag{2.6.19}$$

for the *characteristic* decay length λ as defined above [31].

Stability describes whether a particle will decay; some particles are unconditionally *stable*, and hence they do not decay regardless of how much time passes, whereas others are *unstable*. It is possible for unstable particles to appear stable if their lifetime is much longer than the timeframe considered. For example, the muon has a lifetime of $\tau \approx 2.2 \times 10^{-6}$ s with $c\tau \simeq 660$ m, therefore the muon is an unstable particle but on collider distances $\mathcal{O}(10)$ m it is stable.

2.7 Conclusion

The current best theory for the fundamental particles in the universe and their interactions, known as the Standard Model, was described. How the Higgs mechanism introduces masses for the fermion and gauge boson sectors, leading to Glashow-Weinberg-Salam theory for the physical mass eigenstates of gauge bosons and the interactions between these and fermions. But this is not the full picture, and there are several issues that the model does not address. Neutrinos have masses, and the existence of dark matter is absent. Many theories and models have been proposed to resolve the problems, introducing new particles and interactions. Theoretically, many of these are well-motivated and equally-likely, and hence there is a need to determine which model is correct. This is carried out by experiments, testing the theories by comparing their predictions to the results found. Many hundreds have

been carried out throughout the years, either with the intention to precisely measure a value predicted by the Standard Model, or specifically looking for New Physics.

Chapter 3

Particle Collider Physics

3.1 Introduction

One of the biggest and most well-known categories of particle physics experiments are particle colliders. They have played a major role throughout the years, leading to the discovery of several particles in the Standard Model. The concept has been mentioned already, but a more in-depth description will be provided here.

This chapter starts with an introduction to particle colliders in section 3.2, briefly describing the different types of colliders together with the detectors present at each, the parameters and observables used to analyse the output of detectors, and the methodology behind comparing experimental results to theoretical predictions. Sections 3.3 and 3.4 contain reviews of the Belle II and ATLAS detectors at SuperKEKB and the *Large Hadron Collider* (LHC) respectively. The various parts of the detectors, together with the *Chiral Belle Programme* are covered, forming the foundation for subsequent chapters. Lastly, section 3.5 outlines the general approach for New Physics searches in colliders.

3.2 Particle Colliders

Particle accelerators or colliders are machines which accelerate particles to near-speed-of-light velocity and then collide them. Colliders usually use electric and magnetic fields in order to accelerate the particles, the beams are therefore restricted to consist of charged particles such as leptons (electrons, positrons, muons, etc), hadrons (protons, anti-protons), ions, and many others.

A variety of collider types exist; fixed-target (one beam and one stationary target of particles or nuclei), linear, and circular colliders which differ by the acceleration method of the incoming beams. Colliders with two incoming beams have larger energies available in the collisions, as it is not reduced by the increase of kinetic energy in the fixed target. The advantage of linear colliders is that the incoming beams do not lose energy due to *synchrotron radiation*, which arises from the constant acceleration of the charged particles when travelling in a circle. But they require much greater distances in order to accelerate particles, whereas a circular collider achieves this through having the particles complete several rotations. Circular colliders can reach higher luminosities than linear colliders, see section 3.2.2 for further detail, as they reuse the beam particles which did not take part in the collision [28].

Figure 3.1 displays the layout of a circular collider, specifically the LHC at CERN

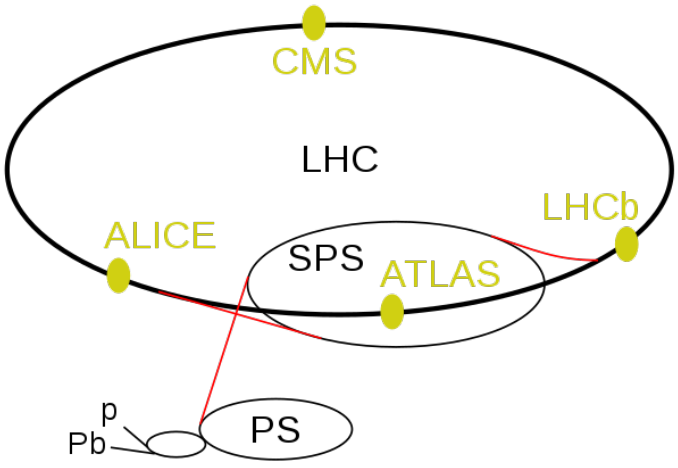

Figure 3.1: The LHC circular collider with its main detectors, see detail in text (from [32]).

(*Conseil européen pour la Recherche nucléaire*). It can be seen how the protons are produced away from the collider, then directed into the main ring for acceleration (red lines), and finally brought to collide at four points along the ring where the main four detectors are located (in yellow). See section 3.4 for further detail.

The centre-of-mass energy describes the energy available in each event at the collider. For initial particles with energies $E_{1,2}$, masses $m_{1,2}$, and $p_1^\mu = \left(E_1, 0, 0, -\sqrt{E_1^2 - m_1^2}\right)$ and $p_2^\mu = \left(E_2, 0, 0, \sqrt{E_2^2 - m_2^2}\right)$, the centre-of-mass energy is defined by

$$\begin{aligned} E_{\text{CMS}} = \sqrt{s} &= \sqrt{\left(p_1^\mu + p_2^\mu\right)\left(p_{1\mu} + p_{2\mu}\right)}\,, \\ &= \left(2E_1E_2 + \left[m_1^2 + m_2^2\right] + 2\cos\theta_c\sqrt{E_1^2 - m_1^2}\sqrt{E_2^2 - m_2^2}\right)^{\frac{1}{2}}\,, \end{aligned} \tag{3.2.1}$$

for beam crossing angle θ_c and s one of three *Mandelstam variables* (see eq. (3.2.6) for further detail). The crossing angle describes the angle at which the particles collide at the *interaction point* (IP), often approximated to be zero for which $\sqrt{s} \approx 2\sqrt{E_1E_2}$, when the masses of the incoming particles are much smaller than their energies .

Figure 3.2 displays nearly a hundred years of particle colliders, both past and future, with the evolution of the centre-of-mass energy, labelled E_{cme} in the Figure. It is seen that hadron colliders can reach higher energies than lepton, but because hadrons are composite particles only a fraction of the energy is available in each collision [33]. At high energies, the individual partons in the incoming protons collide. If the proton is moving at near-speed-of-light, the momenta of the individual partons (p_i) can be described as a fraction of the overall proton momentum P,

$$p_i = x_i P\,, \tag{3.2.2}$$

for *momentum fraction* $0 \leq x_i \leq 1$. Therefore, *Parton Distribution Functions* (PDFs) $f_\alpha(x_i)$, the probability of finding a parton of type α with momentum fraction x_i inside the proton, are defined. As these functions describe partons confined and bound into hadrons this cannot be derived theoretically with current methods, and PDFs are therefore measured experimentally. Extracting and fitting PDFs from data

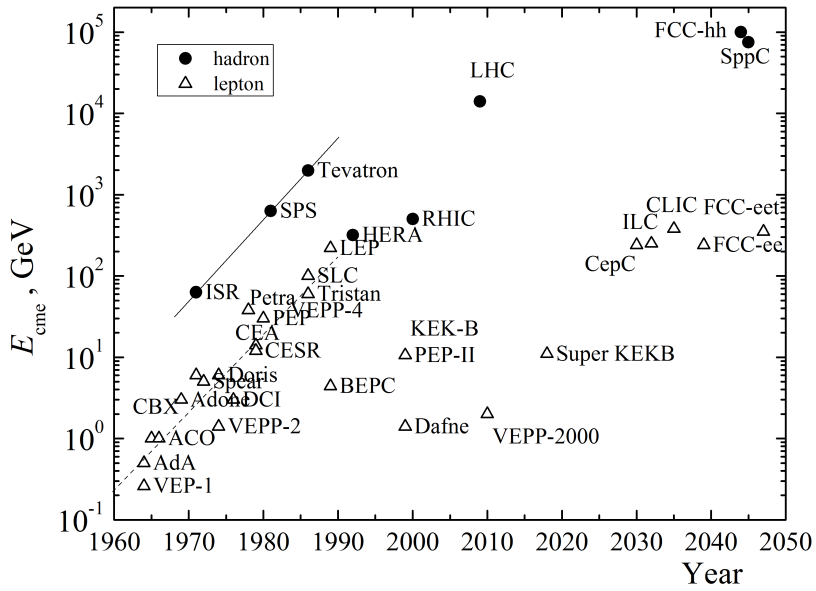

Figure 3.2: Centre-of-mass energies, E_{cme}, for past and future colliders (from [34]).

introduces uncertainties and errors, and hence there are different sets of PDFs one can choose between when performing simulations and analyses.

Many particle colliders have beams consisting of *bunches* of particles. For hadron colliders, when these bunches of protons collide, one of the partons participates in the *hard interaction* (the main collision), leaving the remaining partons, the *beam remnants*. These can interact with each other creating the *underlying event*. Furthermore, as the bunches consist of several protons, there is the probability that more than one pair of protons collide in the same bunch, causing *pile-up* where several events occur at indistinguishable times [28]. Colour confinement demands that the beam remnants must combine with each other, or the hard interaction final state, forming hadrons which add to the pile-up.

The result of these effects, alongside the lack of gluons and colour structure, means that lepton colliders have "cleaner" environments than hadron colliders; they have much less background noise consisting of processes that are not of interest [33].

After the collision, the resulting showers of particles are detected by the detectors which are built around the interaction points of the colliders.

3.2.1 Particle Detectors

For circular colliders, their main associated detectors are typically cylindrical and located such that the *beam pipe* goes through the centre. They are constructed using several layers, each specialising in detecting certain groups of particles, and so each detector has a different layout. A more thorough description of the two detectors considered in this thesis are described in section 3.3.1 and section 3.4. For cylindrical detectors, the *forwards* and *backwards* directions are defined as the regions of the detector close to the beam axis in either direction [28].

The output of a detector can be thought of theoretically as consisting of a list of particles with their properties and four-momentum, together with the potentially missing energy of each event. The four-momenta are defined in a coordinate system where the z-axis is parallel to the incoming beam with a transverse (x, y) plane. The missing energy is found by subtracting the sum of the energies of the outgoing particles observed, from the energy of the incoming beams. There are several reasons for having non-zero missing energy which will be described in future sections.

When analysing the results from the detectors, the differential cross-section is a useful property. It describes the probability of obtaining a certain final-state distribution for a given *observable*. The observables are either measured in the detector or constructed using other observables which can be measured. The differential cross-section for any observable $\mathcal{O}$,

$$f(\mathcal{O}) = \frac{d\,\sigma}{d\,\mathcal{O}}\,, \tag{3.2.3}$$

represents the distribution of the observable [28]. The following section includes a selection of observables commonly used during data analysing of detector outputs.

3.2.2 Observables

The focus when conducting analyses is on each *scattering event* (shortened to event) where the beam particles interact. Not all events are of interest to the physics community, and hence great amounts of work has gone into categorising the interesting

events, whilst getting rid of the others. The frequency of each type of event is given by its partial cross-section σ_i, which all add up to the total cross-section $\sigma = \sum_i \sigma_i$. These partial cross-sections can be determined using the *event* or *interaction rate*,

$$\frac{\mathrm{d}N_i}{\mathrm{d}t} = \mathcal{L} \cdot \sigma_{\mathrm{i}}\,, \tag{3.2.4}$$

for *luminosity* $\mathcal{L}$. The luminosity, with units $cm^{-2}s^{-1}$, describes the concentration of particles per area per unit time and is determined by the frequency of the beams, the beam densities (how many particles per beam), and the intensity of the beams. For a collider, the luminosity is measured experimentally, and the total luminosity for the experiment over a period T is the *integrated* luminosity, $L = \int_0^T \mathcal{L}\,\mathrm{d}t$.

In order to describe a system of particles, the *invariant mass* is defined,

$$s_{i,..,n} = (p_i + ... + p_n)^{\mu} \left(p_i + ... + p_n\right)_{\mu}\,, \tag{3.2.5}$$

which contains information about the total energy and momentum of each event [28]. For $2 \to 2$ processes, *Mandelstam variables* are given by

$$s = (p_1 + p_2)^2, \qquad t = (p_1 - p_3)^2, \qquad u = (p_1 - p_4)^2\,, \tag{3.2.6}$$

for incoming particles $p_{1,2}$ and outgoing particles $p_{3,4}$. The transverse momentum of a particle with three-momentum $\vec{p} = \left(p_x, p_y, p_z\right)$ is

$$\vec{p_T} = (p_x, p_y)\,, \tag{3.2.7}$$

defined in the transverse $(x - y)$ plane to the z-axis of the incoming beams. In order to describe the angle of the final state particles in a Lorentz invariant way, the *pseudorapidity* is used,

$$\eta = -\ln\left(\tan\left[\frac{\theta}{2}\right]\right), \tag{3.2.8}$$

where the polar angle θ is the angle between the particle's four-momentum and the z-axis. Here $\eta = 0$ corresponds to a particle travelling perpendicularly to the beams, for $\eta > 0$ it is travelling in the forward region along the $+z$-axis ($\theta \to 0^{\circ}$), and $\eta < 0$

in the backwards region ($\theta \to 180^{\circ}$). The azimuthal angle ϕ is the angle between the transverse (x-y) plane and the z-axis which is Lorentz invariant under boosts along the z-axis [28].

3.2.3 Comparison of Experiments to Theory

As seen throughout this section, particle colliders and detectors are complex experiments, and therefore it is usually not possible to completely describe them theoretically. Many software packages have been developed to solve this, generally called *Monte Carlo event generators* named after the Monte Carlo (MC) statistical method. The event generators simulate particle collisions, producing lists of final state particles with their respective four-momenta given a set of initial conditions. These are constantly under development in order to become more complex theoretically, taking into account higher and higher order of precision [28].

In the following chapters, two MC generators will be used; Pythia [35] and MadGraph [36]. Both programs calculate the matrix amplitude, as described in section 2.6, for processes specified when running the software. Samples of the specified process are created by running the generator with a certain *number of events*, calculating the cross-section for the process considered. Using the luminosity of a collider, one can calculate the expected number of times the process would occur at the collider.

An example of an event in an MC generator can be seen in Figure 3.3, consisting of the incoming hadrons (h), the hard interaction (represented by a grey circle), the production of two particles where one subsequently decays. Finally, the introduction of *initial* and *final state radiation* (ISR and FSR) of gluons are seen in orange, which are carried out by the *parton shower*. Additionally, one has to consider secondary interactions of the remaining partons incoming hadrons, and the final hadronisation and hadron decays of the final states [37]. After the parton shower, the final state particles *hadronise*, forming hadrons which are clustered together into *jets*. These jets consist of groups of hadrons travelling in the same general direction and are

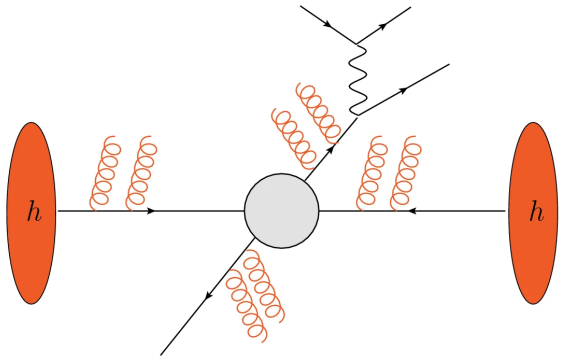

Figure 3.3: Monte Carlo event with incoming particles, primary hard interaction, decay of heavy particle, and parton showering (from [37]).

the objects detected in particle collider detectors [12]. One can visualise how the two particles produced in the hard interaction in Figure 3.3, with subsequent parton showers, will form two measurable jets. Due to momentum conservation, the particles emitted will generally travel in the same direction as the particle, which they were emitted from.

The basics of particle colliders and their detectors have now been introduced. In order to describe the more intricate details of detectors, two examples of detectors will be presented.

3.3 SuperKEKB & Belle II

KEK is the *High Energy Accelerator Research Organisation* in Japan which hosts KEKB, an asymmetric-energy electron-positron collider, where the Belle detector is located. It is called a *B-factory* as its centre-of-mass energy ($\sqrt{s} = 10.58$ GeV) is equal to the mass of the $\Upsilon(4S)$ resonance, which decays into two B mesons. This leads to a large amount of B-mesons being produced, and their interactions can therefore be studies in-depth [38]. The experiment was built to study CP violations in B meson decays [39], and for the general investigation of flavour physics, such as radiative decays $b \to s\gamma$ [40]. SuperKEKB and Belle II are the upgrades of KEKB and Belle, with much increased luminosity and improved detector setup [38].

The SuperKEKB accelerator has beam energies of 7.0 and 4.0 GeV for the electron and positron beams respectively. The asymmetric beam energy is designed for the production and decay of B-mesons; for equal beam energies, the mesons would be produced almost at rest and a large proportion would decay into back-to-back decay products travelling down the beam pipes outside the detector range. With unequal beam energies, the B-mesons are produced with a large boost and therefore travel further before decaying. The decay vertices will be separated and the decay products easier to detect and distinguish [41].

The lab frame z-axis of the detector is found at the bisect of the angle between the direction of the incoming electron beam and the reverse direction of the incoming positron beam. There is a 41.5 mrad (2.37°) crossing angle between the lab frame and the beams [42].

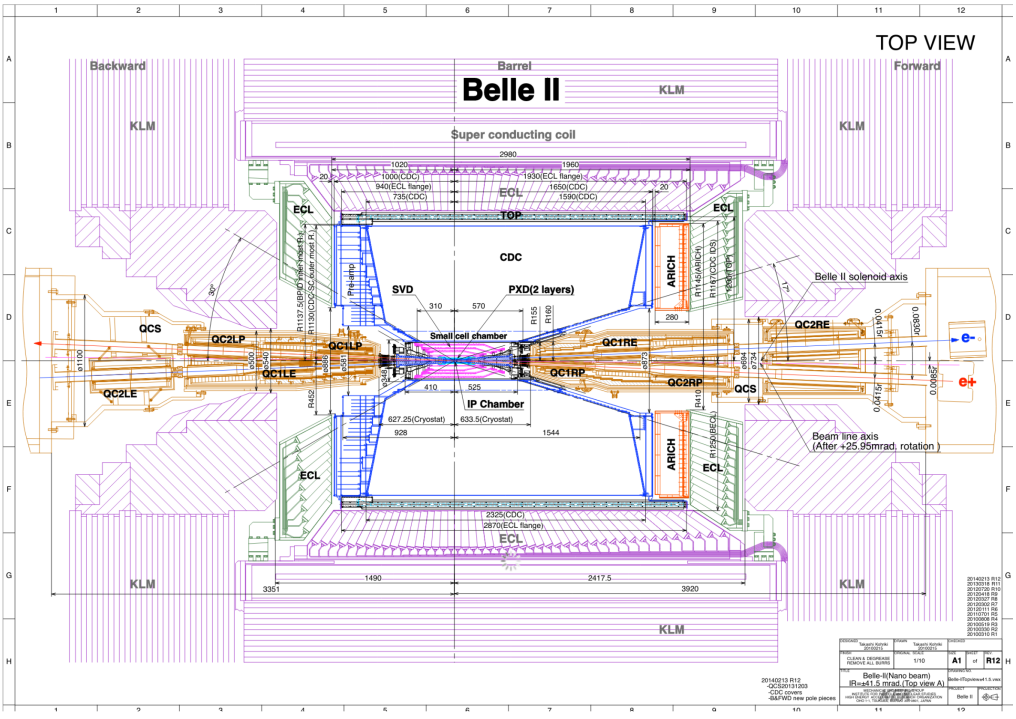

Figure 3.4: Schematics of Belle II, further detail in text (from [40]).

3.3.1 Detector Components

Figure 3.4 displays the top view of the Belle II detector with all of its components where the main ones will be described in this section. The detector has two main parts: the barrel and two end-caps in the forwards and backwards directions.

At the core of the detector, immediately surrounding the interaction point, the Vertex Detector (VXD) consists of the silicon Pixel Detector (PXD) and Silicon Vertex Detector (SVD). All together, they determine the position of the vertices which is used to distinguish particles that produced at the interaction point, from ones that were produced from particles which travelled before decaying [40]. The track reconstruction is carried out through charged particles ionising strips of silicon, the individual hits can then be reconstructed into tracks [28]. The Central Drift Chamber (CDC) is pictured as a large empty volume in Figure 3.4, and acts as the central tracking device for the detector [40]. Here, using a magnetic field, the path of charged particles becomes curved, and hence positive, negative, and neutral particles can be distinguished. This also allows for the identification of particles and their anti-particles [28].

An important matter in detectors is the identification of particles, in Belle II this is carried out by the time-of-propagation (TOP) detector component in the main barrel and the Aerogel Ring Imaging Cherenkov (ARICH) counters in the forward end-cap regions. The ARICH is specifically designed to distinguish between pions and kaons. These can be seen in cyan and orange in Figure 3.4. The identification is done through the detection of Cherenkov radiation. Continuing radially from the IP, the Electromagnetic Calorimeter (ECL) is present in both the barrel and end-caps. It detects gamma rays and identifies particles through the energy deposits in the material from the parton showers. Similarly, the K_L^0 and muon detector (KLM) detects hadronisation showers [40]. All together, the components of the detector provide a series of hits along the path of each particle which are reconstructed into tracks [28].

Angular Coverage

The components described above each have an angular coverage due to their finite width. The ECL has the largest cover with $12.4^\circ < \theta^{\text{lab}} < 155.1^\circ$, where there are gaps between the endcaps and the barrel at $31.4^\circ < \theta^{\text{lab}} < 32.2^\circ$ and $128.7^\circ < \theta^{\text{lab}} < 130.7^\circ$. The gaps exist to make room for cables to reach the inner parts of the detector. With unequal beam energies, the mesons are boosted in the direction of travel of the incoming, more energetic, electron. The decay products will acquire the same boost, and therefore to capture the largest number of the decay products the angular coverage is asymmetric in the direction of the boost, providing the largest opportunity of detection.

Any particle outside the angular coverage, travelling down the beam pipe or in the gaps, will not be detected and shows up as missing energy. Other sources of missing energy are the loss of particles to small gaps in the mechanical structure of the detector and the gaps between crystals in the end-caps, though these are minor compared to the angular coverage loss. Finally, the components of Belle II are not able to detect neutrinos, which therefore is an additional source of missing energy [40].

3.3.2 Chiral Belle Programme

The Chiral Belle Programme aims to upgrade the collider to have left and right longitudinal polarisation of approximately 70% for the electron beam and an unpolarised positron beam. The beam polarisation will be measured with a precision of better than $\pm 0.5\%$, and each beam will have average electron beam polarisation of

$$\langle \text{Pol} \rangle = \frac{1}{2} \left[\left(\frac{N_{eR} - N_{eL}}{N_{eR} + N_{eL}} \right)_{\boldsymbol{R}} - \left(\frac{N_{eR} - N_{eL}}{N_{eR} + N_{eL}} \right)_{\boldsymbol{L}} \right], \tag{3.3.1}$$

where $N_{eR,eL}$ is the number of right/left-handed electrons in the event samples with electron beam bunches with either left ($\boldsymbol{L}$) or right ($\boldsymbol{R}$) polarisation [43].

With one polarised beam, Belle II will be able to uniquely measure electroweak

parameters to unprecedented precision [38]. One such possibility is presented here. The left-right asymmetry for processes $e^+e^- \to f\bar{f}$ with $f \in b, c, \tau, \mu, e$ is given by

$$A_{LR}^f = \frac{\sigma_L^f - \sigma_R^f}{\sigma_L^f + \sigma_R^f}\,, \tag{3.3.2}$$

where $\sigma_{L/R}^f$ are the cross-sections for 100% left- and right-handed incoming electron beams respectively. In the SM, the asymmetry is induced by the $\gamma - Z$ mediator interference,

$$e^+e^- \to V \to f\bar{f} \qquad \text{for} \qquad V \in \{\gamma, Z\}\,, \tag{3.3.3}$$

which, at leading order, has a theoretical value given by [44]

$$A_{LR}^f(SM) = \frac{s\,G_F}{\sqrt{2}\pi\alpha Q_f} g_A^e g_V^f\,. \tag{3.3.4}$$

Here s is the centre-of-mass energy, Q_f the electric charge of the fermion, G_F the Fermi constant, g_A^e is the neutral current axial coupling of the electron, and g_V^f the neutral current vector couplings [38].

The asymmetry will be measured at Belle II using

$$A_{LR}^f(\text{meas.}) = \frac{N_L^f - N_R^f}{N_L^f + N_R^f} \langle \text{Pol} \rangle\,, \tag{3.3.5}$$

where $N_{L,R}$ is the number of events for left-handed and right-handed electron beam polarisation [43]. It is expected to achieve a reduction in the error in the measurement of g_V^f of a factor of 4 for b-quarks, 7 for c-quarks, and 3 for muons [38]. Similarly to α_s, see section 2.2.3, the Weinberg angle runs, and it can be shown that the neutral current vector couplings g_V^f are directly related to the Weinberg angle [12].

Figure 3.5 displays the current and proposed measurements of $\sin^2\theta_W$ as a function of the energy scale μ. The Belle II projection, seen as "e- Polarized SuperKEKB" in red, are for $\mathcal{L} = 40\text{ab}^{-1}$. It is worth noting that both the Tevatron and LHC measurements are also at the Z^0-pole around $\mu = 10^2$ GeV together with SLC and LEP1, indicated by the black arrows. The Mainz-P2, Moller, and SoLID experiments are expected to agree with theory but have been moved down for better visibility. It can be seen that the measurements at the Z-pole are very precise and in agreement

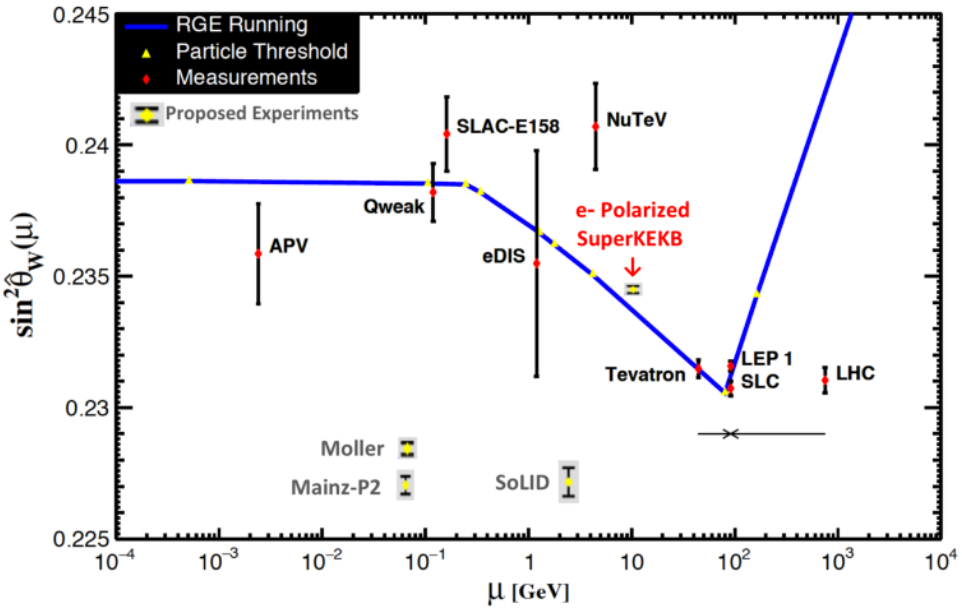

Figure 3.5: Measurements of the running of the Weinberg angle $\sin\theta_W$, see text for detail (from [43]).

with the predicted SM value. But for lower energies, there is slight disagreement between experiments and theory. As $\sin^2\theta_W$ can be modified by the introduction of New Physics it is important to have precise measurements at a range of energies. The Belle II with a polarised electron beam provides a unique measurement between the low and high energy measurements [43].

As described previously, the Chiral Belle Programme will have only one beam polarised as there has yet to be a substantial case for polarising both, but in chapter 6 a compelling proposal shall be outlined.

3.4 ATLAS

The ATLAS (*A Toroidal LHC Apparatus*) detector is located between ALICE (*A Large Ion Collider Experiment*) and LHCb (*LHC-beauty*) at the LHC at CERN. The LHC is currently operating with proton beams of energies up to 6.8 TeV each, resulting in a centre-of-mass energy of $\sqrt{s} = 13.6$ TeV. Initially, ATLAS was intended to search for the theorised but yet to be discovered Higgs boson, together with a

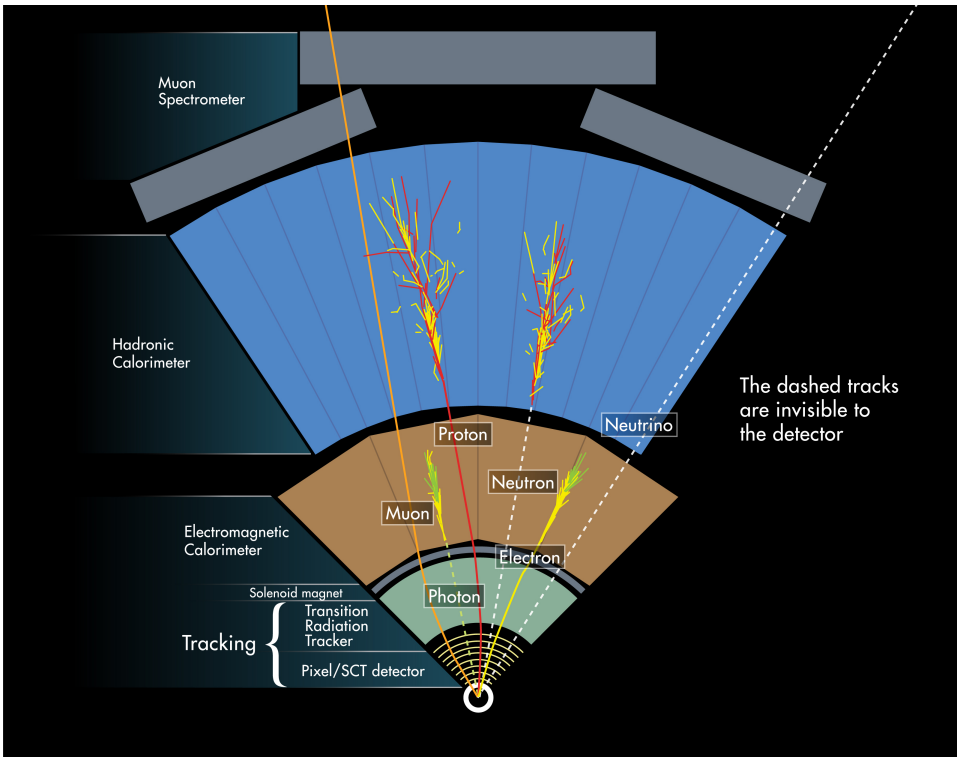

Figure 3.6: Schematics showing particle tracks in each component of the ATLAS detector (from [46]).

plethora of particles predicted by *Supersymmetry* (SUSY). The details of SUSY are beyond the scope of this thesis [45] .

ATLAS has a similar layout to Belle II, as described in section 3.3.1, with the addition of a hadronic calorimeter (HCAL) and the KLM exchanged for a muon spectrometer (MS). The HCAL consists of nuclei with which the produced hadrons interact strongly, causing them to decay and be detected. The MS specialises in measuring muons, which are not sufficiently measured in the inner detector due to their high energy [28]. How six different particles show up in the ATLAS detector depending on their mass and charge is shown in Figure 3.6. Similar diagrams can be constructed for the Belle II detector described previously. The tracks of charged particles are initially curved depending on the sign of their charge. Leptons are stopped through the loss of energy in the ECL, whereas hadrons deposit their energy in the HCAL. It is important to note that neutrinos, as they do not interact very strongly are not detected and will show up only as missing energy.

The MS consists of three layers located at radii 5.0 m, 7.5 m, and 10.0 m away from

the interaction point. In order to achieve correct vertex reconstruction, the particle tracks have to pass through at least two of these layers. Hence, any particle which decays more than 7.5 meters away from the IP in ATLAS will escape the detector without detection [47]. Figure 3.7 displays two separate particles moving in parallel detected by four hits in an arbitrary detector. It can here be seen how, even with hits in two layers, the vertex reconstruction can be incorrect [48].

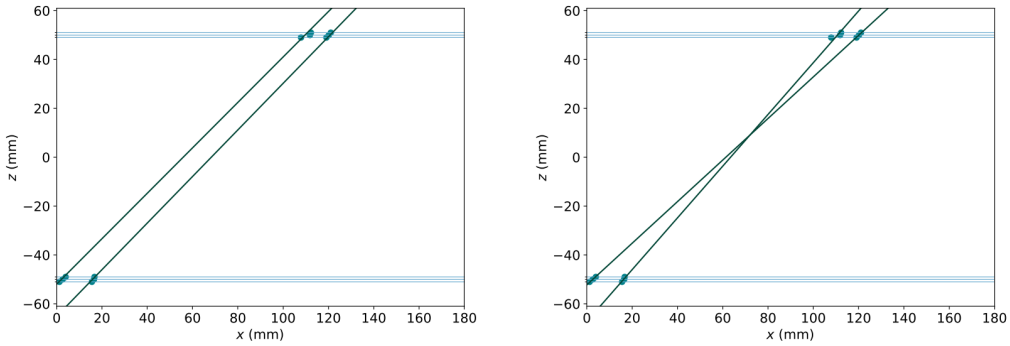

Figure 3.7: Vertex reconstruction for correct (left) and incorrect (right) outcomes (from [48]).

3.5 New Physics Searches

The most commonly used procedures when searching for New Physics in collider experiments can be split into two categories; *implicit* and *explicit*, also known as *direct* and *indirect*. For both, most often the final state detected is not unique and the same can be produced with only SM particles and interactions. This is known as the *SM background* that obscures the *signal* from the New Physics, and these are usually calculated using MC generators, see section 3.2.3, or inferred by looking at existing data from experiments.

Measuring SM processes at very high precision allows searching for processes, where the experimental results do not match the theoretical predictions. This method is the foundation for implicit searches. These searches have broad application but reveals little detail about the underlying New Physics if discrepancies between theory and experiment are found. Generally, implicit searches look for New Physics which,

through appearing in higher-order correction loops, modifies observables such as cross-sections, decay rates, and differential cross-sections. This approach therefore does not require the new particles to have masses below the centre-of-mass of the collider, and the potential mass range is larger than explicit searches.

Explicit searches look for the direct production of new particles, which will reveal more about the involved New Physics. The detection of the new particle depends on its decay modes, which can be categorised into three types of searches.

Resonance searches, where the particle decays promptly, too close to the interaction point to be distinguished. The new particle must decay back into SM particles, either directly or through intermediate New Physics particles. The resonance appears in the distribution of the invariant mass (see eq. (3.2.5)) of the decay products from the new particle. Due to quantum mechanics, the decaying particle's four-momentum can deviate from the relativistic invariant mass formula, and due to detector inefficiencies, the momenta of the decay products will never be measured with 100% accuracy. Together, this causes the invariant mass distribution to be broadened around the mass of the new particle. The possible SM backgrounds result in a smooth continuous invariant mass distribution on which the resonance would be a *bump*. The height and shape of the bump depend on the interactions between the SM and the new particle.

Semi-invisible particle searches are necessary when the new particle decays into one or more invisible particles which leave the detector without decaying or being detected, and therefore show up as missing energy.

If the particle's lifetime is large enough that the particle travels a significant distance before decaying, the decay vertex can be displaced from the IP, or the tracks within the detector can be different to anything predicted by SM. This is known as ***displaced vertex searches***. As described previously, collider detectors have layers of components of finite width, and therefore, depending on the decay length of the particle, the vertex will be placed within one of these layers. This dictates

the relevant SM background for the search, and for certain distances from the IP one can have almost zero background events.

Lastly when the NP particle is stable on collider scales, decaying outside the detector and showing up as missing energy. For these ***missing transverse energy searches***, one selects certain final states to focus on, where either the cross-section is large, or the SM background is small such that the signal stands out.

For all these types of searches, in order to claim that New Physics has been observed, the signal on top of the background has to be statistically different to the background alone. The methods for determining this are described in section 4.3.1.

3.6 Conclusion

The foundations for collider physics have been presented through the introduction of different types of colliders, together with how they facilitate the detection of particles after collision. In particular, the Belle II and ATLAS detectors are reviewed with an overview of their components and layouts. For Belle II, the Chiral Belle Programme aims to polarise the incoming electron beam, and one reason for this plan is described. Methods for analysing the experimental data and comparing the results to the theoretical predictions are discussed . Including examples of the observables used, such as pseudorapidity, and Monte Carlo event generators. Implicit and explicit searches for New Physics at colliders were described.

Particle colliders are an incredibly strong tool for both precisely measuring quantities, such as particle masses and decay widths, and discovering particles predicted by the Standard Model. They have throughout the years not only confirmed theories, but also excluded and disproven many others. By continuously constructing colliders with increasing centre-of-mass energy, particles of higher masses can be produced and studied. The development of detector components, hardware, and software analyses have greatly increased the precision. But there is still plenty left to solve the puzzles of the Standard Model, such as the nature of dark matter.

Chapter 4

Dark Matter

4.1 Introduction

Little is known about the properties of dark matter, which leaves room for many interpretations and models. As seen in Figure 4.1, the mass range considered when looking for dark matter is extremely large, ranging from zepto-eV $\left(10^{-21}\,\text{eV}\right)$ to the Planck scale, $M_{\text{PL}} = 1.22 \times 10^{19}$ GeV. The lower bound is produced from restrictions from dark matter halos of dwarf galaxies where the DM particle's de Broglie wavelength has to be smaller than the size of the halo [50]. Direct detection experiments, such as DEAP which uses liquid argon, has been used to set upper limits on the dark matter mass [51]. These lower and upper bounds are general but can vary depending on the dark matter model considered, for a review see [50]. Fortunately, the mass of the dark matter particle dictates the experiments which are sensitive to the particle. For example, both ultra-light and -heavy dark matter are studied mostly using cosmology and astronomy, whereas $\mathcal{O}(1\,\text{eV}) - \mathcal{O}(1\,\text{TeV})$ DM is considered for lab and collider experiments [3].

This chapter first describes, in section 4.2, the details of the dark matter models considered in this thesis with their general theoretical descriptions and decays. The theories of dark photons, axion-like particles, and heavy neutral leptons are included. Secondly, the approaches for searches for dark matter in particle colliders, together

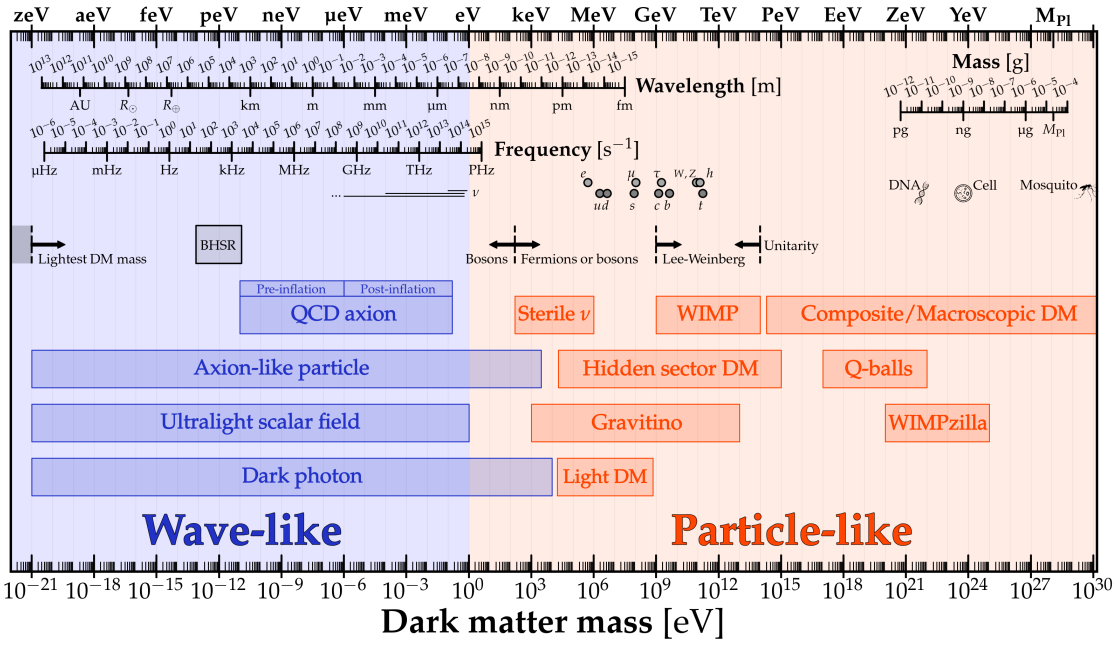

Figure 4.1: Dark matter mass range with categories of models (from [49]).

with the procedure to extract information from the results, are presented in section 4.3. Finally, section 4.4 displays the current limits and projections on the models presented in section 4.2.

4.2 Dark Matter Models

Dark matter can be implemented through a plethora of mechanisms, which vary in terms of particle content, complexity, and possible interactions with the Standard Model particles. In general, the type of dark matter particle follows the ones presented in the SM, (pseudo-)scalar and (pseudo-)vector, where the couplings to the SM are restricted by the model and implementation. Five popular theoretical mechanisms for DM are very heavy DM (masses above TeV scale), *sterile* or *right-handed* neutrinos (RHNs), *weakly interacting massive particles* (WIMPs) , *axions* or *axion-like particles* (ALPs), and *hidden sector* particles and mediators [7]. Many of these models can be found in Figure 4.1 with representative masses, though it is worth noting that the mass ranges displayed are not exact, and one finds many

examples of these models outside these ranges.

For future use, the concept of effective field theories will briefly be introduced. The foundation of EFTs is the principle that one can perform calculations without knowing the full, exact underlying theory; approximations and simplifications can be made to obtain an effective theory.

The Lagrangian of mass dimension d for an arbitrary EFT is given by

$$\mathcal{L}_{\text{EFT}} = \sum_{\mathcal{D}\geq 0,i} \frac{c_i^{(\mathcal{D})}\mathcal{O}_i^{(\mathcal{D})}}{\Lambda^{\mathcal{D}-d}}\,, \tag{4.2.1}$$

where the sum is over all possible operators $\mathcal{O}_i^{(\mathcal{D})}$ of dimension $\mathcal{D}$ with coefficient $c_i^{(\mathcal{D})}$. The operators are constructed of the fields of the EFT, for example in SMEFT the operators has only SM fields. For the coefficients $c_i^{(\mathcal{D})}$ to be dimensionless, the scale Λ is introduced, which is the scale at which New Physics occurs. Therefore, if the scale is large, the higher order contributions are suppressed. For $d = 4$ space-time dimensions,

$$\mathcal{L}_{\text{EFT}} = \mathcal{L}_{\mathcal{D}\leq 4} + \frac{\mathcal{L}_5}{\Lambda} + \frac{\mathcal{L}_6}{\Lambda^2}\,, \tag{4.2.2}$$

it can be seen that the EFT Lagrangian can be understood as an expansion in powers of $\frac{1}{\Lambda}$ [52].

Hidden sectors have one or more dark matter particles weakly interacting with the SM through a *portal*, which will be described in further detail in the following section. This allows the DM particle(s) to have masses below the EW scale[1], even though this mass range has already been explored by experiments [2]. These models are therefore popular as they do not require the construction of new colliders. Alternatively, the masses of the DM particle(s) may be much larger than the EW scale and therefore outside the reach of current experiments [2]. For the remainder of this thesis, the focus shall be on portal dark matter models.

[1] $v_H = (\sqrt{2}G_F^0)^{-1/2} \simeq 246.22$ GeV for the Higg's vev and G_F^0 the tree-level Fermi constant [2].

4.2.1 Portals

Portals between the SM and a dark sector have Lagrangians given by

$$\mathcal{L} \supset \sum_{k,l,n}^{k+l=n+4} \frac{\mathcal{O}_{\mathrm{SM}}^{(l)} \mathcal{O}_{\mathrm{DS}}^{(k)}}{\Lambda^n}, \tag{4.2.3}$$

for cutoff scale Λ, and current $\mathcal{O}_{\mathrm{SM}}$ and $\mathcal{O}_{\mathrm{DS}}$ consisting of only SM and dark sector fields respectively. Here, the sum is over all possible combinations of the fields in the SM and dark sector. In general, the currents can have a number of different Lorentz presentations, but $\mathcal{O}_{\mathrm{SM}}$ is gauge invariant under all SM symmetries [53].

For dimension-4 currents with $n = 0$, there are three well-known examples of portals which have the lowest dimension SM currents; vector (section 4.2.2), scalar (Appendix A), and lepton (section 4.2.4). The corresponding SM currents are $F_{\mu\nu}, H^\dagger H$, and LH with mass dimension 2,2, and $\frac{5}{2}$ respectively. Here $F_{\mu\nu}$ is the hypercharge field strength, H the Higgs doublet, and L the lepton doublet. These currents couple the dark sector to the SM without the introduction of a New Physics mass scale [53]. The three portals mix with one SM particle, and therefore bounds are straightforwardly put on each model. If the mixing is too strong observables, such as the masses and decay widths of the SM particles, would differ significantly from the values measured experimentally.

On their own, the portals can be viable dark matter models, accounting for the total density of dark matter described in section 1.1, where either the mediator particle or the new dark sector particles act as DM. However, the portals themselves do not solve the problems present in the SM; they are simplifications of more complex theories for dark matter which do address these problems. The more complex models will take the place of the portal models eventually. The advantage of the portal framework is that one can often construct models with two parameters, for which exclusion limits and projections can easily be found. The projections can be used to compare current and future experiments and proposals, and highlight parameter spaces of special interest which should be investigated experimentally [7].

In the following section, three different dark matter models are presented with the wider theories in which they lie. Section 4.2.2 describes *dark photons*, whereas *axion-like particles* (ALPs) are presented in section 4.2.3, and *heavy neutral leptons* (HNLs) in section 4.2.4. Together with a dark scalar portal, briefly described in Appendix A, these make up the Feebly-Interacting Particles (FIPs) portals presented in [54], see section 5.5.1 for further detail. The ALP is not a portal model as it is suppressed by a decay constant, but it is included as it often acts as a mediator to a wider dark sector [54].

4.2.2 Dark Photons

The dark photon (also known as the *hidden photon*) was originally introduced to be the gauge boson of a new $U(1)_X$ gauge group added to the SM, which kinetically mixed with the SM photon of $U(1)_{\text{EM}}$. But as this would have occurred after EWSB, the mixing cannot be fundamental [54]. Therefore, it has since then become more common to have the dark gauge boson mix with the hypercharge boson associated with $U(1)_Y$. The simplest model for dark photons will be presented first, which is used for the portal framework.

Minimal Kinetic Mixing

The Lagrangian for the gauge boson X_μ of the new $U(1)_X$ group and hypercharge boson B_μ is given by

$$\mathcal{L} \supset -\frac{1}{4}W_\mu^3 W^{3\mu} - \frac{1}{4}B_\mu B^\mu - \frac{1}{4}X_\mu X^\mu + \frac{1}{2}m_X^2 X^\mu X_\mu - \frac{\epsilon}{2\cos\theta_W}B_{\mu\nu}X^{\mu\nu}\,, \quad (4.2.4)$$

for mixing parameter ϵ of the kinetic mixing, dark gauge boson mass m_X, and Weinberg angle θ_W [31]. The kinetic terms for two of the four gauge bosons of the

SM, W_μ^3 and B_μ, have been included as they mix with X_μ,

$$\begin{pmatrix} W_\mu^3 \\ B_\mu \\ X_\mu \end{pmatrix} = \begin{pmatrix} \cos\theta_W & \sin\theta_W & -\epsilon\sin\theta_W \\ -\sin\theta_W & \cos\theta_W & -\epsilon\cos\theta_W \\ \epsilon\tan\theta_W & 0 & 1 \end{pmatrix} \begin{pmatrix} Z_\mu \\ A_\mu \\ A'_\mu \end{pmatrix}, \tag{4.2.5}$$

where A_μ and Z_μ are the SM electroweak photon and Z-boson, and A'_μ is the dark photon field. Using the mixing matrix, the kinematic terms in the mass eigenstate Lagrangian are

$$\mathcal{L} \supset -\frac{1}{4}A_\mu A^\mu - \frac{1}{4}Z_\mu Z^\mu - \frac{1}{4}A'_\mu A'^\mu + \mathcal{O}(\epsilon^2)\,. \tag{4.2.6}$$

The mixing matrix consists of the EWSB mixing matrix, see eq. (2.4.6),

$$V_{\text{EWSB}} = \begin{pmatrix} \cos\theta_W & \sin\theta_W & 0 \\ -\sin\theta_W & \cos\theta_W & 0 \\ 0 & 0 & 1 \end{pmatrix}, \tag{4.2.7}$$

and the new dark mixing matrix,

$$V_\epsilon = \begin{pmatrix} 1 & 0 & 0 \\ 0 & 1 & -\epsilon \\ \epsilon\tan\theta_W & 0 & 1 \end{pmatrix}. \tag{4.2.8}$$

due to the photon-fermion current J^μ_{EM}, as previously seen in eq. (2.4.14),

$$\mathcal{L} \supset -eJ^\mu_{\text{EM}}A_\mu\,, \tag{4.2.9}$$

after mixing the dark photon couples to the SM fermions through a rescaling of the photon coupling to fermions,

$$\mathcal{L} \supset -e\epsilon J^\mu_{\text{EM}}A'_\mu\,. \tag{4.2.10}$$

As the mixing parameter ϵ is small, this gives rise to the name dark or hidden photon [55]. An advantage of this simplified model is that it only contains two new parameters: the mixing parameter ϵ and the mass m_X [56].

General Kinetic Mixing

The simplified kinetic mixing can be extended by including the possibility that the fermions of the SM are charged under the new $U(1)_X$ group, and thus the dark photon directly interacts with the SM through the current j_μ^X with coupling constant g_X. The general Lagrangian for a $U(1)_X$ group with an associated kinetically mixing dark photon is

$$\mathcal{L} = -\frac{1}{4}\hat{F}_{\mu\nu}\hat{F}^{\mu\nu} - \frac{\epsilon'}{2}\hat{F}_{\mu\nu}\hat{X}_{\mu\nu} - \frac{1}{4}\hat{X}_{\mu\nu}\hat{X}^{\mu\nu} - g' j_\mu^Y \hat{B}_\mu - g_X j_\mu^X \hat{X}_\mu - \frac{1}{2}\hat{M}_X^2 \hat{X}_\mu \hat{X}^\mu \quad (4.2.11)$$

for the hypercharge $\hat{B}_\mu$ and dark photon $\hat{X}_\mu$ fields, where $\hat{X}$ refers to the fact that the fields have yet to be normalised. Each have associated field strength tensors $\hat{F}_{\mu\nu} = \partial_\mu \hat{B}_\nu - \partial_\nu \hat{B}_\mu$ and $\hat{X}_{\mu\nu}$ defined similarly. $\hat{B}_\mu$ has coupling g' and current j_μ^Y, whereas the new dark matter gauge boson has coupling g_X and mass $\hat{M}_X$.

The current j_μ^X depends on the $U(1)_X$ group considered, where three examples are

$$j_\mu^X = 0\,, \quad (4.2.12)$$

$$j_\mu^{i-j} = \overline{L}_i \gamma_\mu L_i + \bar{l}_i \gamma_\mu l_i - \overline{L}_j \gamma_\mu L_j - \bar{l}_j \gamma_\mu l_j \qquad i \neq j = e, \mu, \tau\,, \quad (4.2.13)$$

$$j_\mu^{B-L} = \frac{1}{3}\overline{Q}\gamma_\mu Q + \frac{1}{3}\overline{u}_R \gamma_\mu u_R + \frac{1}{3}\overline{d}_R \gamma_\mu d_R - \overline{L}\gamma_\mu L - \bar{l}\gamma_\mu l - \overline{\nu}_R \gamma_\mu \nu_R\,. \quad (4.2.14)$$

Firstly, $j_\mu^X = 0$ corresponds to the simplified model described above, $U(1)_{L_i - L_j}$ is the gauged lepton number difference with associated current j_μ^{i-j}, and similarly for the gauged baryon-lepton number difference $U(1)_{B-L}$ [57].

Following the procedure described in Appendix A of [57], through the modified covariant derivative,

$$D_\mu = \partial_\mu - i\left(\frac{g}{2}\tau^a \hat{W}_\mu^a - \frac{g'}{2}\hat{B}_\mu - \frac{g_X}{2}\hat{X}_\mu\right)\,, \quad (4.2.15)$$

the Higgs kinetic term, $(D^\mu H)^\dagger (D_\mu H)$, after EWSB becomes

$$\mathcal{L} \supset \frac{1}{2}\frac{v_H^2}{4}\left[g^2 (W_\mu^1)^2 + g^2 (W_\mu^2)^2 + \left(-g\hat{W}_\mu^3 + g'\hat{B}_\mu + \frac{2}{\nu}g_X \hat{X}_\mu\right)^2\right]\,, \quad (4.2.16)$$

where $\hat{B}_\mu$ and $\hat{W}_\mu^a$ are the $U(1)_Y$ and $SU(2)_L$ gauge bosons and the Higgs field has

been left out. The normalised fields are found from the rotation given by

$$\begin{pmatrix} \hat{B}_\mu \\ \hat{W}^3_\mu \\ \hat{X}_\mu \end{pmatrix} = G(\epsilon') \begin{pmatrix} B_\mu \\ W^3_\mu \\ X_\mu \end{pmatrix} \qquad \text{for} \qquad G(\epsilon') = \begin{pmatrix} 1 & 0 & -\frac{\epsilon'}{\sqrt{1-(\epsilon')^2}} \\ 0 & 1 & 0 \\ 0 & 0 & \frac{1}{\sqrt{1-(\epsilon')^2}} \end{pmatrix} . \tag{4.2.17}$$

To find the mass eigenstates, the fields are again rotated resulting in interactions of the dark photon, SM photon, and Z boson, given by Lagrangian

$$\mathcal{L} \supset \left(e j_{\text{EM}}, \frac{e}{\sin\theta_W \cos\theta_W} j_Z, g_X j^X \right) K \begin{pmatrix} A \\ Z \\ A' \end{pmatrix} , \tag{4.2.18}$$

for currents j_{EM} and j_Z as described previously in section 2.4, current j^X with coupling g_X, $\epsilon = \epsilon' \cos\theta_W$,

$$K = \begin{pmatrix} 1 & 0 & -\epsilon \\ 0 & 1 & 0 \\ 0 & \epsilon \tan\theta_W & 1 \end{pmatrix} + \mathcal{O}\left(\epsilon\delta, \epsilon^2\right), \quad \text{and} \quad \delta = \frac{\hat{M}^2_{A'}}{\hat{M}^2_Z} . \tag{4.2.19}$$

Here θ_W is the Weinberg angle, and the masses $\hat{M}_{A',Z}$ are given by the Z boson and dark photon masses,

$$M^2_Z = \hat{M}^2_Z \left(1 + (\epsilon')^2 \sin^2\theta_W [1 + 2\delta]\right) + \mathcal{O}(\delta^2 [\epsilon']^2) , \tag{4.2.20}$$

$$M^2_{A'} = \hat{M}^2_X \left(1 + (\epsilon')^2 [1 - \sin^2\theta_W (1 + \delta)]\right) + \mathcal{O}(\delta^2 [\epsilon']^2) . \tag{4.2.21}$$

Hence the masses are unchanged to leading order in ϵ'. The couplings of the SM photons are untouched, the Z boson has a new coupling to j^X, and the dark photon couples to both j_{EM} and j^X.

In particular, and of interest to chapter 6, the $U(1)_{B-L}$ gauge group has the coupling to fermions arise from the current j_X, defined in eq. (4.2.14), without the existence of kinetic mixing ($\epsilon' = 0$). Here the coupling between the dark photon and the SM

leptons is given by

$$\mathcal{L} \supset -g_x X_\mu \sum_{e,\mu,\tau} \left(\overline{L}\gamma^\mu L + \bar{l}\gamma^\mu l \right) , \tag{4.2.22}$$

for coupling constant g_X for the current j_X.

Dark Photon Decays

When considering kinetic mixing, the dark photon inherits the couplings of the SM photon. Therefore, the decay widths for the dark photon into charged SM leptons are given by the couplings of the SM photon, where the coupling is replaced by $\alpha \to \alpha\epsilon^2$. For example, the width for the dark photon decaying into an electron pair is given by

$$\Gamma_{A' \to e^+e^-} = \frac{g_X^2 \sqrt{M_X^2 - 4m_e^2} \left(2m_e^2 + M_X^2 \right)}{12\pi M_X^2} \overset{m_e \to 0}{\approx} \frac{g_X^2 M_X}{12\pi} . \tag{4.2.23}$$

As described in section 2.2.3, when quarks are produced with low momenta they form hadrons, and therefore the decays into leptons and quarks are considered separately. The hadronic decay widths can be determined using

$$\Gamma_{A' \to \text{hadrons}}(m_{A'}) = \Gamma_{A' \to \mu^+\mu^-} \times \mathcal{R}_\mu(m_{A'}) , \tag{4.2.24}$$

where $\Gamma_{A' \to \mu^+\mu^-}$ is the decay width of the dark photon into a muon pair. Through the ratio of the cross-sections of e^+e^- annihilation into hadronic final states and muon pairs,

$$\mathcal{R}_\mu(m_{A'}) = \frac{\sigma(e^+e^- \to \text{hadrons})}{\sigma(e^+e^- \to \mu^+\mu^-)} , \tag{4.2.25}$$

the dark photon decay into muons is re-scaled to take into account the hadronic resonances [58]. The values of $\mathcal{R}_\mu(m_{A'})$ are displayed in Figure 4.2 as a function of the centre-of-mass energy $\sqrt{s}$, where the resonances for each meson state are distinct peaks [2].

Summing over all available decay channels, one can calculate the total width and decay length of the dark photon as a function of the mixing parameter ϵ and mass M_X. As seen in Figure 4.3, as the mass increases, the decay length decreases, and

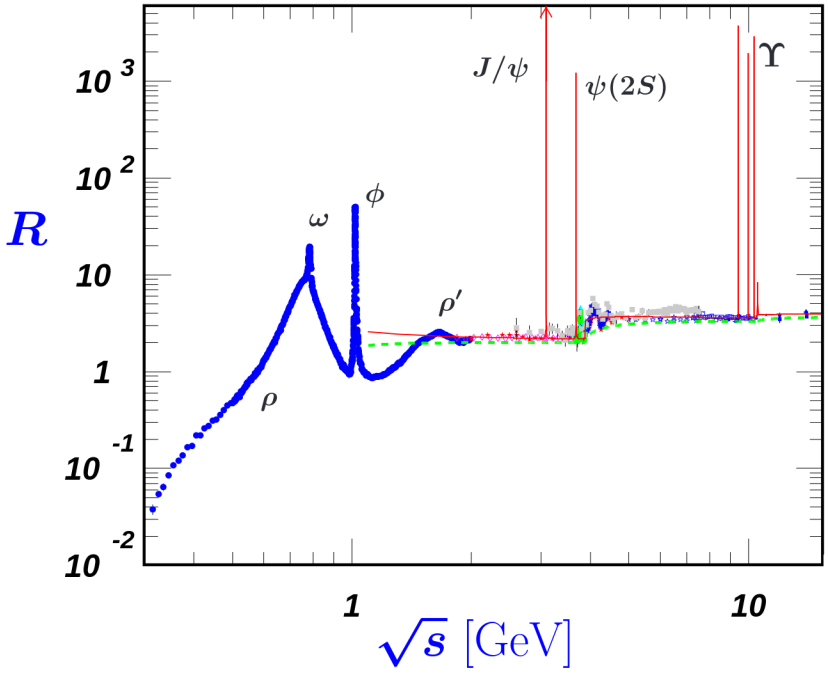

Figure 4.2: e^+e^- hadronic annihilation cross-section ratio, see text for details (from [2]).

similarly for increasing coupling constant as the dark photon interacts more strongly.

Following the methods described in section 2.6.3, the decay length was found using

$$\lambda = \frac{|\vec{p}(m_X)|}{m_X} c\tau \qquad \text{for} \qquad |\vec{p}(m_X)| = \frac{s - m_x^2}{2\sqrt{s}} \qquad \text{and} \qquad \tau = \frac{\hbar}{\Gamma}\,. \tag{4.2.26}$$

Here $e^+e^- \to \gamma + X$ processes at Belle II, see section 3.3 for further detail, were considered, and the total width Γ is found using the decay width formula described above. At tree-level, the $2 \to 2$ process fixes the energy of the outgoing photon, and therefore its momentum, to be a function of the center-of-mass energy and dark photon mass [31].

The irregularities seen in Figure 4.3 around 1 and 5 GeV are due to decays into hadronic states, and the dip around 0.2 GeV is due to the decay channel $A' \to \mu^+\mu^-$ becoming available $\left(2 \times m_\mu \approx 0.2\,\text{GeV}\right)$. All decays in the region above the purple line at 0.2 cm are effectively prompt decays, between the purple and green (0.9 cm) lines the decay vertex is inside the beam pipe. The region between the green and

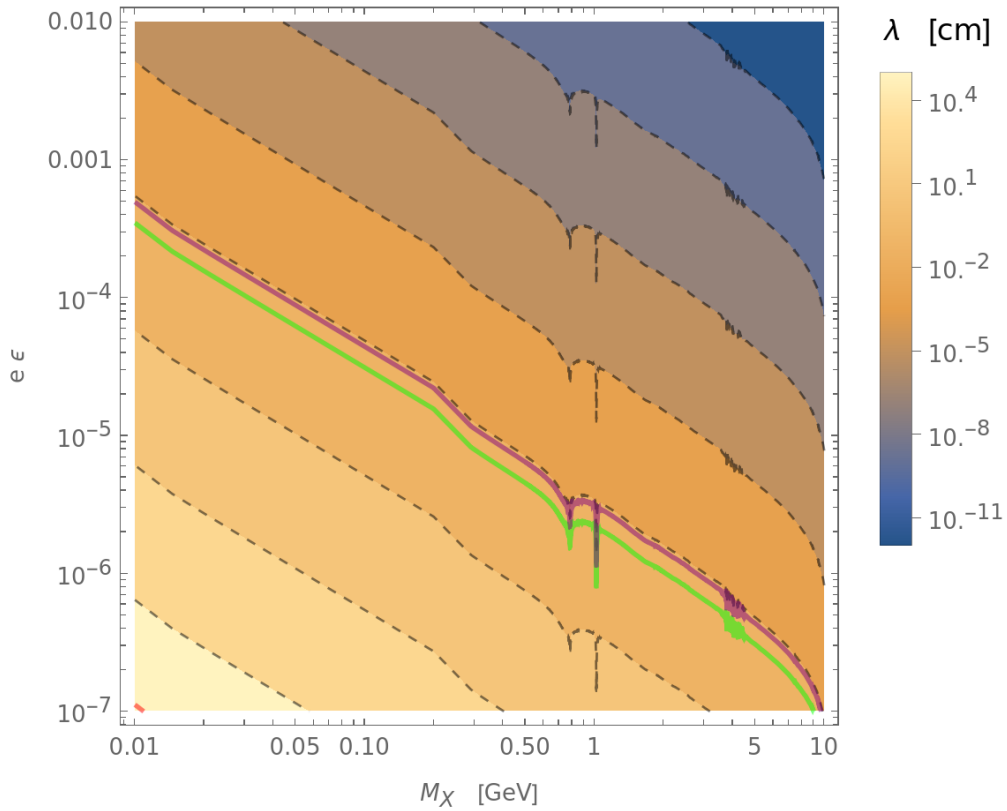

Figure 4.3: Decay length as a function of dark photon mass and mixing parameter, the purple, green and red lines are at 0.2, 0.9, and 17 cm respectively, see details in text.

red (17 cm) line, which can faintly be seen in the left-hand lower corner, is inside the vertex detector (VXD) part of the detector. Each section of parameter space has different SM backgrounds to consider, and hence when considering a displaced vertex search one has to make an educated choice of parameter values [59]. For smaller masses and couplings, the decay length increases, and similarly for larger boosts, the lifetimes and decay lengths increase and eventually the particle completely escapes the detector before decaying.

4.2.3 Axion-Like Particles

Axion-like particles are pseudo-scalar particles with a broad mass range from as low as 10^{-20} eV to over 10^{3} GeV. The fields of astronomy and cosmology are interested in very light ALPs, whereas the collider searches described in this thesis will focus on masses between 10^{-2} and 10 GeV. ALPs have strong theoretical motivations and

are included in many models [60]. The name originates from the axion which was introduced as a solution to the *strong CP problem* [60].

The Strong CP Problem

Using gluon fields, the only term not included in the QCD Lagrangian that obeys the gauge symmetries of the QCD Lagrangian is

$$\mathcal{L}\supset -\theta\frac{\alpha_s}{8\pi}G^a_{\mu\nu}\tilde{G}^{\mu\nu}_a\,, \tag{4.2.27}$$

for α_s the strong coupling constant, a constant θ, and gluon field strength tensor $G_{\mu\nu}$ and its dual $\tilde{G}^{\mu\nu} = \frac{1}{2}\epsilon^{\mu\nu\sigma\gamma}G_{\sigma\gamma}$ [60]. This CP violating term results in an electric dipole moment for the neutron proportional to θ. Experimentally, the neutron electric dipole moment has been measured to be very small, implying that $|\theta| \lesssim 10^{-10}$. However, theoretically there is no motivation for the smallness of θ, and this has therefore been named the *strong CP Problem* [2].

The axion, also known as the QCD axion, is introduced in the Lagrangian,

$$\mathcal{L}\supset \left(\frac{a}{f_a}-\theta\right)\frac{\alpha_s}{8\pi}G^a_{\mu\nu}\tilde{G}^{\mu\nu}_a\,, \tag{4.2.28}$$

using its field a and decay constant f_a related to the scale of the New Physics associated with the axion. The axion field acquires a minimum at $a = \theta f_a$, hence solving the strong CP problem and the smallness of the term in the Lagrangian. Through calculations that are beyond the scope of this thesis, it can be shown that the axion mass and decay constant are related through its mixing with mesons,

$$m_A = 5.691(51)\left(\frac{10^{12}\,\mathrm{GeV}}{f_a}\right)\,\mathrm{meV}\,, \tag{4.2.29}$$

restricting the parameter space available. Therefore, the more general axion-like particle, which does not satisfy the criteria related to the axion, was introduced [2].

General Axion-Like Particle Lagrangian

The general effective dimension-5 Lagrangian for ALPs is given by

$$\mathcal{L}_{\text{eff}} \supset \frac{1}{2}\left(\partial_\mu a\right)\left(\partial^\mu a\right) + \frac{\partial_\mu a}{f_a}\sum_f \frac{c_f}{2}\bar{f}\gamma_\mu\gamma^5 f + c_{\tilde{G}}\mathcal{A}_{\tilde{G}} + c_{\tilde{W}}\mathcal{A}_{\tilde{W}} + c_{\tilde{B}}\mathcal{A}_{\tilde{B}}\,, \tag{4.2.30}$$

for couplings to the Standard Model with operators,

$$\mathcal{A}_{\tilde{B}} = -B_{\mu\nu}\tilde{B}^{\mu\nu}\frac{a}{f_a}, \qquad \mathcal{A}_{\tilde{W}} = -W^a_{\mu\nu}\tilde{W}^{\mu\nu,a}\frac{a}{f_a}, \qquad \mathcal{A}_{\tilde{G}} = -G^a_{\mu\nu}\tilde{G}^{\mu\nu,a}\frac{a}{f_a}\,, \tag{4.2.31}$$

for field strength tensors $B_{\mu\nu}$, $W^a_{\mu\nu}$, and $G^a_{\mu\nu}$ for the weak vector bosons and gluons respectively [61]. The coupling to fermions is assumed to be flavour-diagonal, and the couplings to leptons and quarks are assumed equal, $c_l = c_q = c_f$. As alluded to previously, the ALP is not a portal model as its couplings are suppressed by its decay constant f_a.

For future use in chapters 6 and 5, the couplings between ALPs, photons, fermions, and gluons will now be shown. For other couplings and further details see [61].

After EWSB, the coupling between ALPs and photons,

$$\mathcal{L} \supset -c_\gamma\frac{a}{f_a}F_{\mu\nu}\tilde{F}^{\mu\nu} \quad \text{for} \quad c_\gamma = \left(c_{\tilde{B}}\cos^2\theta_W + c_{\tilde{W}}\sin^2\theta_W\right)\,, \tag{4.2.32}$$

has contributions from both the $\mathcal{A}_{\tilde{B}}$ and $\mathcal{A}_{\tilde{W}}$ operators, where θ_W is the Weinberg angle. The ALP-fermion interaction can be rewritten using the equations of motion,

$$\frac{c_f}{2}\frac{\partial_\mu a}{f_a}\,\bar{f}\gamma_\mu\gamma^5 f = -i\,c_f\,m_f\frac{a}{f_a}\bar{f}\gamma_5 f\,, \tag{4.2.33}$$

for fermion masses m_f. The coupling to gluons come straightforwardly from the Lagrangian,

$$\mathcal{L} \supset -c_{\tilde{G}}\,\frac{a}{f_a}\,G^a_{\mu\nu}\tilde{G}^{a\mu\nu}\,. \tag{4.2.34}$$

Here it is worth noting that the ALP coupling to gluons is not the QCD axion coupling and therefore $c_{\tilde{G}} \neq \frac{\alpha_s}{8\pi}$. As seen earlier, coupling constants can depend on the energy scale at which they are measured, see section 2.2.3. Hence, through the inclusion of higher-order loops, the QCD axion, which only couples to gluons, will

generically also interact with photons and fermions [62].

Axion-Like Particle Decays

Without considering loop corrections, the width for the ALP decaying to two photons is given by

$$\Gamma(a \to \gamma\gamma) = \frac{c_\gamma^2 m_a^3}{4\pi f_a^2}\,, \tag{4.2.35}$$

where m_a is the mass of the axion. The decay width of an ALP to an electron pair, at tree level,

$$\Gamma(a \to e^+e^-) = \frac{c_e^2 m_e^2 \sqrt{m_a^2 - 4m_e^2}}{8\pi f_a^2} \overset{m_e \ll m_a}{\approx} \frac{c_e^2 m_e^2 m_a}{8\pi f_a^2}\,, \tag{4.2.36}$$

depends on the mass of the electron. When considering loops, the couplings run at different energy scales and each decay channel depends on all coupling constants introduced, from for example fermion or boson loops. The specifics of the higher order corrections are beyond the scope of this thesis, see [63] for further detail.

As several decay channels are present, the decay length of the ALP is more complicated than the one found above for the dark photon; it depends on the ratio of the various couplings compared to each other. For similar values of the coupling constants, the decay length of the ALP is similar to that of the dark photon.

4.2.4 Heavy Neutral Leptons

Heavy Neutral Leptons (HNLs), also known as right-handed or sterile neutrinos, are often introduced in order to solve the problem of neutrino oscillations and masses through the *seesaw mechanism* [7]. The new right-handed neutrino fields are singlets under $SU(2)_L \times U(1)_Y$ and mix with the SM neutrinos [64].

Simplified Model

A simplified example of one HNL mixing with one SM neutrino has a Lagrangian given by

$$\mathcal{L} \supset m_D \overline{\nu}_L \nu_R + \frac{1}{2} M_R \nu_R^T C \nu_R + \text{h.c.}\,, \tag{4.2.37}$$

where m_D and M_R are the Dirac and Majorana masses respectively with $M_R \gg m_D$. From the Lagrangian the mass matrix is constructed,

$$\mathcal{M} = \begin{pmatrix} 0 & m_D \\ m_D^T & M_R \end{pmatrix}, \tag{4.2.38}$$

which has eigenvalues,

$$m_\pm = \frac{M_R \pm \sqrt{M_R^2 + 4m_D^2}}{2}\,. \tag{4.2.39}$$

For $M_R \gg m_D$, at leading order in M_R, the eigenvalues are

$$m_\pm = \frac{M_R}{2}\left(1 \pm \sqrt{1 + 4\frac{m_D^2}{M_R^2}}\right) \approx \frac{M_R}{2}\left(1 \pm \left[1 + 2\frac{m_D^2}{M_R^2}\right]\right) = \begin{cases} M_R + \mathcal{O}(M_R^{-1}) \\ -\frac{m_D^2}{M_R} \end{cases}, \tag{4.2.40}$$

where one of the mass eigenstates will have the same mass as the new HNL, whereas the other will have a small mass due to the scaling between the Dirac and Majorana masses. Hence, the introduction of a massive HNL has introduced the very small mass of the SM neutrino giving the name "seesaw" to this mechanism [65].

The mass matrix $\mathcal{M}$ can be diagonalised using,

$$\mathcal{M} = O\, m\, O^T \quad \text{for} \quad O = \begin{pmatrix} \cos\theta & \sin\theta \\ -\sin\theta & \cos\theta \end{pmatrix} \quad \text{and} \quad m = \begin{pmatrix} m_- & 0 \\ 0 & m_+ \end{pmatrix}, \tag{4.2.41}$$

from which one finds the mixing angle using the small angle approximation,

$$\tan(2\,\theta) = 2\,\frac{m_D}{M_R} \quad \Rightarrow \quad \theta \approx \frac{m_D}{M_R}\,. \tag{4.2.42}$$

In this approximation, the diagonalising matrix O is given by

$$O = \begin{pmatrix} \cos\theta & \sin\theta \\ -\sin\theta & \cos\theta \end{pmatrix} \approx \begin{pmatrix} 1 & \frac{m_D}{M_R} \\ -\frac{m_D}{M_R} & 1 \end{pmatrix} . \tag{4.2.43}$$

The mass eigenstates $v_\pm$ are found using

$$\begin{pmatrix} \nu_- \\ \nu_+ \end{pmatrix} = O^T \begin{pmatrix} \nu_L \\ \nu_R \end{pmatrix} = \begin{pmatrix} \cos\theta\nu_L - \sin\theta\nu_R \\ \sin\theta\nu_L + \cos\theta\nu_R \end{pmatrix} \approx \begin{pmatrix} \nu_L - \theta\,\nu_R \\ \theta\,\nu_L + \nu_R \end{pmatrix} , \tag{4.2.44}$$

and hence they are a linear combination of the initial fields [66].

General Mixing

Moving on from the simplified example, the general Lagrangian for $\mathcal{N}$ heavy neutral leptons is given by

$$\mathcal{L} \supset i\overline{N}_I \not{\partial} N_I - F_{\alpha I}\overline{L}_\alpha \cdot \tilde{\phi}\, N_I + \text{h.c.}\,, \tag{4.2.45}$$

where $F_{\alpha I}$ is a matrix of Yukawa couplings between the left-handed SM lepton doublet (L_α) and the right-handed singlet containing the HNLs (N_I) for $\alpha \in \{e, \mu, \tau\}$ and $I \in [1, \mathcal{N}]$. $\tilde{\phi} = i\sigma_2\phi^*$ is defined for the Higgs doublet ϕ and the second Pauli matrix σ_2 [67].

Through EWSB, the Higgs field is replaced by its vev, v_H, and kinetic mixing between the SM neutrinos and the new HNLs occurs through

$$\tilde{\phi} = \frac{1}{\sqrt{2}} \begin{pmatrix} v_H \\ 0 \end{pmatrix} \qquad \Rightarrow \qquad \overline{L}_\alpha \cdot \tilde{\phi} N_I = \frac{v_H}{\sqrt{2}} \overline{\nu}_\alpha N_I\,. \tag{4.2.46}$$

Together with the left-handed SM neutrinos (v_α), the right-handed neutrinos N_I form Dirac spinors and can construct Dirac mass terms,

$$\mathcal{L}_{\text{dirac}} \propto \overline{\nu} m_D \nu = \overline{\nu}_L m_D \nu_R + \text{h.c.} \tag{4.2.47}$$

The HNLs can be Majorana particles with mass terms given by

$$\mathcal{L}_{\text{Majorana}} \propto M_R \overline{N_R}^C N_R + \text{h.c.} \tag{4.2.48}$$

for the mass matrix M_R [67]. Altogether, the mass terms are

$$\begin{aligned}\mathcal{L} \supset -\frac{1}{2}\Bigg(&\left[(\overline{\nu}_\alpha)_L\ (m_D)_{\alpha I}\ (N_I)_R + \left(\overline{N}_I^C\right)_L\ (m_D)_{I\alpha}\ \left(\nu_\alpha^C\right)_R\right] \\ &+ \sum_{I_1,I_2=1}^{\mathcal{N}} \left(\overline{N}_{I_1}^C\right)_L (M_R)_{I_1 I_2} \left(N_{I_2}\right)_R\Bigg) + \text{h.c.} \\ = -\frac{1}{2}&\left(\overline{\nu}_L\ \overline{N}_L^C\right)\ \mathcal{M}\begin{pmatrix}\nu_R^C \\ N_R\end{pmatrix} + \text{h.c.}\end{aligned} \tag{4.2.49}$$

Here the number of SM flavours and new HNLs are summed over [68], and the mass matrix is given by

$$\mathcal{M} = \begin{pmatrix} 0_{(3\times3)} & m_{D\,(3\times\mathcal{N})} \\ m_{D\,(\mathcal{N}\times3)}^T & M_{R\,(\mathcal{N}\times\mathcal{N})}\end{pmatrix} \tag{4.2.50}$$

for Majorana M_R and Dirac $(m_D)_{\alpha I} = \frac{1}{\sqrt{2}} v_H\, F_{\alpha I}$ mass matrices [67]. The Lagrangian in eq. (4.2.45) contains the flavour eigenstates of the neutrinos, which are different to the mass eigenstates obtained through diagonalising the mass matrix,

$$V^T \mathcal{M} V = m = \begin{pmatrix} m_{L\,(3\times3)} & 0_{(3\times\mathcal{N})} \\ 0_{(\mathcal{N}\times3)} & M_{(\mathcal{N}\times\mathcal{N})}\end{pmatrix}. \tag{4.2.51}$$

Here m is a block-diagonal for unitary matrix, and matrix V has a form given by

$$V = \begin{pmatrix} \mathbb{1}_{(3\times3)} & a^\dagger_{(3\times\mathcal{N})} \\ -a_{(\mathcal{N}\times3)} & \mathbb{1}_{(\mathcal{N}\times\mathcal{N})}\end{pmatrix}. \tag{4.2.52}$$

Choosing $a = M_R^{-1} m_D^T$, the diagonal matrix is obtained [66],

$$m = V^T \mathcal{M} V \approx \begin{pmatrix} -m_D M_R^{-1} m_D^T & \mathcal{O}(M_R^{-2}) \\ \mathcal{O}(M_R^{-2}) & M_R + \mathcal{O}(M_R^{-1})\end{pmatrix}. \tag{4.2.53}$$

The light left-handed neutrino masses become $m_L = -m_D M_R^{-1} m_D^T$ whereas the right-handed neutrino mass is at leading order unchanged. The mass eigenstate Lagrangian is given by

$$\mathcal{L} \supset -\frac{1}{2}\overline{\nu_L} m_L (\nu_L)^c - \frac{1}{2}\overline{\nu_R}^c M_R \nu_R + \text{h.c.} \tag{4.2.54}$$

In addition to the mixing between the new HNL(s) and the SM neutrinos, the

presence of mixing between the SM neutrino states needs to be taken into account through the inclusion of the PMNS matrix as seen in section 2.5,

$$\begin{pmatrix} \nu_{L\alpha} \\ N^C_{RI} \end{pmatrix} = \begin{pmatrix} U_{\text{PMNS}\,(3\times3)} & a^\dagger_{(3\times\mathcal{N})} \\ -a_{(\mathcal{N}\times3)} & \mathbb{1}_{(\mathcal{N}\times\mathcal{N})} \end{pmatrix} \begin{pmatrix} \nu_m \\ N^C_{m'} \end{pmatrix} , \tag{4.2.55}$$

for $\alpha, m \in \{1,2,3\}$ and $I, m' \in [1,\mathcal{N}]$. Hence, the neutrino mass eigenstates are

$$\nu_L = \sum_{m=1}^{3} (U_{\text{PMNS}})_{lm} \nu_m + \sum_{m'=1}^{\mathcal{N}} a^\dagger_{lm'} N^C_{m'} , \tag{4.2.56}$$

given the flavour eigenstates v_m and $N_{m'}$. It can be assumed that only one HNL is relevant, either through being the only new particle in the theory, or as the others have significantly higher masses which are kinematically out of reach [67]. Simplifying to one HNL, the Lagrangian with interactions to the Higgs, W, and Z-bosons is

$$\begin{aligned} \mathcal{L} \supset & -\frac{g}{\sqrt{2}} W^+_\mu \sum_{l=e}^{\tau} \left(\sum_{m=1}^{3} \overline{\nu_n} (U_{\text{PMNS}})^*_{lm} \gamma^\mu P_L l^- + \overline{N^c} a^*_l \gamma^\mu P_L l^- \right) \\ & - \frac{g}{2\cos\theta_W} Z_\mu \sum_{l=e}^{\tau} \left(\sum_{m=1}^{3} \overline{\nu_n} (U_{\text{PMNS}})^*_{lm} \gamma^\mu P_L \nu_L + \overline{N^C} a^*_l \gamma^\mu P_L \nu_L \right) \\ & - \frac{g m_N}{2 M_W} h \sum_{l=e}^{\tau} \overline{N^C} a^*_l P_L \nu_L + \text{h.c.} , \end{aligned} \tag{4.2.57}$$

where it can be seen that the HNL interactions with $W^\pm, Z^0$, and h are the neutrino interactions modified by the mixing angle a_l [69]. $P_L = \frac{1}{2}\left(1-\gamma^5\right)$ are the left-handed projection operator defined in section 2.2. For one HNL, there are three angles $a_\alpha = \frac{v_H}{\sqrt{2}} \frac{F_\alpha}{M_R}$, which in literature are usually refereed to as U_α. One often assumes either *electron-*, *muon-*, or *tau-dominance* for $|U_\alpha|$ much bigger than the other two [67]. For the remainder of this thesis, the common practice in literature will be adopted, and U_α will be used for HNL mixing with SM neutrinos.

Heavy Neutral Lepton Decays

The HNLs considered in this thesis have masses $m_{\text{HNL}} \ll m_{W^\pm, Z^0}$, and hence the $W^\pm$ and Z^0 bosons will be integrated out when considering the decays of the HNLs,

much like Fermi's EFT for weak interactions [70].

Through a Z^0-mediator, the HNL can have *neutrino-only* decays into three neutrinos, which is a purely invisible final state.

The decays of HNLs into fermionic final states can be categorised by their heavy, integrated out mediator; *charged* and *neutral*. For decays mediated by $W^{\pm}$, the charged current, the HNL decays into two leptons and a neutrino ($N \to l_\alpha^- v_\beta l_\beta^+$ for $\alpha \neq \beta$) or two quarks (one up-type u and one down-type d) and a lepton ($N \to l_\alpha u_i \overline{d}_j$), where the outgoing fermions have different flavours. For decays mediated by Z^0, the neutral current, the HNL decays into two fermions and a neutrino ($N \to v_\alpha f \overline{f}$), where the flavour of the lepton pair ($l_\beta \overline{l}_\beta$) can either match $\alpha = \beta$ or be different $\alpha \neq \beta$ to the neutrino flavour.

For HNLs with masses below 1 GeV, when quark pairs are produced they form bound states, mesons, as their momenta are too small to escape the attraction from QCD between them. See section 2.2.3 for further detail. Both charged h^+ and neutral h^0, pseudo-scalar h_P and vector h_V mesons can be produced from charged and neutral mediated decays of HNLs; $N \to l_\alpha h^+_{P,V}$ and $N \to v_\alpha h^0_{P,V}$. See Figure 4.4 for depictions of HNL decays into mesons, the integrated out mediators have been included in the depictions for visualisation of the current for each type of decay.

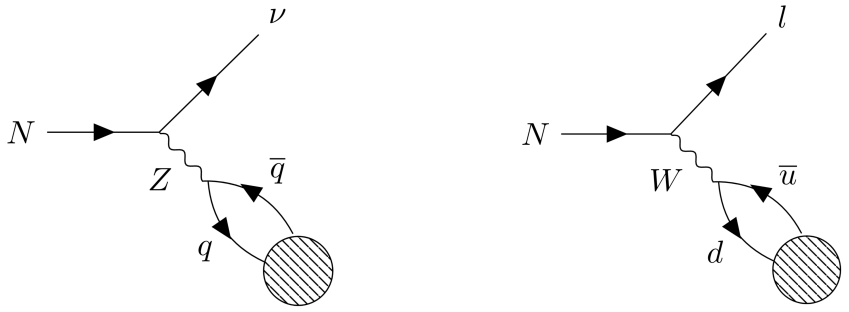

Figure 4.4: HNL decay into a neutrino and neutral meson (left), and lepton and a charged meson (right).

For $m_{\text{HNL}} > 1$ GeV, the produced quarks have enough momenta to be free, but they later shower and hadronise forming multi-hadron final states. These can be described using the underlying quark interactions, where the subsequent hadronisation is an

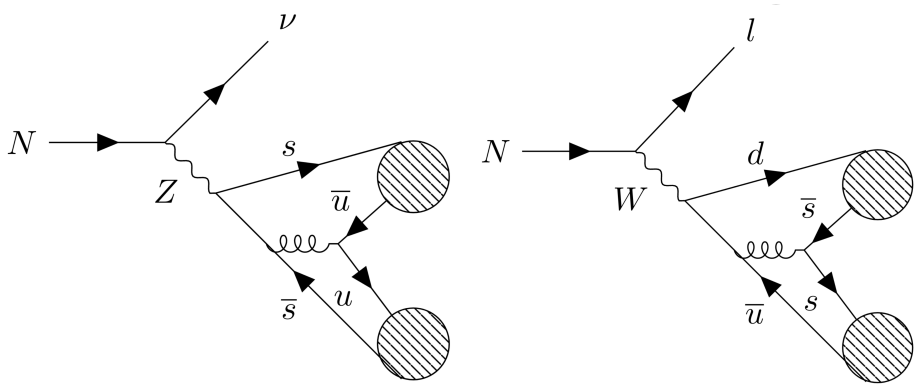

Figure 4.5: HNL decay into a neutrino (left), or a lepton (right) and two kaons.

additional correction [71]. Figure 4.5 displays two possibilities for decays into multi-meson through neutral (left) and charged (right) currents for production of two kaons, K^-K^+ and K^0K^- respectively [70]. The decay width formulas for the channels described can be found in Appendix B.

Figure 4.6 displays the branching ratio for six groupings of HNL decay channels; invisible, v+multi-hadrons (hadr.), $l^{\pm}$+multi-hadrons (hadr.), v+single meson (mes.), $l^{\pm}$+single meson (mes.), and purely leptonic $vl\bar{l}$. Here the invisible final state contains the 3-neutrino decay mode, but this category can be modified to also contain decays into a dark sector, which the HNL is a portal to. It can be seen that the single

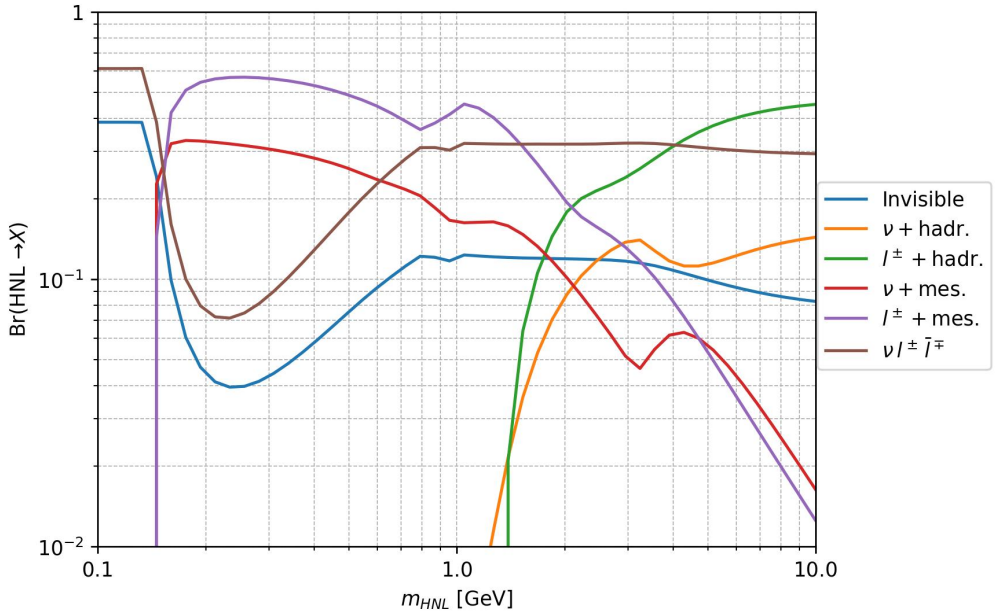

Figure 4.6: HNL branching ratios for $|U_e| = 1$ and $|U_{\mu,\tau}| = 0$.

meson final states dominate for $m_{\text{HNL}} < 1$ GeV compared to multi-hadrons final states, but the latter starts to dominate for $m_{\text{HNL}} > 2$ GeV. The three-neutrino and the purely leptonic final state branching ratios can be seen to be somewhat stable for $m_{\text{HNL}} \in [1, 10]$ GeV. The sudden kinks and changes in branching ratio happen when new decay channels become available.

For the decay widths described in this section, Figure 4.7 displays the characteristic decay length $c\tau$ (without boost and therefore process independent) as a function of the HNL mass and the mixing parameter U_e. The HNL is assumed to only mix with SM electron neutrinos, electron-dominance ($U_e \gg U_{\mu,\tau}$). The red line represents the radius of the ATLAS detector at 12.5 m. Without boost, it can here be seen that the HNL must have a significantly small coupling to escape ATLAS if its mass is 10 GeV or above, therefore reducing the sensitivity drastically. As the momentum of the particle increases the radius of ATLAS becomes contracted for the decaying particle, and therefore for sufficiently high boosts it is possible for a 10 GeV particle to leave

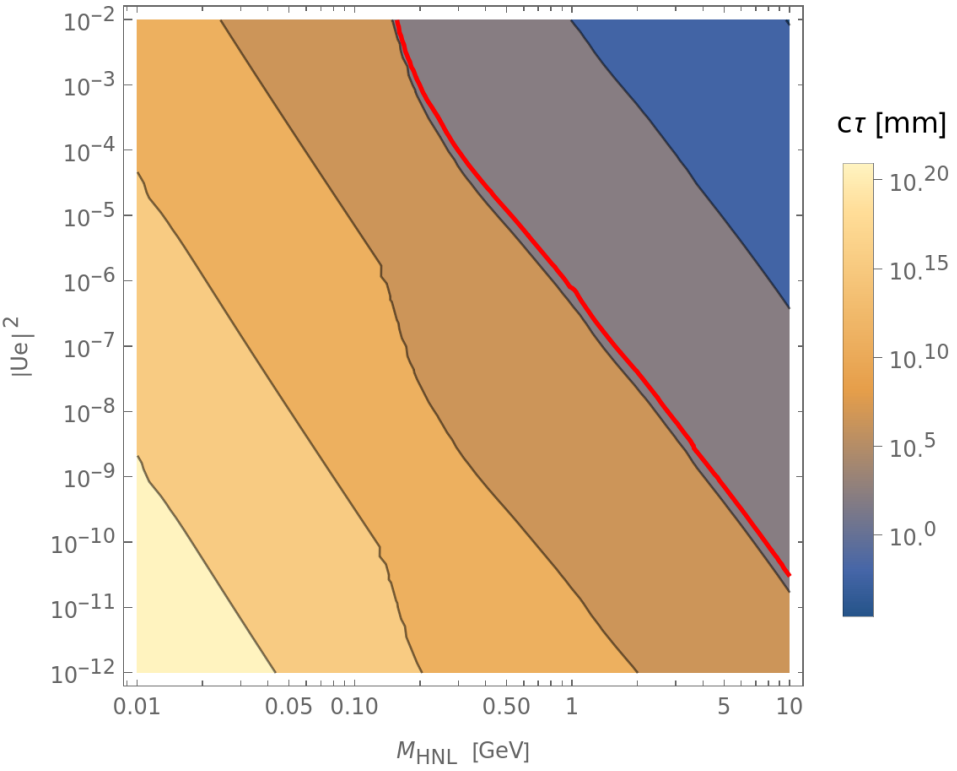

Figure 4.7: Decay length, without boost $c\tau$, for HNLs with the radius of the ATLAS detector highlighted in red.

without decaying. The boost is given by $\frac{p}{m_{\text{HNL}}}$, hence for mass $m_{\text{HNL}} = 10$ GeV and momentum $p = 100$ GeV the sensitivity to $|U_e|^2$ is increased by a factor of 10.

4.3 Dark Matter Searches

Having introduced several models for dark matter, the searches for dark matter will be described now, expanding on the New Physics searches outlined in section 3.5. In order to determine the nature of dark matter, many experiments and searches have been preformed and are planned to take place in the future. These generally fall into three categories; collider searches, indirect detection, and direct detection. As seen in Figure 4.8, each rely on the dark matter exhibiting different interactions with the particles in the SM.

Direct detection searches depend on dark matter particles scattering off SM particles and on the ability to measure the recoil energy of target particles, such as nuclei. If the DM particles annihilate into SM particles, one can detect these SM particles as an indirect method of detecting the DM particles. An example of this method is measuring excesses of cosmic rays or neutrinos. Both of these methods of direction have a lower limit on their reach with respect to the masses of dark matter. Direct detection have a minimum recoil energy threshold due to detector limitations, whereas the indirect detection signals will be obscured by background for small masses.

The third method has SM particle interactions producing DM particles, which is the foundation for particle collider searches for dark matter. The previous two searches

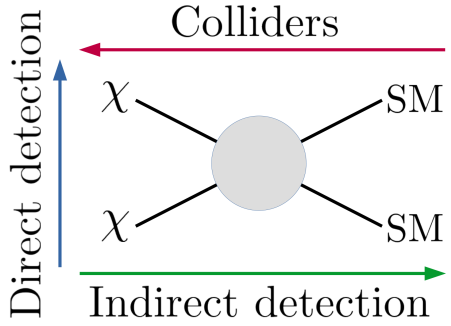

Figure 4.8: Detection methods of dark matter χ (from [5]).

have the dark matter particles already existing, whereas collider searches rely on the production of dark matter. But collider searches have a large reach, being able to detect both light and heavy dark matter. The detection methods presented are not exclusive and can be used together in order to pinpoint the nature of DM [72].

When searing for dark matter at particle colliders, many considerations have to be taken into account, a few of these will be described here. The type of collider considered determines the productions modes present, for example a lepton collider excludes the possibility of production modes like gluon-fusion ($gg \to X$). The DM particle(s) interactions also affects the production modes. For example at leading order, the dark photon does not interact with gluons, and hence even at hadron colliders gluon-fusion is not available. The centre-of-mass energy of the collider puts an upper bound on the mass of the DM particle(s), which can be produced, and determines the probability of the production and decay modes of the DM.

As described in section 3.5, there are three main types of collider searches; *missing energy*, *prompt*, and *displaced*. Missing energy searches, as the name suggests, consists of looking for missing energy in the events. An example is a dark matter model with a particle acting as a portal, both interacting with the SM and a dark sector but with much larger couplings to the dark sector. In this case, every time the portal particle is produced it will decay into the dark sector, which is undetectable, and show up as missing energy in the collider.

The decay length of a particle is determined by its lifetime, which in turn depends on its interactions. The decay length is inversely proportional to both the coupling strength and the particle's mass. Therefore, if the DM particle is very heavy or interacts strongly with the SM, it will decay promptly. For combinations of coupling strength and mass, the particle travels a distinguishable length away from the IP and the vertex becomes displaced.

Further, if the DM particle is long-lived enough, it will travel through the detector and decay outside it, appearing as missing energy. Detectors are built around the IP and therefore have a sensitivity to dark matter with a lower bound on the

coupling and mass. Recently, many proposals are trying to address this problem, detectors specialising in *long-lived particles* (LLPs) like SHiP [67], MATHUSLA [73], FASER [74], CODEX-b [75], and many others. These detectors are also known as *far* detectors due to their location far away from the interaction point. They are usually extensions to already existing particle collider experiments but differ in their design, relation to the experiment it is connected to, and sensitivity. An example of an LLP experiment is the ANUBIS detector which will be described in further detail in chapter 5.

4.3.1 Exclusion Limits & Sensitivity Projections

Having presented several models describing dark matter together with the searches used to look for dark matter in colliders, there are two possible options for results: the experimental results match the theoretical predictions, or they differ. For each result, a different statistical approach is used to ensure that the correct conclusion is drawn. If the result deviates from the expected, it has to be determined whether the deviation is statistically significant, or can be explained as a statistical fluctuation. Oppositely, if the result is as expected, limits can be set on any model which would cause deviations that are statistically significant. Most results currently agree with the SM predictions, and hence regions of parameter space have been excluded, which will be seen in the plots presented in the following section [2].

In general, given a certain model one can calculate the expected cross-section for each production mode which, together with the integrated luminosity of the experiment, provides an expected number of events ($N = \sigma_{\text{NP}} \times \mathcal{L}_{\text{int}}$). Using this, depending on the expected number of background events, one can calculate the sensitivity of the collider to the production mode.

In order to determine the statistical significance of a result (or lack thereof), the *confidence interval* (CoI) is defined within which the true value of a parameter will lie a certain percentage of the time, given by the *confidence level* (CL) [28]. A

commonly used confidence level is 95%. This means that if a measured parameter is within the corresponding CoI, then there is a 5% chance that the result has been accepted incorrectly.

To calculate the confidence level, the probability density function $f(y)$ is defined,

$$P\left(y \in [y, y+dy]\right) = f(y)\, dy\,, \tag{4.3.1}$$

which is the probability of an observable y being in the interval $[y, y+dy]$. Whereas the *cumulative distribution function* (CDF) for variable Y,

$$F(y) = P(Y \leq y)\,, \tag{4.3.2}$$

describes the probability of achieving a result less than or equal to y. Continuous CDFs can be written as

$$F(y) = \int_{-\infty}^{y} f(t)\, dt\,, \tag{4.3.3}$$

for probability density function $f(t)$.

For a specific confidence level, α_{crit}, the critical value x_{crit} is defined for when the CDF has value $F(x_{\text{crit}}) = \alpha_{\text{crit}}$, such that $x_{\text{crit}} = F^{-1}(\alpha_{\text{crit}})$ for the inverse of the cumulative function [28].

The statistical test used later in section 6.6 will now be described. The *Poisson* distribution for observing k events when expecting λ number of events is given by

$$P(k, \lambda) = \frac{\lambda^k e^{-\lambda}}{k!}\,. \tag{4.3.4}$$

The discrete cumulative Poisson distribution is found by summing from 0 to k events,

$$F(k, \lambda) = P(K \leq k, \lambda) = \sum_{x=0}^{\lfloor k \rfloor} \frac{\lambda^x e^{-\lambda}}{x!} = \frac{\Gamma(\lfloor k+1 \rfloor, \lambda)}{\Gamma(\lfloor k+1 \rfloor)}\,, \tag{4.3.5}$$

for the *upper incomplete gamma* function,

$$\Gamma(k, \lambda) = \int_{\lambda}^{\infty} t^{k-1} e^{-t} dt\,, \tag{4.3.6}$$

and the *gamma* function,

$$\Gamma(k,0) = \Gamma(k) = \int_0^\infty t^{k-1} e^{-t} dt \,. \tag{4.3.7}$$

For positive number of expected events ($\lambda > 0$) and $k > 0$, the *regularized* upper incomplete gamma function is constructed,

$$Q(\lfloor k \rfloor, \lambda) = \frac{\Gamma(\lfloor k \rfloor, \lambda)}{\Gamma(\lfloor k \rfloor)} = \frac{1}{\Gamma(\lfloor k \rfloor)} \int_\lambda^\infty t^{\lfloor k-1 \rfloor} e^{-t} dt = \sum_{x=0}^{\lfloor k-1 \rfloor} \frac{\lambda^x e^{-\lambda}}{x!} \,. \tag{4.3.8}$$

Here the relationship between the sum of Poisson probabilities is given in terms of incomplete gamma integrals (see proof in Appendix. C) [76].

The probability for observing both μ_S signal events from New Physics and μ_B SM background events,

$$\alpha_{\mu_S+\mu_B} = P_{\mu_S+\mu_B} \left(X \leq X_{\text{obs}} \right) \,, \tag{4.3.9}$$

is given by the probability of the results of a statistical test X being less than or equal to the observed value X_{obs}. For example, using the Poisson distribution described above, the probability of observing less than or equal to μ_B events when expecting $\mu_B + \mu_S$ events is given by

$$\alpha = \frac{\Gamma(\lfloor \mu_B + 1 \rfloor, \mu_B + \mu_S)}{\Gamma(\lfloor \mu_B + 1 \rfloor)} = Q(\lfloor \mu_B + 1 \rfloor, \mu_B + \mu_S) \,, \tag{4.3.10}$$

which can rearranged to get an expression for μ_S,

$$\mu_S = Q^{-1} \left(\lfloor \mu_B + 1 \rfloor, \alpha \right) - \mu_B \,, \tag{4.3.11}$$

where $Q(a, z)$ is the regularised incomplete gamma function. For the critical value α_{crit}, the critical number of signal events, $(\mu_S)_{\text{crit}}$, needed for $\mu_B + \mu_S$ to be statistically different from μ_B is found. Hence, the confidence level ($\text{CL}_{\mu_S+\mu_B} = 1 - \alpha_{\mu_S+\mu_B}$) is used to calculate exclusion limits and sensitivity projections [77].

4.4 Current Limits & Projections

Having presented the procedures for searching for dark matter in collider experiments and how these are used to find exclusion limits and projections, the current and projected results for the three dark matter models described previously will be presented.

Dark Photon

Figure 4.9 displays the current exclusion limits on the mixing parameter ϵ as a function of the dark photon mass $m_{A'}$ for various past, current, and future experiments. The grey regions have already been excluded by past experiments, whereas the coloured regions are projections from currently running experiments. The dashed

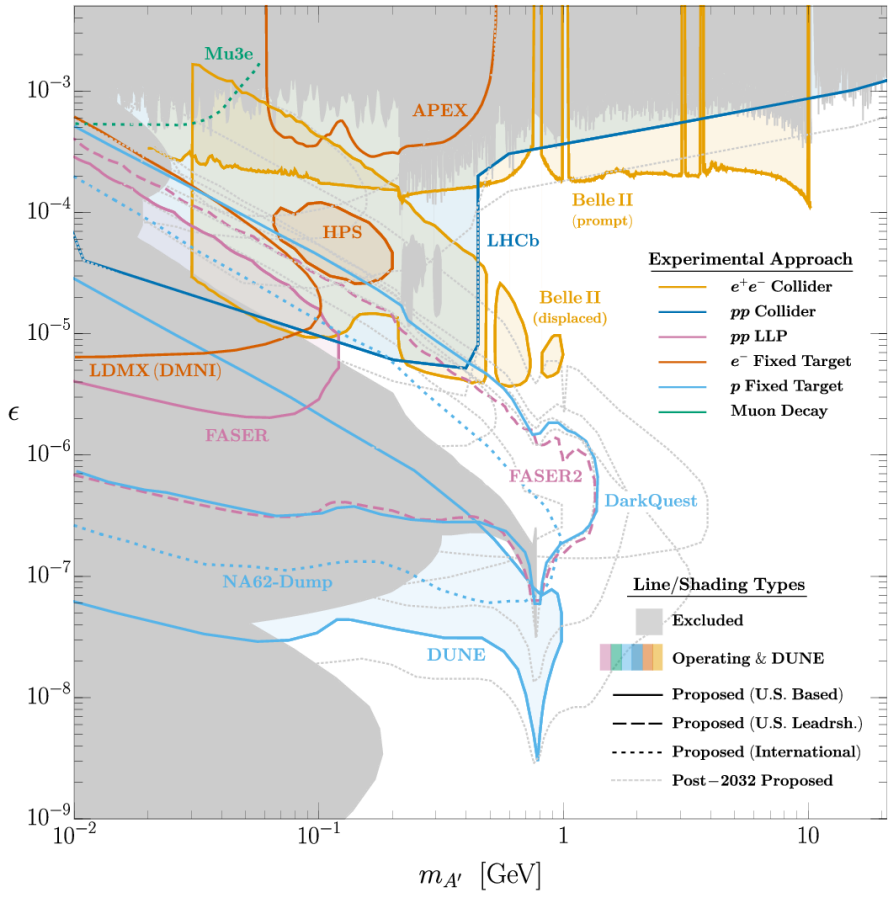

Figure 4.9: Current limits and projections on a minimal dark photon with mass $m_{A'}$ and kinetic mixing ϵ (from [78]).

lines are projections for experiments proposed to start operations before 2032, while the dotted grey lines are proposed for after 2032. Experiments bounded from both above and below, like "FASER(2)" in light pink or "Belle II (displaced)" in orange, are looking for long-lived particles with displaced vertices. Hence, a sufficiently large decay length is needed in order to distinguish the decay from being prompt, but the searches are limited by both sensitivity and finite detector volume for longer decay lengths. It can be seen that the sensitivity drastically drops for masses above 1 GeV, where the current best limits are found at Belle II for prompt searches. This region of parameter space requires detectors located at key distances from the IP in order to acquire the correct mass-coupling correlation to detect displaced vertices.

Axion-Like Particles

Figure 4.10 displays the Current limits and projections on the ALP coupling to photons ($|g_{a\gamma\gamma}| = |\frac{4}{f_a}c_\gamma|$) as a function of the ALP mass m_a. Coloured regions and solid lines are experimentally excluded, whereas dashed and dotted lines are projections. The grey regions are mainly from astrophysical data such as restrictions from *big bang nucleosynthesis* (BBN) [5]. BBN is when the production of lighter

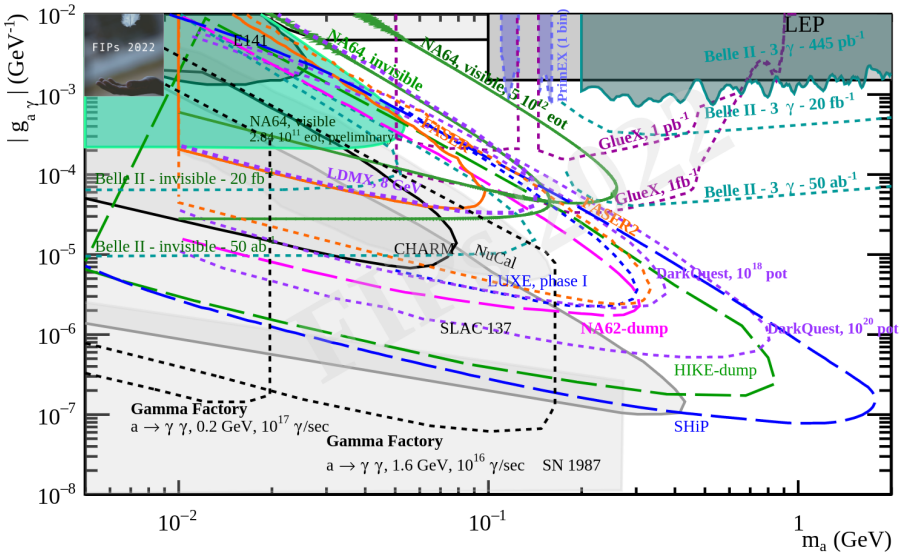

Figure 4.10: Current limits and projections on ALPs with coupling to photons, see text for detail (from [54]).

nuclei began, which can be significantly disrupted by the injection of particles from decay of DM particles, where the sequence of processes in BBN and their ratios are altered [79]. The exclusion limit from BBN is also applicable for HNLs, see figure 4.11, and have been produced for dark photons [80]. Similarly to the limits on the dark photon coupling, one can distinctly differentiate between the displaced vertex and prompt searches, see "Belle II-3 γ" in cyan compared to the blue "SHiP" results. It is worth noting that for these limits and projections, one assumes that all other ALP couplings are negligible, varying only one coupling and the ALP mass. For exclusion limits on the ALP-fermion and ALP-gluon couplings see Appendix D.

Heavy Neutral Leptons

Figure 4.11 displays the current limits and projections on the HNL mixing with electron neutrinos ($|U_e|^2$), where the coupling to muon and tau neutrinos are assumed negligible. For muon- and tau-dominance see Appendix D. The colour-coding is the same as the ALP limits described previously in Figure 4.10. It can again be seen that there remains a large area of unexplored parameter space above 5 GeV. The dashed line for "seesaw" has $|U_\alpha|^2 = \sqrt{\Delta m^2_{\text{atm}}}/m_{\text{HNL}}$ and is found from the "naive seesaw type I prediction" [54]. Here Δm_{atm} is the difference in mass between the two lightest mass eigenstates of atmospheric neutrinos [81], which are produced in interactions between the Earth's atmosphere and incoming cosmic rays [2].

4.5 Conclusion

Here, a range of models and production mechanisms for dark matter were introduced, with a focus on portals. In particular, the models of dark photons, axion-like particles, and heavy neutral leptons are presented, together with their current exclusion limits and projections. These show areas of parameter space yet to be explored, combinations of coupling parameters and masses which current detector designs cannot reach.

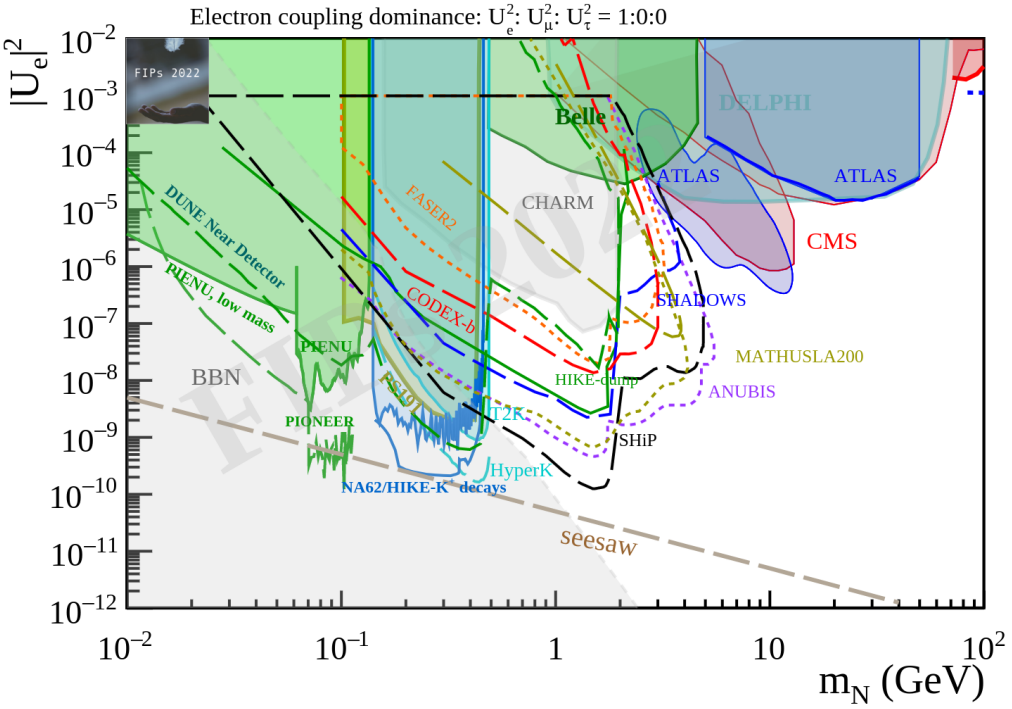

Figure 4.11: Current limits and projections on minimal HNL models for electron-dominated mixing (from [54]).

Extending the New Physics searches at colliders from the previous chapter, the specifics of dark matter searches in colliders were discussed. Given the lack of New Physics observed in experiments thus far, a statistical method for creating exclusion limits and sensitivity projects were demonstrated.

When producing these limits and projections, many assumptions are made. If the dark matter model contains more than one variable, one has to either keep all but one static using pre-set values, or perform scans varying more than one parameter. The use of simplified models, such as portals, addresses this, but in chapter 6 an alternative method to reduce the number of parameters is presented.

The particle detectors, Belle II and ATLAS described in sections 3.3 and 3.4, were not build with the discovery of dark matter in mind. They mainly focus on prompt decays at the interaction point, though have over the years increasingly improved the searches for displaced vertices. But the detectors at colliders have finite radius, and thus a long-lived particle can escape the detector undetected. In the next chapter, this issue will be addressed.

Chapter 5

ANUBIS Sensitivity Studies

5.1 Introduction

The finite dimensions of detectors at particle colliders limits their reach for long-lived particles with small coupling constants and light masses. In this chapter, a solution to extending the reach of the ATLAS detector, described in section 3.4, is presented. *AN Underground Belayed In-Shaft search experiment* (ANUBIS) aims to detect particles decaying outside the limitations of ATLAS but still inside the surrounding cavern.

Searches at ATLAS have a limited sensitivity to LLPs, as seen on the exclusion plots presented in section 4.4. Due to the light masses of the LLPs, the remaining center-of-mass energy results in large amounts of noise from pile-ups in each event. Figure 4.11 displays the ATLAS searches for an electron-dominated HNL, where the prompt decays start at around 10 GeV and displaced vertex searches around 2 GeV. The reach for the latter is complementary to the LLP detectors (such as MATHUSLA200 [73] and SHiP [67]), though the sensitivity is significantly reduced. The LLP detectors have shielding from both the materials, such as air or earth, between the detector and the interaction point, and from the main detector they are associated with. Hence, noise is stopped before reaching the detector, resulting in much cleaner signals and therefore increased sensitivities.

The rest of this chapter is organised as follows. Section 5.2 describes the ANUBIS detector layout and implementation, and section 5.3 briefly presents previous studies of the detector. The ongoing development of the software for the sensitivity studies by the ANUBIS collaboration is described in section 5.4. Finally, the current ANUBIS studies and the future of these are discussed in sections 5.5 and 5.6, where the models for the long-lived particles considered are outlined.

5.2 The ANUBIS Detector

The ANUBIS experiment was originally proposed to be located in the service shaft above ATLAS, left panel of Figure 5.1, where four tracking stations are located vertically in the shaft [82]. Subsequently, it was proposed to install components along the ceiling of the cavern (right panel of Figure 5.1), or a combination of the shaft and ceiling configurations. Figure 5.1 displays the ATLAS detector (mostly in blue) and its surrounding underground cavern, together with the LHC beampipe on the left panel. The two ANUBIS configurations can be seen in red (left) and orange (right). The ceiling configuration includes two disks at the entrance to each of the two service shafts, which can be removed for inspections and down-time of the experiment [83].

The reason for the change in detector configuration was mainly due to concerns of

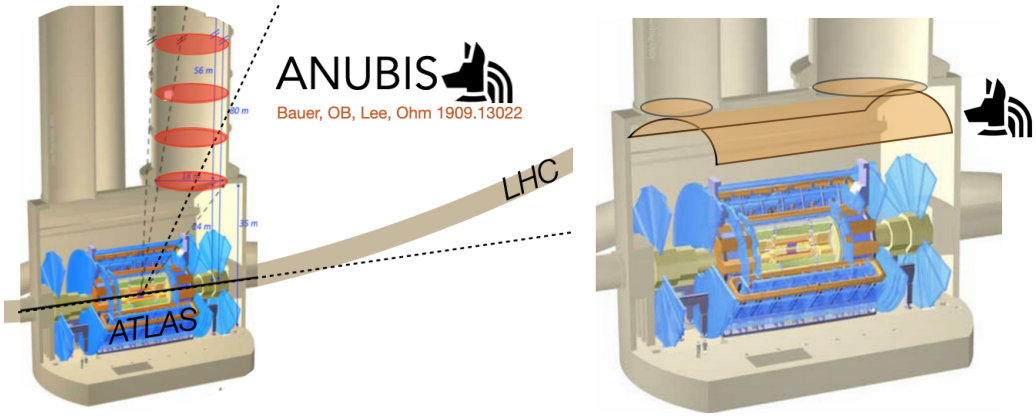

Figure 5.1: ANUBIS configurations for (left) the service shaft (from [83]), and (right) ceiling (from [84]).

background events. For example, when particles hit the wall material at the entrance to the shaft, they create showers of particles which will interfere with the detection of signals at ANUBIS. Additionally, the new ceiling configuration presents improved sensitivity and acceptance in comparison to the shaft configuration. This is due to the larger solid angle coverage as the ceiling tracking stations are closer to the interaction point of ATLAS compared to the shaft ones [48].

Currently, a prototype, *proANUBIS*, has been installed in the ATLAS cavern and is taking data in order to estimate the backgrounds, verifying the detector design and its operation during data-taking. The detector consists of layers of tracking stations, see Figure 5.2 where the design of proANUBIS is depicted [85]. Each tracking station consist of Resistive Plate Chambers (RPCs), which are parallel plates separated by a narrow gap filled with gas. An electric field is applied across the plates, and therefore when charged particles pass through they ionise the gas which subsequently release electrons [28]. As the RPCs rely on the incoming particle being charged, ANUBIS is currently unable to detect neutral particles. The RPCs are currently installed in the muon spectrometers in ATLAS, their production is thus already undergoing and the production of the RPCs needed for ANUBIS is easy [82].

The inclusion of several layers allows for better particle detection and vertex reconstruction, as seen in Figure 3.7. The prototype tracking stations have an area of

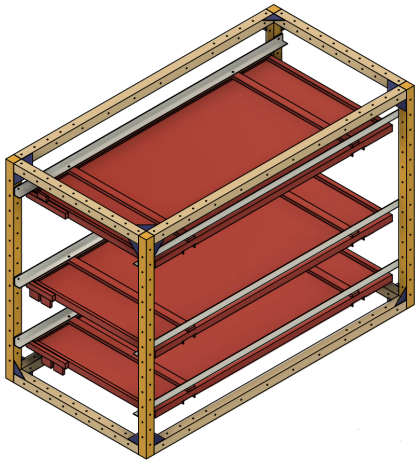

Figure 5.2: Design of the proANUBIS detector consisting of three layers of tracking stations seen in red.

$1\,\mathrm{m} \times 1.8\,\mathrm{m}$ separated by approximately 0.5 m. Each tracking station will consist of up to three layers of tracking material, which allows for better trajectory reconstruction. The bottom tracking station of proANUBIS has three layers whereas the middle has one, and the top has two [85]. For further detail of the detector design see [48, 82, 85].

The full ANUBIS detector is located approximately 20m from the ATLAS interaction point and is therefore sensitive to LLPs with lifetimes $10^{-1}\,\mathrm{m} < c\tau < 10^{6}\,\mathrm{m}$ [85], extending the reach of ATLAS beyond the 7.5m limitation described in section 3.4. ANUBIS proposes a low-cost extension to the ATLAS detector making use of existing infrastructure such as the service shaft and ceiling, as well as existing technology for its tracking detectors. The proximity to ATLAS provides ANUBIS with a large angular coverage and therefore a large detection volume, together with the possibility of integrating ANUBIS with the ATLAS trigger system; signals at ANUBIS will be able to be timed with the signals observed in ATLAS. This will provide an active-veto system and can isolate events of interest, allowing ATLAS to keep events that otherwise would have been thrown out [85].

5.3 Previous ANUBIS Studies

In the following section, some previous sensitivity studies done for the ANUBIS detector are outlined. First, a study of a dark scalar model is described followed by a study of heavy neutral leptons. For other studies of HNLs at ANUBIS see [86–89], and [90] studies the lightest neutralino which is found in SUSY. Another study of note is [91] that introduces inelastic dark matter, a pair of particles with almost degenerate masses, which couple to the SM with a dark photon portal.

5.3.1 Dark Scalar

The initial proposal of ANUBIS [82] presented the study of a dark scalar, as described in Appendix A, produced in Higgs decay, $h \to SS$. The projections were produced for the service shaft configuration. These results were updated in the unpublished Master's thesis [48] for both the shaft and ceiling configurations. The Higgs is considered to be produced in gluon fusion (ggF) and vector boson fusion (vbf), and then decays into a pair of dark scalar particles, which are assumed to decay into $b\bar{b}$-pairs. These subsequently hadronise, forming charged jets detected by ANUBIS.

The number of LLPs produced,

$$N_{\text{LLP}} = n \cdot N_M \cdot \text{Br}\left(M \to n\,\text{LLP}\right) , \tag{5.3.1}$$

is determined from the number of produced mother particles, $N_M = \mathcal{L}\ \sigma_M$ for luminosity $\mathcal{L}$ and mother particle production cross-section. $\text{Br}\left(M \to n\,\text{LLP}\right)$ is the branching ratio of the mother particle into n long-lived particles. From this, the number of LLPs detected at ANUBIS is calculated,

$$N_{\text{LLP}}^{\text{detect.}} = P_{\text{detect.}} \cdot N_{\text{LLP}} \cdot \text{Br}\left(\text{LLP} \to X\right) , \tag{5.3.2}$$

for the number of LLPs decaying into a set of final states X and the probability of detection $P_{\text{detect.}}$. The probability is acquired using Monte Carlo simulations, where the percentage of produced LLPs reaching the detector is determined,

$$P_{\text{detect.}} = \frac{N_{\text{obs.}}}{N_{\text{tot.}}} . \tag{5.3.3}$$

Here the fraction of the LLPs detected at ANUBIS ($N_{\text{obs.}}$) given a total number of LLPs produced in the simulations ($N_{\text{tot.}}$) is found. The geometry of the detector and the kinematic distributions of the LLPs are taken into account when $N_{\text{obs.}}$ is derived.

For both the studies of dark scalars, $\sigma_M = \sigma_{\text{Higgs}}$ is the production cross-section of the Higgs, and the branching ratio of the Higgs decaying into two dark scalars

$\mathrm{Br}(H \to SS)$ is considered for $n = 2$ dark scalars produced. As the dark scalars are assumed to decay into only $b\bar{b}$-pairs, $\mathrm{Br}\left(\mathrm{LLP} \to X\right) = \mathrm{Br}\left(\mathrm{LLP} \to b\bar{b}\right) = 1$. The sensitivity projections are found for *High-Luminosity* LHC (HL-LHC) with $\sqrt{s} = 14$ GeV and $\mathcal{L} = 3$ ab^{-1}. For varying dark scalar masses, the projections for $\mathrm{Br}(H \to SS)$ were found as a function of the decay length $c\tau$, where τ is the LLP lifetime [48, 82]. See section 5.5 for further detail.

5.3.2 Heavy Neutral Leptons

The bounds seen in Figure 4.11 for ANUBIS (in dashed purple) are based on the findings in [92], which performed sensitivity studies for HNLs. Through an implementation of a $U(1)_{B-L}$ symmetry and considering one HNL mixing with either the Standard Model electron or muon neutrinos, the study calculates the projections for ANUBIS. The outdated shaft configuration was used, the projections were found assuming zero background events, and all visible decay channels for HNLs were included.

The number of LLPs detected at ANUBIS was calculated using the same method as described above for the dark scalar studies, but for a range of mother particles together with the HNLs decaying into all visible final states. The sensitivity projections were found for HNLs produced by B and D mesons,

$$\mathrm{Br}(B \to \mathrm{LLP} + X) \cdot \mathrm{Br}(\mathrm{LLP} \to \mathrm{vis.}) \quad \text{and} \quad \mathrm{Br}(D \to \mathrm{LLP} + X) \cdot \mathrm{Br}(\mathrm{LLP} \to \mathrm{vis.}),$$

as a function of $c\tau$. The study compares the projections for the HNL mixing angle, $|U_\alpha|^2$ for $\alpha = e, \mu$, as a function of the HNL mass for several mother particles, $M \in \{B - \mathrm{meson}, D - \mathrm{meson}, Z, t, W, h\}$, and the combined projections for ANUBIS were compared to other LLP detectors.

Similarly to the studies described above, most sensitivity studies for detectors specialising in LLPs consider either one dominating decay channel with $\mathrm{Br} = 1$, or all decay channels equally by using the branching ratio into visible final states. This

method, for example, does not take into account the additional parton showering involved when hadrons are produced, as opposed to leptons. In order to address this, the software development, which is a part of the ongoing sensitivity study of the ANUBIS collaboration, will now be presented.

5.4 SET-ANUBIS

To create model-independent and reproducible sensitivity projections for the ANUBIS detector, it was decided to develop a software package, *SEnsitivity sTudies for ANUBIS* (SET-ANUBIS). The aim of SET-ANUBIS is to allow any user to produce sensitivity projections for any implemented LLP model with the ability to study each individual production mode and decay channel/final state.

In Figure 5.3, an example LLP path is presented. The LLP is initially produced in the ATLAS detector before travelling through it (dashed black line), then traversing the cavern before decaying (dotted black line) into a jet of decay products that will be detected by ANUBIS if charged (full black cone). To cover these individual stages, the software is separated into five parts. First the input and implementation of LLP models, which provides the foundation for the subsequent simulations of the LLP production in ATLAS and resulting kinematic distributions. The next two stages are the decays in the cavern and the detection of the final states in ANUBIS, providing the number of signal events used to finally calculate the sensitivity projection.

The remainder of this section will focus on the individual parts of SET-ANUBIS, particularly on the implementation and choice of dark matter models considered. It is worth noting that SET-ANUBIS is still under development, and hence the following sections describe the current structure of the software, but it is subject to change.

5.4.1 Dark Matter Model Input

In order to allow any user to find the ANUBIS sensitivity for any potential model, one has to construct a model-independent and user-friendly software. With this in mind, it was decided to use a Python runner script for the input and implementation of the dark matter models which contain the LLPs considered. The main purpose of the script is to produce a UFO model file [93] for a particular LLP model, and derive the total width of the LLP alongside the widths of each production mode and decay channel. These widths will subsequently be passed on to the simulation softwares to calculate the appropriate branching ratios.

There are three possible options (and a combination of them) for the input of the dark matter model will be available in SET-ANUBIS: a FeynRules model [30], individual formula for decay widths of the LLPs in Python, and a number for the total width of the LLP. The latter two are optional, whereas the first is required.

The FeynRules model is handled in Mathematica [94] and used to calculate the branching ratios of the production modes of the LLP considered. This is necessary

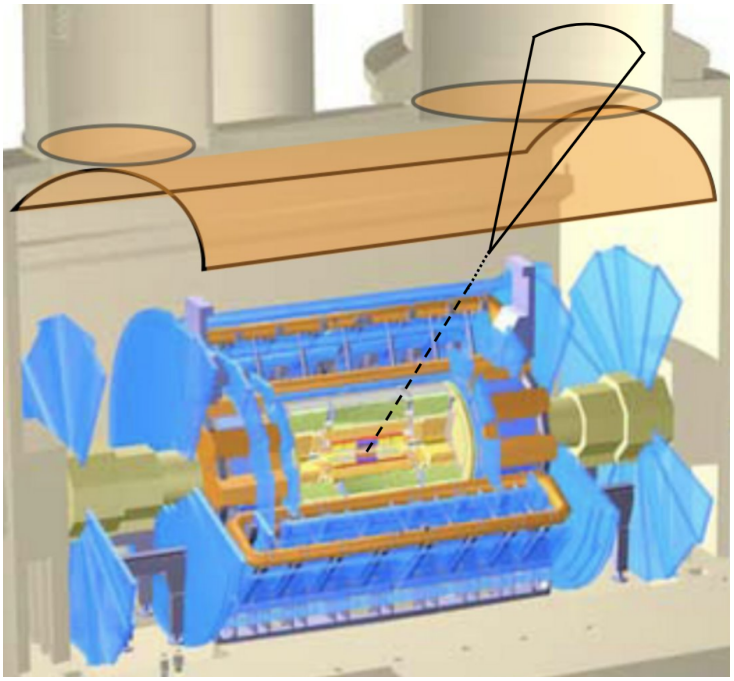

Figure 5.3: Production at ATLAS (dashed), decay in cavern (dotted), and detection at ANUBIS (full) of a long-lived particle (Modified from [84]).

as, when introducing a new particle which interacts with SM particles, one has to consider how this changes the branching ratios of the SM particles. From the FeynRules model, the widths for the LLP decay channels can be derived and afterwards exported to Python. Alternatively, formulas for the decay widths can be provided in Python. Using either sets of formulas, the total width of the LLP as a function of its mass and coupling constant(s) is derived. This is used to calculate the characteristic decay length and displace the decay to be inside the cavern between ATLAS and ANUBIS.

Additionally, one needs to consider the possibility of a wider dark sector where either the LLP is a portal or several new particles interact with the SM. This is accounted for by allowing the user to provide total widths, which will be used to rescale all branching ratios calculated.

Using the example of heavy neutral leptons, the choice of using individual decay width formula will be justified. The mass range for HNLs considered at ANUBIS is 0.1–10 GeV for which, as seen in section 4.2.4, all decays are mediated through $W^{\pm}$ and Z^0 bosons which are integrated out. Alone, this EFT lagrangian could be used to create an UFO model. But for HNLs with masses below 1 GeV, the produced quark pairs form mesons, and hence a modified EFT containing mesons rather than quarks would have to be used. Above 2 GeV the quark pairs are free, and the initial EFT can be used, whereas the intermediate range, $1\,\text{GeV} < m_{\text{HNL}} < 2\,\text{GeV}$, is more complicated. Therefore, in order to fully represent the decays of HNLs, one has to use at least two different UFO models and make a choice of how to interpolate between the two. Calculating the branching ratios directly from the decay width formulas prevents this.

For LLPs with more than one coupling to the SM, as seen in section 4.2.3 for ALPs, both production and decay modes can be included or excluded through setting couplings to zero. In general, it will be assumed that only one coupling needs to be considered through the remaining couplings being negligible or constant.

5.4.2 Production Simulations

The dark matter UFO model generated by Mathematica is passed to the simulation for production of LLPs in ATLAS. For this it was decided to use both Pythia [35] and MadGraph [36], though it is worth noting that MadGraph uses Pythia to handle the parton showering and hadronisation. Both simulations softwares lack the ability to have the production of LLPs through decays of mesons. Hence, with consent of the SHiP Collaboration, the *FairShip* software [95] was modified in order to implement the production and decay of mesons in Pythia.

Each production mode will be split into multiple parts; production cross-section for the mother particle(s), the branching ratio of the mother particle(s) decaying into the LLP, and the kinematic distribution of the LLP and potentially accompanying particles. The production branching ratios are calculated by the simulation software using the UFO model or the widths provided by the Python runner script.

The subsequent decay of the LLP in the cavern is done in Pythia, where the width for each possible decay channel and the total width of the LLP is again provided by the Python runner script. The branching ratio for each possible decay channel is calculated by Pythia for the values of the LLP mass and coupling constant(s) considered. By adding new decay channels for both mother particles and the LLP with associated widths, Pythia calculates the branching ratios by either summing over all decay channels or using a total width provided. This procedure allows for a model-independent approach where a potential wider dark sector can be taken into account.

As described in section 3.2.3, the simulation softwares (independent of the particular generator) output the kinematic distributions of the final states of the processes considered. These are passed to a python script which considers the ANUBIS geometry and produces the number of signal events for the distribution. The script is an extension of the work in [48].

5.4.3 ANUBIS Geometry

When considering the detection of LLPs in ANUBIS, one has to take the formation of jets into account. This is carried out in FastJet [96], where the final state particles produced by Pythia are grouped into jets by *jet clustering algorithms*. There exists different types of algorithms, though they generally cluster final state particles together by their distance to surrounding particles compared to the distance to the incoming beams. The most energetic particles are clustered first and neighbouring softer particles are added to the jet up to the *jet radius* R [28].

Figure 5.4 displays the creation of two jets at the interaction point (primary vertex) and a third, displaced jet at a secondary vertex due to the decay of a long-lived particle. A signal at ANUBIS consists of one and only one jet hitting at least one tracking station of the detector. The presence of any other jets near ANUBIS will be categorised as a background event and neglected. The radius between the signal and any other jet is defined, $\Delta R = \sqrt{(\Delta\eta)^2 + (\Delta\varphi)^2} > 0.5$, for pseudo-rapidity η, see eq. (3.2.8), and azimuthal angle ϕ [48].

Additionally, the detection of the final state particles in the ANUBIS fiducial volume

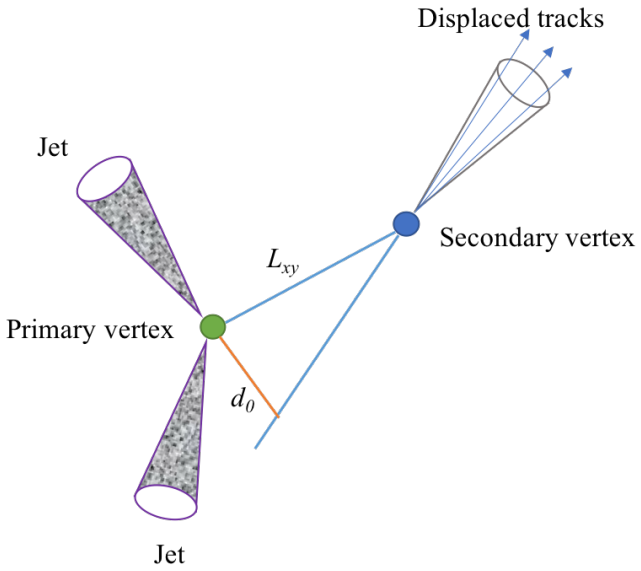

Figure 5.4: Depiction of two jets from the primary vertex and a displaced jet at a secondary vertex (from [97]).

is implemented within SET-ANUBIS through a series of cuts on the energy, momentum, and angular distribution of the particles, to mention a few. Using *cut flow diagrams*, the different production and decay channels can be studied in order to determine the most important processes. In doing so, later detector efficiencies can be incorporated, for example for the detection of a specific particle or grouping of particles such as quarks or leptons. The cut flow diagrams visualise the reduction in signal and background events for each cut introduced, allowing for the development of cuts which remove the most background whilst keeping the signal events.

All together the ANUBIS geometry gives a total number of signal events which is compared to an expected number of background events.

5.4.4 Sensitivity Projections

In order to find the sensitivity projection for ANUBIS, one needs an estimate of the expected background. The shaft configuration had an expected number of SM background events of 50, found using ATLAS muon spectrometer searches [82]. This is updated for the ceiling configuration by rescaling the active volume,

$$N_{\text{events-ceiling}} = N_{\text{events-shaft}} \cdot \sqrt{\frac{V_c}{V_s}} = 50 \cdot \sqrt{3.2} \approx 90, \tag{5.4.1}$$

for $V_{c,s}$ the active volumes of the ceiling and shaft configurations respectively (For further detail see [48]).

The main Standard Model background arises from long-lived, neutral SM particles such as the neutron (n^0) and K-Long (K_L^0), a long-lived, neutral kaon. As both particles escape ATLAS without being detected, they can scatter off the atoms in the air in the cavern, creating jets that can be detected by ANUBIS. The neutron has a mean lifetime of 878.4 s whereas the K-Long has a much shorter lifetime of 5.116×10^{-8} s [2], thus their characteristic decay lengths ($\lambda = c\tau$) are 2.633×10^{11} m and 15.34 m respectively. The K-Long can therefore decay inside the cavern into muons that act as a background to ANUBIS, but the background from neutrons is

purely from scattering of air atoms [48].

In the future, a more thorough investigation needs to be carried out for the SM background, using for example Monte Carlo simulations. When this analysis has been carried out, it will inform and update the analysis of the importance of each production and decay channel. Each has associated final state configurations which will have differing backgrounds.

Sensitivity projections for the ANUBIS detector are calculated by rescaling the number of signal events found for a certain value of the coupling constant(s) and LLP mass, finding the coupling value for which 90 signal events are detected. For LLP models with only one varying coupling constant, the rescaling is easily done as the number of signal events is proportional to the coupling squared.

5.4.5 Software Overview

Having described each stage of SET-ANUBIS, the following section presents a general overview of the software. Table. 5.1 shows the specifications for each module, where the initial input of dark matter models is handled with a Python runner script and UFO models using FeynRules in Mathematica, the main simulations of the events are carried out in Pythia and MadGraph, and the final detection and acceptance in ANUBIS is implemented in a Python script.

Component	Software
Input	Mathematica [94] & Python Runner Script
Simulations	Pythia [35] & MadGraph [36]
ANUBIS Geometry & Sensitivity Projections	Python Script

Table 5.1: Overview of the softwares used for each stage of SET-ANUBIS.

Figure 5.5 displays the flow diagram for SET-ANUBIS from theoretical inputs on the left to the final sensitivity projection in the lower-right corner. The light blue

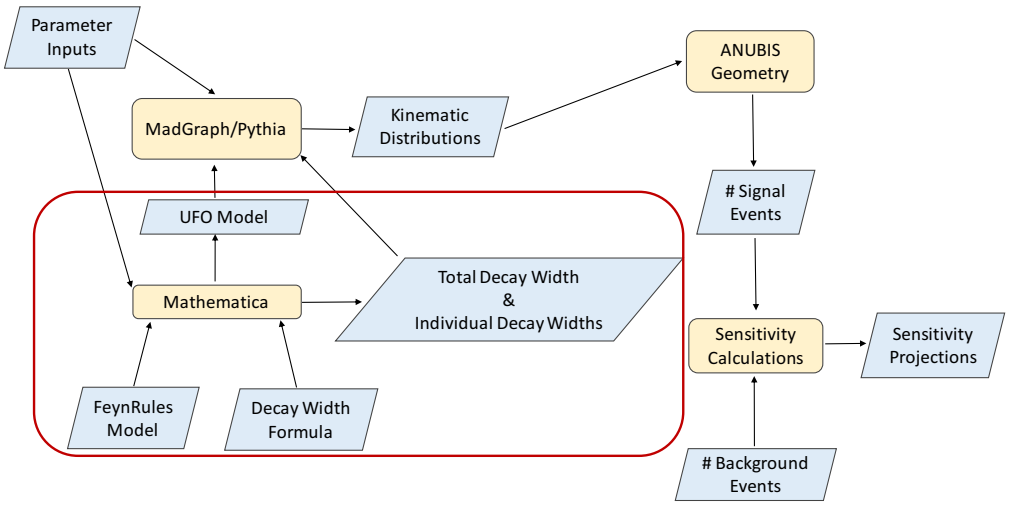

Figure 5.5: Flow diagram for SET-ANUBIS with the contributions from the author of this thesis highlighted by the red box.

parallelograms represent input and output from modules seen in light orange rounded squares. It can be seen here how each module interlinks with the others. Both the calculations of width in Mathematica and the MadGraph/Pythia simulations will rely on the same parameter input such that the final results are consistent. The part of SET-ANUBIS which is the work by the author of this thesis is enclosed in the red box seen in the Figure. This includes the implementation of FeynRules models, production of UFO models, and calculations of branching ratios of both the production and decay modes for the LLP. The SET-ANUBIS GitLab is available upon request from the reader.

5.5 Current ANUBIS Studies

There are two approaches to sensitivity studies; how does the experiment compare to others, and what is the experiment uniquely good at. It was decided to start with producing the ANUBIS sensitivity to the benchmarks described by the *Feebly-Interaction Particles* Group (FIPs) [7], such that the projections can be included on the plots seen in section 4.4. Starting with updating the previous study of ANUBIS

performance for heavy neutral leptons [92], as this used the outdated ANUBIS shaft configuration, and the selection cuts for the detector has been updated.

5.5.1 FIPs Benchmark Models

The FIPs benchmarks consists of four models; dark photon, heavy neutral leptons, dark scalar, and axions as described in section 4.2 and Appendix A. A brief outline of the models can be found in Table 5.2. These benchmarks will briefly be presented

Dark Matter Model	Particle	Spin	Coupling
Dark Photon	A_μ	1	$-\frac{\epsilon}{2\cos\theta_W}F'_{\mu\nu}B^{\mu\nu}$
Dark Scalar	S	0	$\left(\mu_S S + \lambda_S S^2\right) H^\dagger H$
ALPs	a	0	$\frac{a}{f_a}F_{\mu\nu}\tilde{F}^{\mu\nu}$, $\frac{a}{f_a}G_{i,\mu\nu}\tilde{G}_i^{\mu\nu}$, $\frac{\partial_\mu a}{f_a}\bar{\psi}\gamma^\mu\gamma^5\psi$
Heavy Neutral Leptons	N	$\frac{1}{2}$	$FLHN$

Table 5.2: Long-lived particle models for FIPs benchmarks

here, for further detail see [7]. Due to the ANUBIS detector's construction, not all benchmarks are relevant for the sensitivity study. For all benchmarks considered, it was decided to keep the parameter space simple, and if possible only consider two parameters for each; the mass of the LLP and a coupling constant.

For the simplified kinetic mixing model of a dark photon vector portal, see section 4.2.2, benchmark BC1 is defined where the mass and coupling constant are the only two parameters. Introducing a dark sector, for which the dark photon is a portal, with at least one particle of mass m_χ and coupling constant $\alpha_D = g_D^2/(4\pi)$, two more benchmarks are available (BC2 and BC3). These will not be considered any further as the dark photon predominantly decay into the dark sector, which is undetectable.

The scalar portal has a new scalar dark particle mixing with the SM Higgs boson with linear $\mu_S S H H^\dagger$ and pair $\lambda_S S^2 H H^\dagger$ couplings. The specifics of the model can

Vector Portal		
BC1	*Minimal dark photon model*	$\{m_{A'}, \epsilon\}$
BC2	*Light dark matter coupled to dark photon*	$\{m_{A'}, \epsilon, m_\chi, \alpha_D\}$
BC3	*Milli-charged particles*	$\{m_\chi, Q_\chi/e\}$ for $m_{A'} \to 0$ and $\lvert Q_\chi\rvert = \lvert\epsilon g_D e\rvert$

be found in Appendix A. Defining mixing angle,

$$\theta = \frac{\nu\mu_S}{m_H^2 - m_S^2}\,, \tag{5.5.1}$$

two benchmarks for $\lambda_S = 0$ (BC4) and $\lambda_S > \mu_S$ (BC5) are found. The FIPs group recommends the use of $\lambda_S \simeq 5 \times 10^{-4}$ for BC5. The second benchmark (BC5) is the foundation for the dark scalar study in [48] and [82].

Scalar Portal		
BC4	*Higgs-mixed scalar*	$\{m_S, \theta\}$
BC5	Higgs-mixed scalar with large pair-production	$\{m_S, \lambda, \theta\}$ for large λ

All three possible mixings between a heavy neutral lepton and the three SM neutrinos, see section 4.2.4, are available at ANUBIS, where the three benchmarks (BC6-8) assume one mixing dominating over the two others.

Neutrino Portal (One HNL)		
BC6	*Electron dominance*	$\{m_{\text{HNL}}, \lvert U_e\rvert^2\}$
BC7	*Muon dominance*	$\{m_{\text{HNL}}, \lvert U_\mu\rvert^2\}$
BC8	*Tau dominance*	$\{m_{\text{HNL}}, \lvert U_\tau\rvert^2\}$

The ALP model presented in section 4.2.3 has three main couplings to photons, gluons, and fermions respectively, for which three separate benchmarks (BC9-11) are created with only one coupling being non-zero. For simplicity, it is assumed that the ALP couples equally to leptons and quarks $c_l = c_q = c_f$. Currently, the ANUBIS detector will not be able to detect photons and gluons, and hence BC9 and BC11 are not considered. However, there is the possibility for photons to be detected in the future.

Axion "Portal"		
BC9	*Photon dominance*	$\{m_a, c_\gamma\}$
BC10	*Fermion dominance*	$\{m_a, c_l^{-1}, c_q^{-1}\}$
BC11	*Gluon dominance*	$\{m_a, c_{\tilde{G}}^{-1}\}$

Having presented the FIPs benchmarks, the current developments on the sensitivity studies of HNLs at ANUBIS will be reported.

5.5.2 Heavy Neutral Lepton Study

The development of SET-ANUBIS is being carried out with the study of HNLs as a prototype. At the finalisation of the HNL sensitivity projections, it is expected that the SET-ANUBIS software will be functionally complete. Additional developments, such as the modelling of the detector backgrounds, are expected to be carried out later. This will allow for the production of projections for the other FIPs benchmarks described above shortly after the HNL results.

At the time of the writing of this thesis, the sensitivity projections for HNLs are not finalised, but are expected to be soon. Instead, an overview of the current progress will be presented. Using FeynRules [30] and UFO model files provided by [69] and the decay widths described in Appendix B, the heavy neutral lepton model is fully implemented. The widths of production and decay modes as functions of HNL mass and mixing angles U_α have been derived. The simulations of production of HNLs have been completed in MadGraph, and the mesonic production implemented in Pythia. Almost all ANUBIS detection and geometry cuts are incorporated, together with the calculations of the sensitivity projections. The remaining tasks are to ensure communication between the different modules, and the finalisation of the acceptance cuts on jets in the detection at ANUBIS.

The previous HNLs sensitivity study [92] found that production through meson decay were the largest contributions, followed by the Z and W bosons, and lastly the top quark [92]. This is expected to change when considering the more transverse ceiling

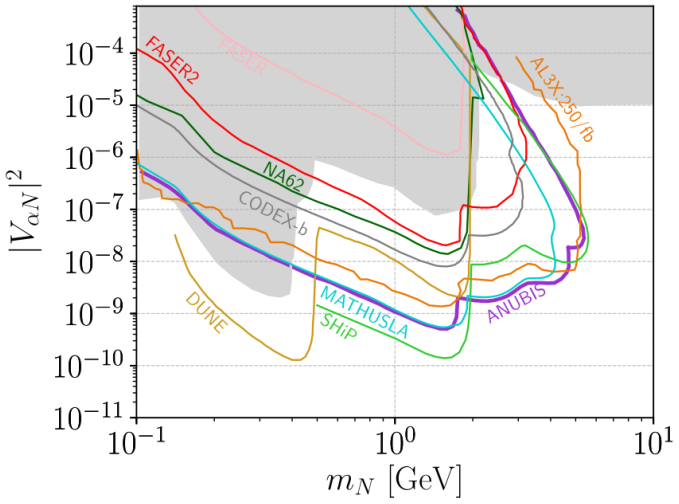

Figure 5.6: HNL projections for ANUBIS for HNL mixing $|V_{\alpha N}|^2$ with $\alpha \in \{e, \mu\}$ and HNL mass m_N (from [92]).

configuration, compared to the service shaft. Therefore, each production channel should be analysed to determine the updated contributions for each.

As previously seen in Figure 4.6, at varying HNL masses different decay channels dominate. The purely leptonic decay channels will induce significantly less showering and hadronisation, and therefore presents as "cleaner" final states. The contributions for each grouping of final state will be analysed to better understand the detector performance.

At the finalisation of the HNL study, the projection for ANUBIS from [92], seen in Figure 5.6, will be updated for the ceiling configuration. The projection displayed is for one HNL which mixes with either electron or muon neutrinos for $|V_{\alpha N}| = |U_\alpha|$. The grey region shows already experimentally excluded parameter space, whereas the coloured lines are projections from DUNE [98] and other LLP detectors such as MATHUSLA [99].

For HNL masses $\gg m_{\mu,e}$, the masses of electrons and muons can be assumed equal, and the production and decay rates for electron and muon mixing are therefore mostly the same. With the assumption that ANUBIS will have approximately equivalent efficiencies to the detection of electrons and muons, the sensitivity to electron- and muon-mixing can be taken to be equal. The mixing with tau-neutrinos

is not considered due to the additional decay and showering from the tau mass being significantly larger than the other two leptons. See [92] for further detail.

Figure 5.7 displays the branching ratio of Higgs to two dark scalars, $\mathrm{Br}(H \to SS)$, as a function of the decay length $c\tau$. As described previously in section 5.3, the two scalars are assumed to decay solely into $b\bar{b}$-pairs [48]. It can be here seen how the ceiling configuration has a significantly better sensitivity than the shaft configuration. Here "PX14" refers to the PX14 installation shaft in ATLAS, the right service shaft on the left panel of Figure 5.1. The difference between the "cavern or shaft decay" and "shaft decay" projections is the restriction that the latter has the LLP decay inside the service shaft, whereas the first includes the possibility of decays in the cavern. The projections are found for 4 (dashed lines) and 90 (full lines) signal events for no background events and the expected number of background events from the ATLAS muon spectrometer as described earlier. The width of the projections, best seen around $c\tau \approx 10^5$ m, is given by the statistical uncertainty given by the standard

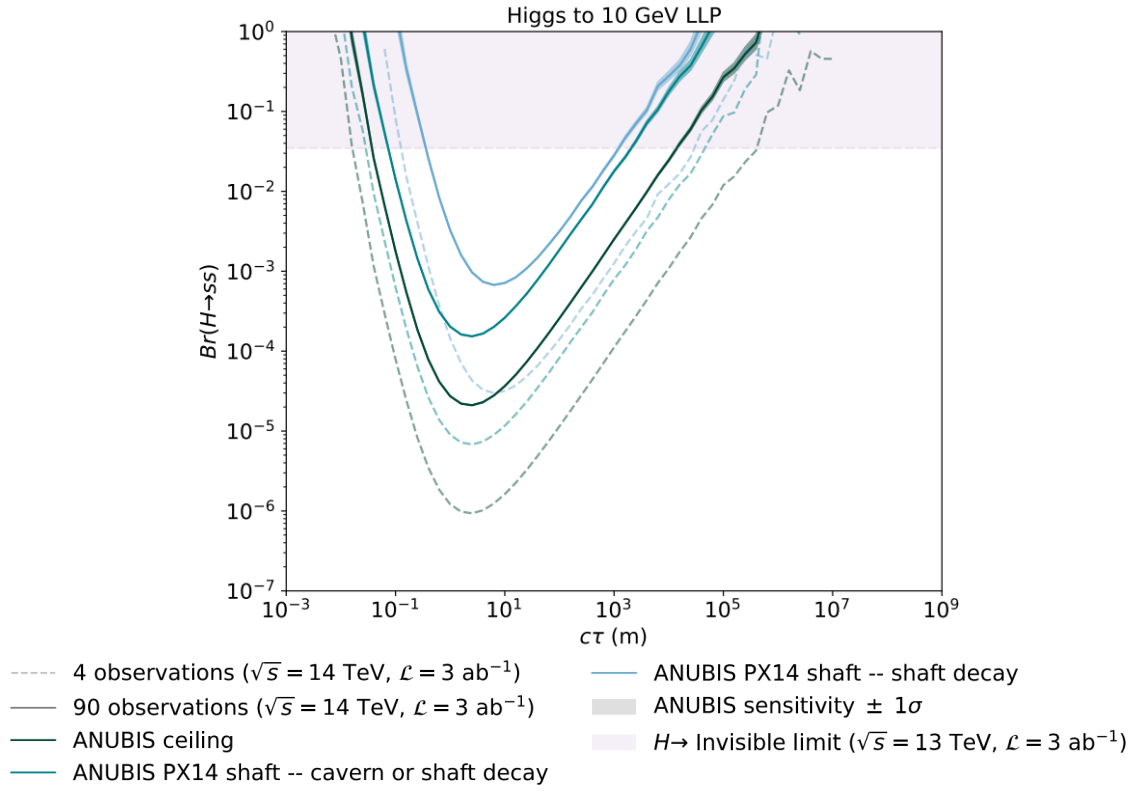

Figure 5.7: ANUBIS projection for branching ratio of Higgs to two dark scalars, $m_{\mathrm{LLP}} = 10$ GeV, and $c\tau$ (from [48]).

deviation of the Poisson distribution of generated events with mean N_{obs}, $\sigma = \sqrt{N_{\text{obs}}}$. The projected limit for HL-LHC of the Higgs decay into invisible particles is seen as the shaded band across the top [48].

The ANUBIS sensitivity projections in Figure 5.6 were found for 3 signal events where no background is assumed. This exact result is expected to improve for the ceiling configuration, increasing the reach of ANUBIS. But as the expected sensitivity projection for ANUBIS will require 90 signal events, it is not certain whether the projections found with SET-ANUBIS will increase the sensitivity found in [92].

5.6 Outlook

When the initial sensitivity study of ANUBIS has been finalised for the FIPs benchmarks, the detector will be able to easily be compared to other detectors specialising LLPs. The next step is to consider specific processes and LLP models that ANUBIS has unique sensitivity to. One example of such process is the decay of a Higgs boson into an axion-like particle and either a Z boson or a photon, $h \to \text{ALP} + Z/\gamma$. The initial Higgs production and decay are prompt, and the photon or following prompt decay of the Z boson will be detected by ATLAS. Currently, the ALP in this process will show up purely as missing energy, but ANUBIS proposes the possibility of detecting the ALP decay products. With the integration into the active-veto system of ATLAS, ANUBIS will be able to connect the photon or prompt Z decay with the displaced decay of the ALP in the cavern. Therefore, the otherwise missing energy is correctly assigned to the ALP, and the $\{h\ \text{ALP}\ Z\}$ and $\{h\ \text{ALP}\ \gamma\}$ couplings can be studied.

5.7 Conclusion

The ANUBIS detector is a low-cost extension to the ATLAS detector, increasing the reach for long-lived particles with small masses and coupling constants. The

proposals for the designs of the detector were described, the service shaft and ceiling configurations, together with the prototype proANUBIS. An overview of the previous studies of the ANUBIS detector for heavy neutral leptons and dark scalars was included, summarising the points which SET-ANUBIS seek to address such as the individual study of the LLP decay channels.

The current status of the sensitivity studies of ANUBIS is the development of the SET-ANUBIS software by the ANUBIS collaboration. The software implements arbitrary LLP models, like the ones described in the previous chapter, and creates the sensitivity projections for the detector. It performs simulations of production in ATLAS, travel and subsequent decay in the surrounding cavern, and final detection by ANUBIS. Aiming to increase the complexity and accuracy of the sensitivity projections, SET-ANUBIS allows for the study of individual production and LLP decay modes. The initial plans for SET-ANUBIS are updating and creating projections for the FIPs benchmarks, which are presented.

The ANUBIS detector relies on the LLPs produced to decay into visible, charged final states. Hence, if the LLP is a portal to a dark sector into which the LLP dominantly decays, ANUBIS will not be able to detect anything. The studies presented above make theoretical assumptions about models and parameters; introducing one LLP and varying one coupling constant at a time. These assumptions are necessary when performing searches for dark matter with current detector designs. Therefore in the following chapter, a novel method to distinguish different dark matter models in missing energy searches is presented.

Chapter 6

How to measure the spin of invisible states in $e^+e^- \to \gamma + X$

6.1 Introduction

The ANUBIS detector addresses the noise present in proton-proton collisions by being placed away from the interaction point. But larger actions can be taken to reduce noise can be done; using a lepton collider. In particular for missing energy searches, where the dark matter particle decays into a dark sector, the signals become swamped by the background and noise at hadron colliders.

It is here discussed how one can take advantage of the clean environment at e^+e^- colliders and use the angular distribution of the final state photons, polarised beams, and final state photon polarisation to identify the spin and the coupling structure of two invisible states; the spin 1 dark photon and spin 0 ALPs as introduced previously. Searches for missing energy at electron positron colliders with a final state photon, $e^+e^- \to \gamma + X$, are one of the most sensitive probes for invisible states X with masses in the range $0.1 - 9$ GeV. The existence of such a signal, the measurement of one jet plus missing energy, is not possible in a *pp* collider. With unequal beam energies, $E_{e^+} = 4$ GeV and $E_{e^-} = 7$ GeV, and a centre-of-mass energy of $\sqrt{s} = 10.58$ GeV, Belle II will provide a valuable opportunity to search for these signatures [100].

This search provides a complimentary search to the ones performed at ANUBIS. For ALPs such a search has been proposed first by Wilczek [101] and searches have been performed with CLEO [102] and BaBar [103, 104]. For Belle II, projections are available [105–107]. A search for dark photons has been performed by BaBar [108] and a projection for Belle II can be found in [100]. Each study assumes the existence of one dark matter particle, and interpret searches for missing energy and a single photon as a signal in that model. The search strategy proposed in [100] is extended, and observables, that can distinguish between the different models in the case where a signal is observed, are identified.

The rest of this chapter is organised as follows. In section 6.2, the dark photon and axion-like particle Lagrangians are introduced, and in section 6.3 how the differential cross-sections with and without polarised beams can be used to identify the production process is discussed. In section 6.4, simulations and analyses for signal and background are presented, and an improvement to the search strategy is proposed. The implications of measuring the photon polarisation are discussed in section 6.5, and in section 6.6 the sensitivity reach for future runs of Belle II is presented.

6.2 ALP & Dark Photon Lagrangians

Two minimal models of invisible states, that can be produced via $e^+e^- \to \gamma + X$, that carry either spin 1 or spin 0 will be compared. Here the dark photon and axion-like particle are considered. As seen in section 4.2.2, the relevant terms for the spin 1 field or dark photon are given by

$$\mathcal{L} \supset -g_X \bar{\psi} \gamma_\mu \psi X^\mu - \frac{m_X^2}{2} X_\mu X^\mu \,, \tag{6.2.1}$$

where m_X is the mass of the dark photon and g_X denotes its coupling strength to fermions. In the case of kinetic mixing one can write $g_X = \epsilon\, e\, Q_\psi$, where ϵ is the coefficient of the kinetic mixing term of the electromagnetic field strength tensor

$F_{\mu\nu}$ and the dark photon field strength tensor, and Q_ψ is the electric charge of the fermion ψ in units of the electron charge e [109–112]. Interactions due to mixing with the Z boson are suppressed for masses $m_X \leq 10$ GeV, but can play a role for dark photons with masses closer to the Z-pole [58, 113].

In the case of the spin 0 particle, an ALP a is considered with interactions given by

$$\mathcal{L} \supset c_f \frac{\partial_\mu a}{2f} \bar{f} \gamma^\mu \gamma_5 f - c_\gamma \frac{a}{f_a} F_{\mu\nu} \tilde{F}^{\mu\nu} - \frac{m_a^2}{2} a^2 \,, \tag{6.2.2}$$

where, as described in section 4.2.3, c_f and c_γ are coupling constants, and m_a is the mass term, though m_X is used to denote the mass of the new particle when referring to both the dark photon and ALPs. The coupling to gluons will not be included as, at tree level, it does not appear in $e^+e^- \to \gamma + \text{ALP}$ processes.

The main differences between the models are their spin, the coupling structure to fermions, and the ALP coupling to photons. The production of the dark photon only occurs though couplings to the electron, whereas for the ALP there are two contributions. The corresponding Feynman diagrams are shown in Figure 6.1.

In section 4.2.2, it was shown that dark photons in $e^+e^- \to \gamma + X$ at Belle II will decay within the detector if only considering decays back into SM particles. Therefore, in all cases the dark photon and ALP are considered not to decay into SM particles on collider scales, e.g. by introducing a dominant decay into dark sector with a set of invisible particles for which the invisible states act like portals. Otherwise, for the mass range considered here with masses up to $m_X = 9$ GeV, both the dark photon and ALP decay back into electron positron or photon pairs. Due

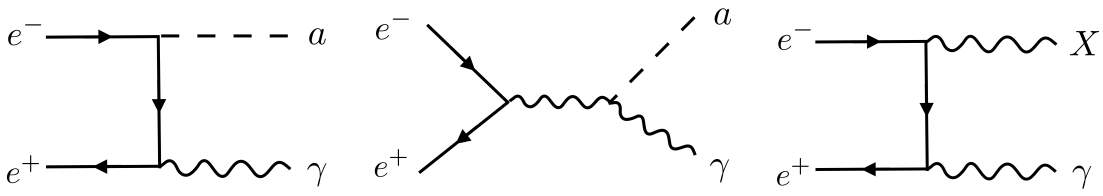

Figure 6.1: Different contributions to the production of ALPs (left and middle) and dark photons (right) at an e^+e^- collider.

to this, throughout this chapter the state X in the process will be referred to as an invisible state rather than a dark matter particle. Neglecting subleading terms suppressed by the electron mass, as seen in eqs. (4.2.23), (4.2.35), and (4.2.36), the corresponding decay lengths for the three models read

$$\begin{aligned}
\ell(g_X) &= \left(\frac{g_X^2 m_X}{12\pi}\right)^{-1} \approx 7\times 10^{-15}\left[\frac{1}{m_X g_X^2}\right]\mathrm{GeVm}\,,\\
\ell(c_e) &= \left(\frac{c_e^2 m_a m_e^2}{8\pi f_a^2}\right)^{-1} \approx 2\times 10^{-8}\left[\frac{f_a^2}{m_a c_e^2}\right]\mathrm{GeV}^{-1}\mathrm{m}\,,\\
\ell(c_\gamma) &= \left(\frac{c_\gamma^2 m_a^3}{4\pi f_a^2}\right)^{-1} \approx 2\times 10^{-15}\left[\frac{f_a^2}{m_a^3 c_\gamma^2}\right]\mathrm{GeVm}\,.
\end{aligned} \tag{6.2.3}$$

6.3 Angular Distributions

In the following, it will be discussed how the angular distribution of the final state photon in the process $e^+e^-\to\gamma+X$ can be used to discriminate between the dark photon and ALP final states as well as between the ALP coupling to electrons and photons. In general the amplitude for the process,

$$e^+(p_1,\lambda_{e^+})+e^-(p_2,\lambda_{e^-})\to\gamma(q_1,\lambda_\gamma)+X(q_2,\lambda_X)\,, \tag{6.3.1}$$

can be written as $\mathcal{M}=\mathcal{M}_\mu\epsilon^\mu(q_1,\lambda_\gamma)$ for photon polarisation vector ϵ^μ and helicities $|\lambda_{e^\pm}|=\frac{1}{2}$, $|\lambda_\gamma|=1$, $|\lambda_X|=0$ for the ALP, and $|\lambda_X|=1$ for the dark photon, respectively. As described in section 2.2.4, the helicity and chirality of a massive fermion are not the same, and hence the helicity of the incoming fermions will distinctly be referred to in this chapter.

The partial amplitude,

$$\mathcal{M}_\mu=\bar v(p_{e^+},\lambda_{e^+})\Gamma_\mu u(p_{e^-},\lambda_{e^-})\,, \tag{6.3.2}$$

is written for the current of the interaction Γ_μ. Using eq. (2.2.24) for massless fermions, it is found that the amplitude is proportional to two possible combinations of incoming helicities, see Table. 6.1.

	Equal Beam Helicities $\lambda_{e^-} = \lambda_{e^+} = \lambda$	Opposite Beam Helicities $\lambda_{e^-} = -\lambda_{e^+} = \lambda$
$\frac{1}{4}(1 + 2\lambda_{e^+}\gamma^5)(1 + 2\lambda_{e^-}\gamma^5)$	$\frac{1}{2}(1 + 2\lambda\gamma^5)$	0
$\frac{1}{4}(1 + 2\lambda_{e^+}\gamma^5)(1 - 2\lambda_{e^-}\gamma^5)$	0	$\frac{1}{2}(1 - 2\lambda\gamma^5)$

Table 6.1: Combinations of incoming beam helicities for $|\lambda| = \frac{1}{2}$.

From these one finds that axial and vector interactions, $\Gamma_\mu \in \{\gamma^\mu, \gamma^\mu\gamma^5\}$, require the electron and positron helicities to be opposite sign, as otherwise the amplitude goes to zero. Whereas for (pseudo-)scalar, and tensor, $\Gamma_\mu \in \{1, \gamma^5, \sigma^{\mu\nu} = \frac{i}{2}[\gamma^\mu, \gamma^\nu]\}$ interactions, the helicities signs must be equal. For massive leptons, contributions from both opposite and equal sign helicities will be present, but the massless case will dominate due to mass suppression of $\mathcal{O}(m_e^2/s)$.

In order to calculate the amplitude, the momenta of the particles are defined as

$$p_1^\mu = \left(E_1, 0, 0, -\sqrt{E_1^2 - m_e^2}\right) , \tag{6.3.3}$$

$$p_2^\mu = \left(E_2, 0, 0, \sqrt{E_2^2 - m_e^2}\right) , \tag{6.3.4}$$

$$q_1^\mu = E_\gamma \left(1, \cos\phi\sin\theta_{\text{lab}}, \sin\phi\sin\theta_{\text{lab}}, \cos\theta_{\text{lab}}\right) , \tag{6.3.5}$$

$$q_2^\mu = p_1^\mu + p_2^\mu - q_1^\mu , \tag{6.3.6}$$

where E_γ is the photon energy in the laboratory frame, θ_{lab} is the angle between the photon and incoming beams, and ϕ between the photon and the x-axis in the transverse plane. At Belle II, the incoming beams are angled 83 mrad with respect to each other, with the z-axis defined with equal distance to the beams [100]. This distinction is assumed to have little effect on the results presented in this chapter, and hence it is assumed that the beams are antiparallel along the z-axis with energies E_1 and E_2 respectively.

In the following, the derivations for the amplitudes for the dark photon and ALP contributions will be described.

Dark Photon

As seen in Figure 6.1, the amplitude for the dark photon production has two contributions,

$$\mathcal{M}_1 = \frac{e\, g_X}{t - m_e^2}\ \epsilon_\mu(q_1,\lambda_\gamma)\epsilon_\nu(q_2,\lambda_X)\ \bar{v}(p_2,\lambda_{e^+})\gamma^\mu(\not{p}_1 - \not{q}_1 + m_e)\gamma^\nu u(p_1,\lambda_{e^-})\,, \quad (6.3.7)$$

$$\mathcal{M}_2 = \frac{e\, g_X}{u - m_e^2}\ \epsilon_\nu(q_1,\lambda_\gamma)\epsilon_\mu(q_2,\lambda_X)\ \bar{v}(p_2,\lambda_{e^+})\gamma^\mu(\not{p}_1 - \not{q}_2 + m_e)\gamma^\nu u(p_1,\lambda_{e^-})\,, \quad (6.3.8)$$

resulting in an amplitude given by

$$|\mathcal{M}|^2 = |\mathcal{M}_1|^2 + |\mathcal{M}_2|^2 + \mathcal{M}_1^*\mathcal{M}_2 + \mathcal{M}_1\mathcal{M}_2^*\,. \quad (6.3.9)$$

Using FeynCalc [114], the matrix amplitude squared is calculated with the momenta, spin, and polarisation vectors as described in section 2.2.4. As the dark photon is undetectable its spin will be summed over using eq. (2.2.31) for its mass m_X. The photon helicity is included in the calculations for future use in section 6.5.

The leading term $\mathcal{O}(m_e^0)$ of the final total amplitude is

$$\begin{aligned}|\mathcal{M}|^2 = -\frac{g_X^2 e^2 \csc^2\theta}{2s\,(\tau_X - 1)^2}\Bigg\{ & \\ & \beta_X^2\lambda_\gamma(2\,\lambda_{e^-} - 2\,\lambda_{e^+})\left[E_+E_-(\cos(2\theta)+3) + \left(4E_+^2 - 2s\right)\cos\theta\right] \\ & - 2(4\,\lambda_{e^-}\lambda_{e^+} - 1)\Bigg[-2\beta_X^2 E_+E_-\cot\theta + \sin\theta\left(\beta_X^2\left(E_+^2 - \frac{s}{2}\right) - s\tau_X\right) \\ & \qquad - \beta_X^2\left(2E_+^2 - s\right)\csc\theta\Bigg]\Bigg\}\,,\end{aligned} \quad (6.3.10)$$

where θ is the polar angle in the lab frame, and s, t, and u are the Mandelstam variables defined in eq. (3.2.6),

$$E_\pm = E_1 \pm E_2\,, \qquad \tau_X = m_X^2/s\,, \qquad \text{and} \qquad \beta_X^2 = 1 + \tau_X^2\,. \quad (6.3.11)$$

The photon energy E_γ has been re-written as a function of m_X, θ, and $E_{1,2}$ in order to simplify the expression.

From the amplitude, two separate expressions containing the incoming fermion helicities emerge; $(\lambda_{e^-} - \lambda_{e^+})$ and $(4\,\lambda_{e^-}\lambda_{e^+} - 1)$ which both go to zero for $\lambda_{e^+} = \lambda_{e^-}$.

Therefore, as described earlier, due to the vector interaction the helicities are required to be opposite and any dependence on the equal helicity part of the amplitude is of order $\mathcal{O}(m_e^2/s)$.

The effects of the polarisation of the incoming beams on the amplitude is investigated using the ratio given by

$$\mathcal{R}\left(P_{e^-}, P_{e^+}\right) = \frac{|\mathcal{M}|^2\left(\alpha_\gamma = 0\right)}{|\mathcal{M}|^2\left(\alpha_\gamma = P_{e^\pm} = 0\right)}\,, \tag{6.3.12}$$

where beam polarisations $P_{e^\pm}$ are defined in eq. (2.6.13) and α_γ is the degree of photon polarisation in eq. (2.6.14) . It is found, using eq. (6.3.10), that $\mathcal{R}\left(P_{e^-}, P_{e^+}\right) = (1 - P_{e^-}P_{e^+})$ at $\mathcal{O}(m_e^0)$, and the cross-section is maximally enhanced for fully oppositely polarised beams.

Axion-Like Particles

As seen in Figure 6.1, the matrix amplitude of the ALP production has two t/u-channel contributions, eq. (6.3.13) and (6.3.14), and a third s-channel contribution coming from the photon coupling, eq.(6.3.15).

$$\mathcal{M}_1 = \frac{e\,c_e m_e}{f_a\left(t - m_e^2\right)}\;\; \epsilon^*_\beta(q_1,\lambda_\gamma)\;\; \bar{v}(p_2,\lambda_{e^+})\gamma^5(\not{p}_1 - \not{q}_1 + m_e)\gamma^\beta u(p_1,\lambda_{e^-})\,, \tag{6.3.13}$$

$$\mathcal{M}_2 = \frac{e\,c_e m_e}{f_a\left(u - m_e^2\right)}\;\; \epsilon^*_\beta(q_1,\lambda_\gamma)\;\; \bar{v}(p_2,\lambda_{e^+})\gamma^\beta(\not{p}_1 - \not{q}_2 + m_e)\gamma^5 u(p_1,\lambda_{e^-})\,, \tag{6.3.14}$$

$$\mathcal{M}_3 = \frac{e\,c_\gamma}{f_a\,s} g_{\mu\nu}\;\; \epsilon^*_\beta(q_1,\lambda_\gamma)\;\; \bar{v}(p_2,\lambda_{e^+})\gamma^\mu u(p_1,\lambda_{e^-})\epsilon^{\nu\beta\rho\sigma}(p_2+p_1)_\rho(q_1)_\sigma\,. \tag{6.3.15}$$

The ALP coupling to fermions is proportional to m_e, hence its contribution will at leading order be proportional to m_e^2. The interference between the two channels is suppressed by a factor of m_e and is found to be negligible. Following the same procedure as the dark photon calculations, the amplitude is derived accounting for contributions from ALP coupling to electrons, eq. (6.3.16), ALP coupling to photons, eq. (6.3.17), and the interference between them, eq. (6.3.18).

$$|\mathcal{M}|_e^2 = \frac{m_e^2 c_e^2 e^2 \csc^2\theta}{2 f_a^2\, s(\tau_X-1)^2}\ (E_-\cos\theta + E_+)^2 \left[(\lambda_{e^-}\lambda_{e^+}+1)(1+\tau_X^2) + \lambda_\gamma(\lambda_{e^-}+\lambda_{e^+})\left(\tau_X^2-1\right)\right], \tag{6.3.16}$$

$$|\mathcal{M}|_\gamma^2 = \frac{c_\gamma^2 e^2 s(\tau_X-1)^2}{32 f_a^2 (E_-\cos\theta+E_+)^2} \left\{2\lambda_\gamma(\lambda_{e^-}-\lambda_{e^+})\left[4E_2^2\cos\theta + \left(E_+^2-\frac{s}{2}\right)(\cos\theta+1)^2\right] + (\lambda_{e^-}\lambda_{e^+}-1)\left[4E_2^2\cos\theta - \left(E_+^2-\frac{s}{2}\right)(\cos\theta+1)^2\right]\right\}, \tag{6.3.17}$$

$$|\mathcal{M}|_{\mathrm{i}}^2 = \frac{c_\gamma c_e e^2 m_e \csc\theta}{2 f_a^2\, s^2} \left\{\lambda_\gamma\left[s(\lambda_{e^-}-\lambda_{e^+})\left(E_+^2-\frac{s}{2}\right)(\cos\theta+1)^2(1-\tau_X) - \frac{1}{2}s^2(\lambda_{e^-}+\lambda_{e^+})(\tau_X+1)\sin^2(\theta)\right] - E_2^2\left[\cos(2\theta)+3\right] + s(\tau_X-1)\left[\lambda_{e^-}\lambda_{e^+}(E_-+E_+\cos\theta)^2 - (E_-\cos\theta+E_+)^2\right]\right\}. \tag{6.3.18}$$

Here the amplitudes squared are displayed with their relative leading order in the electron mass; $\mathcal{O}(m_e^0)$ for the ALP-photon coupling, $\mathcal{O}(m_e^2)$ for the ALP-electron coupling, and $\mathcal{O}(m_e^1)$ for the interference. The leading order terms for the contribution from the ALP coupling to photons require the incoming fermions to have opposite helicity, and any contributions from equal helicities are of $\mathcal{O}(m_e^2)$. Unlike the dark photon and s-channel contribution, the t/u-channel contribution from the ALP coupling to fermions requires equal beam helicities, where opposite helicities only give rise to terms $\mathcal{O}(m_e^4)$. Hence, with 100% polarised beams, where the helicity of both incoming particles is fixed, one can to leading order approximation distinguish between the two ALP couplings.

Using eq. (6.3.12) for the effect of the polarisation of the incoming beams, and the amplitudes squared eq. (6.3.16) and (6.3.17), the s-channel contribution gives

$\mathcal{R}\left(P_{e^-}, P_{e^+}\right) = (1 - P_{e^-}P_{e^+})$ at $\mathcal{O}(m_e^0)$, while the t/u-channel contribution gives rise to $\mathcal{R}\left(P_{e^-}, P_{e^+}\right) = (1 + P_{e^-}P_{e^+})$ at $\mathcal{O}(m_e^2)$, both with little to no corrections from higher orders. The full ALP amplitude squared has a more complex structure with the two main components, from each ALP coupling, having opposite polarisation dependencies. For similarly sized t/u- and s-channel cross-sections, one can control the ratio of the two channels using the beam polarisations.

The two ALP couplings have different dependencies on the ALP mass. The s-channel contribution is directly proportional to $(\tau_X - 1)^2 = (m_a^2 - s)^2$, which for $m_a^2 \ll s$ simplifies to s^2, and as m_a increases the expression tends to zero. The t/u-channel has a more complicated dependence, where for small ALP masses an overall suppression by s^{-1} emerges, and the s-channel dominates over the t/u-channel. But as the mass increases and $m_a \sim \sqrt{s}$, the expression blows up and the t/u-channel starts to dominate. For equally sized coupling constants, the ALP coupling to photons process dominates for small masses and hence the maximum enhancement of the total amplitude is found for opposite helicities, whereas the opposite becomes true for large mass.

6.3.1 Differential Cross-sections

Using the $2 \to 2$ differential cross-section in eq. (2.6.9), the differential cross-section for the production of dark photons in the centre-of-mass frame for unpolarised beams, up to corrections of order $\mathcal{O}(m_e^2/s)$, is given by

$$\frac{d\sigma}{d\Omega} = g_X^2 \frac{\alpha}{4\pi\, s} \frac{(1+\tau_X)^2 + (1-\tau_X)^2 \cos^2\theta}{(1-\tau_X)(1-\cos^2\theta)}\,, \tag{6.3.19}$$

for $\tau_X = m_X^2/s$. For the production of ALPs, the differential cross-section reads [106]

$$\begin{aligned}\frac{d\sigma}{d\Omega} = \frac{\alpha}{4\pi\, f_a^2}\Bigg[& c_e^2 \frac{m_e^2}{s} \frac{1+\tau_X^2}{(1-\tau_X)(1-\cos^2\theta)} \\ & + c_e c_\gamma \frac{m_e^2}{2s} \frac{(1-\tau_X)^2}{(1-\cos^2\theta)} + \frac{c_\gamma^2}{32}(1+\cos^2\theta)(1-\tau_X)^3\Bigg]\,,\end{aligned} \tag{6.3.20}$$

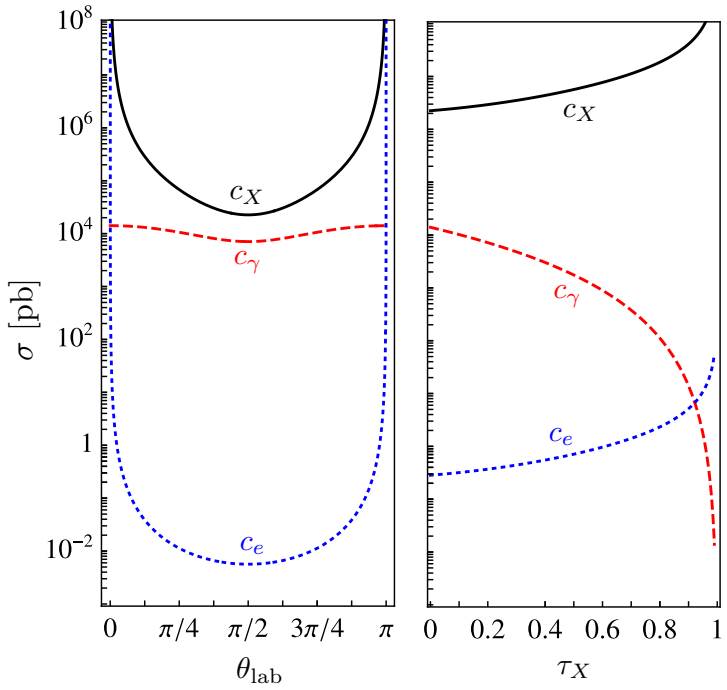

Figure 6.2: Cross-sections for the production of dark photons with $g_X = 1$ (black), ALP-photon coupling for $c_\gamma/f_a = 1/\text{GeV}$ and $c_e = 0$ (red dashed), and ALP-electron with $c_e/f_a = 1/\text{GeV}$ and $c_\gamma = 0$ (blue dotted) as a function of $\theta_{\rm lab}$ (left) and τ_X (right). Other variables are set as $s = 10\ \text{GeV}$, $\tau_X = m_X^2/s = 0$ (left), and $\theta_{\rm lab} = \frac{\pi}{4}$ (right).

up to relative corrections of order $\mathcal{O}(m_e^2/s)$. Here the first term is the contribution from the left panel of Figure 6.1 with the ALP coupling to the electron, the second is the interference term, and the last term is the contribution from the middle panel of Figure 6.1 with the ALP radiated from the photon (*ALP-strahlung*). The contribution from the ALP coupling to photon process is of order $\mathcal{O}(m_e^0)$ as the $\mathcal{O}(m_e^2/s)$ term is heavily suppressed.

The differential cross-sections are shown in the left panel of Figure 6.2. Both the dark photon and the ALP coupled to electrons are produced mostly for $|\cos(\theta_{\rm lab})| \to 1$ (the forwards and backwards directions), whereas the ALP coupled to photons has a significantly more flat distributions. The angular distribution can therefore distinguish a new particle produced in t/u-channel diagrams (ALPs coupling to electrons or dark photons) from particles produced in the s-channel (ALPs coupling to photons), though it is not enough to distinguish within these categories.

The dependence of the differential cross-sections on the mass of the invisible state m_X is shown in the right panel of Figure 6.2. As described earlier, the production of ALPs via s-channel is suppressed for large τ_X, but the production via t/u-channel is enhanced. Hence, independently of the background present, the expected signal from the s-channel contribution reduces for larger masses, decreasing the experimental sensitivity to the ALP coupling to photons. It is worth noting that the t/u-channel contributions seem to diverge for both large angles and $\tau_X \to 1$, but are regularised by the inclusion of the electron mass.

The Chiral Belle Programme, as described in section 3.3.2, is the proposal to use a polarised electron beam to collide with an unpolarised positron beam [115]. The amplitude for dark photon and ALP-strahlung production is dominated by incoming beams with opposite helicities, whereas the production of ALPs through coupling to electrons is dominated by incoming beams with equal helicities. This requires both beams to be polarised, the polarisation of one beam will not have a qualitative effect on the differential production cross-sections.

If *both* the electron and positron beams are polarised, one can distinguish the dark photon from an ALP. In the case of a dark photon, if the electrons and positrons are polarised with *equal* helicity, the signal would be suppressed by m_e^2/s with respect to the unpolarised case. In contrast, the leading term for the cross-section for ALPs produced via electron couplings remains unchanged for electron and positron beams with equal helicities. These two production channels have the same angular distribution, but with the polarisation of both beams one can significantly reduce the contribution of either channel, distinguishing them from one another. Similarly, in the context of a dark vector boson Z_d, which differs from the dark photon considered by the inclusion of an axial-vector coupling, the angular distribution of the polarised differential cross-section of $e^+e^- \to Z_d\gamma$ can be used to distinguish between the vector and axial-vector couplings [116]. The longitudinal beam polarisations are used in this thesis, but for electron and positron beams with transversal polarisation the information from the azimuthal angular distribution can be used to further

discriminate between background and signal [117–119].

6.4 Event Generation

The signature in the production of an invisible state together with a photon is a single photon recoiling against missing energy. Any search for New Physics with this signature needs to account for a number of SM processes that produce final states that are difficult to distinguish. The SM background is dominated by the process $e^+ e^- \to e^+ e^- \gamma$ in which both the electron and the positron escape the detector. Additional background final states are $e^+ e^- \gamma\gamma$, $\gamma\gamma(\gamma)$ in which one or two photons are lost, and the irreducible production of neutrinos $\nu\bar{\nu}\gamma(\gamma)$. Even though the neutrino background is significantly smaller than the other backgrounds, it has to be considered as it cannot be reduced with detector upgrades. The selection process for the signal events will be presented here, following the analysis in [100] with modifications.

6.4.1 Standard Model Background

Each SM background process has several contributions, where the corresponding Feynman diagrams are shown in Figure 6.3. Implementing minimal cuts on the lab frame energy of photons, $E_\gamma > 0.01$ GeV, and the asymmetric angular coverage $12.4^\circ \leq \theta_{\text{lab}} \leq 155.1^\circ$ of the Belle II detector [43], the fraction of the different processes contributing to the background is shown in Table 6.2.

SM process	$e^+e^-\gamma$	$e^+e^-\gamma\gamma$	$\gamma\gamma\gamma$	$\gamma\gamma$	$\bar{\nu}\nu\gamma(\gamma)$
Fraction	79.38%	10.39%	9.72%	0.51%	$< 0.01\%$

Table 6.2: Fraction of the different SM backgrounds for simulations performed with minimal cuts.

In Figure 6.4, it can be seen how the normalised differential photon energy distribution of the different background processes compares to the signal process for three

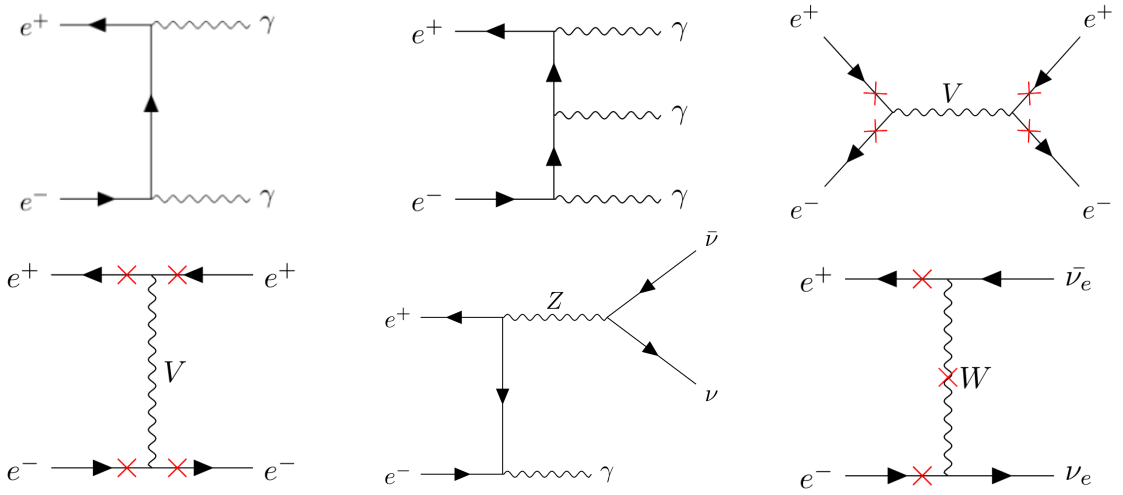

Figure 6.3: Feynman diagrams for all background processes, $e^+e^- \to \gamma\gamma(\gamma)$ (top left and middle), $e^+e^- \to e^+e^-\gamma(\gamma)$ (top right and bottom left), and $e^+e^- \to \nu\bar{\nu}(\gamma)$ (bottom middle and right), with $V \in \{\gamma, Z\}$.

different masses of the invisible state $m_X \in \{1, 6, 9\}$ GeV using the cuts described above. In the centre-of-mass frame, the energy of the photon recoiling against the invisible state is fixed by the mass of the invisible state,

$$E_{\text{CMS}} = \frac{1}{2}\frac{(s - m_X^2)}{\sqrt{s}}\,. \tag{6.4.1}$$

The signal is therefore constant in E_{CMS} where larger masses m_X correspond to lower photon energies. Notably, for the E_{CMS} observable the signals with $m_X \leq 1$ GeV are almost identical to the $e^+e^- \to \gamma\gamma$ background and therefore positioned underneath the $\gamma\gamma$ signal in the figure. The shape of the differential energy distribution is therefore independent, up to small corrections, of the spin or specific production process of the invisible state. The figure shows how cuts on the photon energy can isolate the signal, in particular for small masses m_X.

For high photon energies or small mass m_X, the background process $e^+e^- \to \gamma\gamma$ has increasing significance, whereas for low photon energies or high mass m_X the other background processes are more important. For this reason, the BaBar search for dark photons distinguishes two different mass regions, $-4 < m_X^2 < 36\,\text{GeV}^2$ and $24 < m_X^2 < 69\ \text{GeV}^2$, in which the background from $e^+e^- \to \gamma\gamma$ and $e^+\,e^- \to e^+\,e^-\,\gamma$

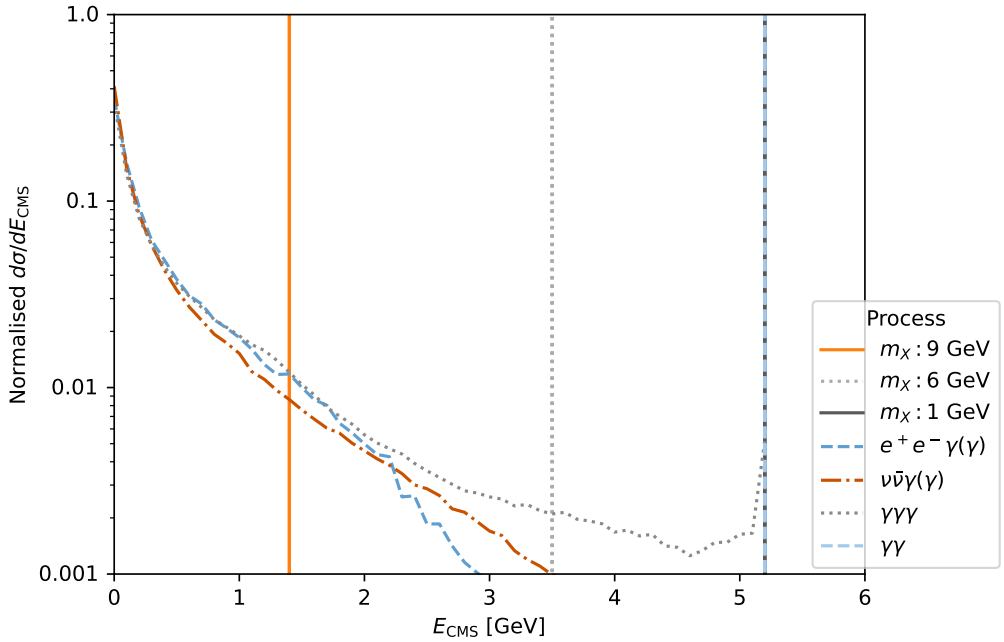

Figure 6.4: Differential cross-section for the different SM background processes and the production of a new state with $m_X \in \{1, 6, 9\}$ GeV as a function of the centre-of-mass energy of the final state photon E_{CMS}.

dominate respectively [103]. The upper limit is $m_X^2 = 63.5$ GeV^2 for the $\Upsilon(2S)$ dataset. Similarly, Belle II anticipates two different signal regions for $m_X < 6$ GeV and $m_X \in [6, 8]$ GeV [100]. In the following, the proposed cuts for these analyses from [100], which are optimised to search for dark photons, will be analysed. How the different optimisation for ALP searches, how polarised beams, or a final state photon polarisation measurement could improve the analysis, will be commented on.

Using MadGraph [36], 5×10^6 background events are simulated with a minimum transverse momentum cut applied to outgoing photons and invisible states, $p_T \geq 0.01$ GeV, and to outgoing fermions, $p_T \geq 0.1$ GeV, in order to avoid divergences.

The simulations are performed for tree-level, fixed-order QED contributions with a simplified detector setup. For example, the imperfections in the crystals in the detector and the photon conversion probability are not considered. The beam polarisation is specified within MadGraph for $0 - 100\%$ polarised beams. It is required that only one photon is within the angular acceptance of the detector, either in the end-caps or the main barrel, all other particles must be undetected.

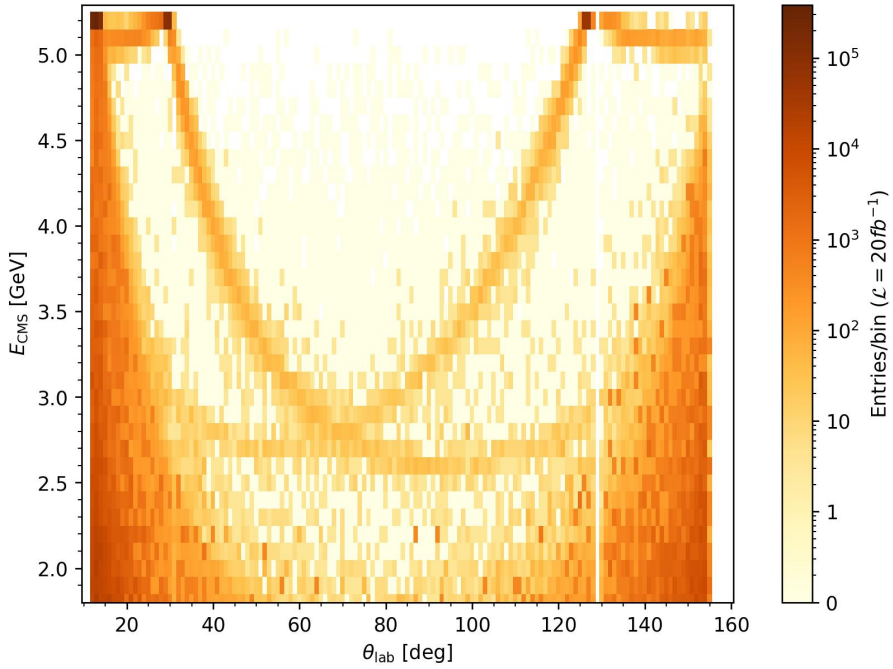

Figure 6.5: Distribution of SM background events in $\theta_{\mathrm{lab}} - E_{\mathrm{CMS}}$ plane for $e^+e^- \to \gamma + \not{E}$, see text for details.

The distribution of outgoing photons from the various SM backgrounds in the plane spanned by the scattering angle θ_{lab} and centre-of-mass energy E_{CMS} is shown in Figure 6.5.

The distributions for the different background processes are displayed in Figure 6.6, where for larger displays see Appendix E. The background from $\gamma\gamma$ final states, upper left panel of Figure 6.6, has a fixed energy due to the $2 \to 2$ scattering, but only contributes for certain angles as only one of the two photons are detected. This happens when one photon is lost in the two gaps between the endcaps and the main barrel of the detector, and for the asymmetric angular coverage of the detector where the photon is lost along the beampipe. Figure 6.7 highlights the two gaps and the difference in angular coverage $(17^\circ, 30^\circ)$ of the Belle II detector as viewed from the top. As a consequence of the asymmetric beam energies and asymmetric angular coverage, processes in which photons are lost along the beampipe in the other direction does not contribute to the background because the recoiling photon is not covered by the detector.

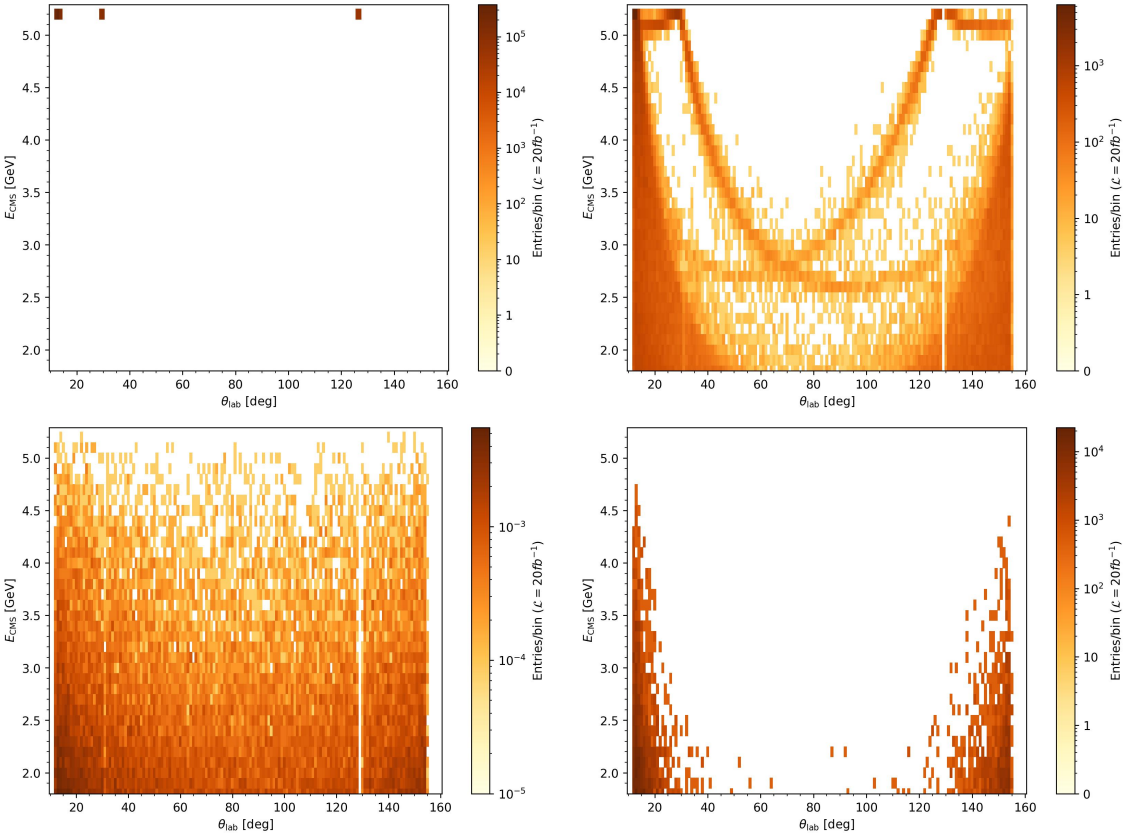

Figure 6.6: SM background distributions for $e^+e^- \to \gamma\gamma$ (upper left), $\gamma\gamma\gamma$ (upper right), $\nu\bar{\nu}\gamma(\gamma)$ (bottom left), and $e^+e^-\gamma(\gamma)$ (bottom right).

The endcap gaps are also visible in the background from $\gamma\gamma\gamma$ final states, upper right panel of Figure 6.6, where the two bands crossing the central region of the plane correspond to photons lost in either forward or backward direction. Here one of the three photons will be produced along the beam pipe whilst the other two travel transversely, one escaping detection through an endcap gap.

The background from the $e^+e^-\gamma(\gamma)$ final states, bottom left panel of Figure 6.6, is most pronounced for small angles with respect to the beampipe, and there are fewer events for angles $40^\circ \lesssim \theta_{\text{lab}} \lesssim 120^\circ$. Whereas background events from $\nu\bar{\nu}\gamma(\gamma)$ final states, bottom right panel of Figure 6.6, have an almost flat θ_{lab} distribution, but the contribution decreases for high photon energies. In all backgrounds the gap between the main barrel and endcaps are visible as straight white lines, most clearly in the neutrino final states in bottom right panel of Figure 6.6 at $\theta_{\text{lab}} \approx 130^\circ$ but also present at $\theta_{\text{lab}} \approx 30^\circ$.

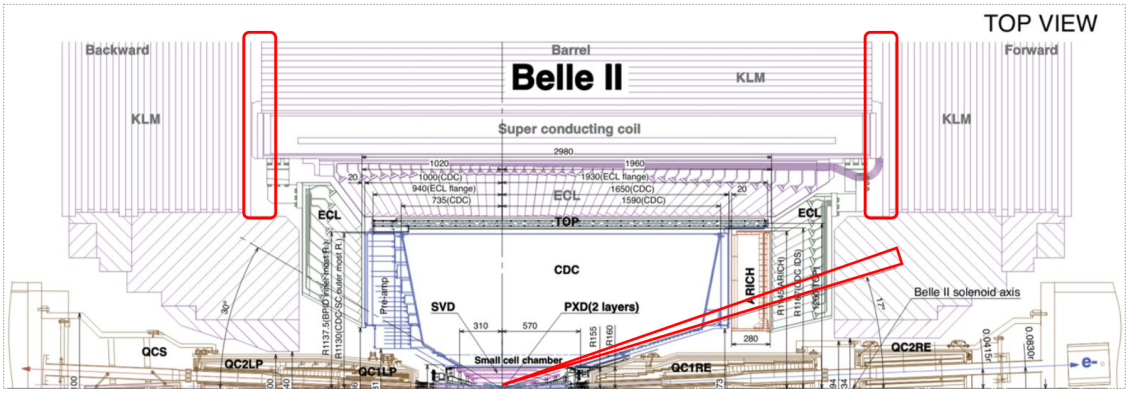

Figure 6.7: Depiction of the gaps between the barrel and end-caps and difference in angular coverage for the Belle II detector (Modified from [100]).

The background distribution found agrees with the unpublished results found in [120] where a detailed analysis of the different background processes is performed. More background events are found for large θ_{lab}, in the forward direction, than the Belle II physics book [100], which has only one $\gamma\gamma\gamma$ band going across the plot. The Belle II physics book includes higher-order QED corrections, performs a full detector analysis, and applies other cuts. The discrepancy could arise from these, or be due to detector components or deficiencies, which were not taken into consideration in the detector simulations in this thesis. For electron and positron beams polarised with equal helicities, the SM backgrounds are significantly reduced. Similarly to the dark photon process, the backgrounds from $\gamma\gamma$ and $\gamma\gamma\gamma$ final states are substantially suppressed with respect to the unpolarised case, and the remaining background is mostly peaked towards small angles with the beam axis. In the left panel of Figure 6.8, the distribution of background events for beams polarised with the same helicities is shown. Instead, for electron and positron beams polarised with opposite helicities the backgrounds, seen on the right panel of Figure 6.8, are very similar to the unpolarised case. Hence, in the following analysis the case for oppositely polarised beams will not be considered. The panels in Figure 6.8 for polarised beams have significantly fewer generated events than the unpolarised case seen in the right panel of Figure 6.5, and hence the resolutions are worse.

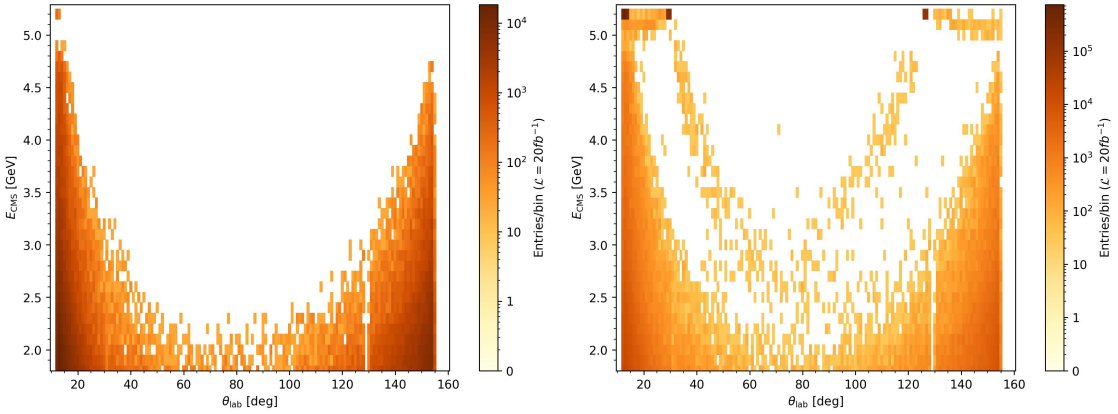

Figure 6.8: SM background for equal (left) and opposite (right) helicities polarised beams.

6.4.2 Signal

The signal processes are implemented into MadGraph using UFO models [93] based on modified Feynrules [30] models for ALPs [121] and Z' models [122–124]. As described previously and seen in Figure 6.2, the angular distribution of the signal peaks towards small and large angles with respect to the beam-line in the case of dark photons or ALPs coupled to electrons, whereas it is approximately flat for ALPs coupled to photons. In case a signal is observed, and enough statistics are available, the angular distribution can be used to distinguish these models.

For the ALP coupling to photon, it was decided to set $c_{\tilde{W}} = c_{\tilde{B}}$. As the coupling constant does not change the shape of the distribution, this can be done without loss of generality. Making this choice results in the ALP coupling to γZ going to zero, which isolate the ALP-strahlung process in simulations. The ALP couplings were fixed for three options; $c_\gamma = 1$ and $c_e = 0$, $c_\gamma = 0$ and $c_e = 1 \times 10^4$, and $c_\gamma = 1$ and $c_e = 1 \times 10^4$. For each set of values, 10^6 events were simulated where the decay constant f_a was kept as a free parameter. It is assumed that all dark photons and ALPs leave the detector before they decay, or that they decay into invisible particles, so that their decay width is considered to be zero for the remainder of this analysis. The parameters are varied within,

$$g_X \in [5 \times 10^{-6}, 1 \times 10^{-5}, 5 \times 10^{-5}, ..., 5 \times 10^{-3}] ,$$

$$f_a \in [4 \times 10^5, 2 \times 10^5, 4 \times 10^4, ..., 4 \times 10^2] \,.$$

The mass of the invisible state is varied with changing step sizes in order to increase precision; $m_X \in [1.0, 8.0]$ GeV in steps of 1 GeV with additional $m_X = 0.1, 0.5, 8.5,$ and 9.0 GeV.

For polarised beams, the signal changes as discussed in section 6.3, and if the beams have the same helicities the background is substantially suppressed. In the case of a dark photon, the signal is suppressed and very small compared to the unpolarised case. Similarly, ALPs coupled only to photons are produced with a strongly suppressed cross-section for beams with equal helicities. In contrast, the cross-section for the production of ALPs interacting with electrons is not suppressed, and one can take advantage of the lower background for polarised beams.

6.4.3 Event Selection

The searches for light new states $m_X < 6$ GeV and heavy new states $m_X \geq 6$ GeV are distinguished due to the increased background of softer photons for the heavier states. The photon trigger efficiency also varies significantly with energy [100], which will be discussed further in section 6.4.3. The Belle II angular acceptance regions are used, see section 3.3.1, and a cut is applied on the energy of the detected photon, $E_{\text{CMS}} \geq 1.8$ GeV, which restricts the mass of the invisible state. The angular coverage consists of three regions; the forward endcap $12.4^\circ < \theta < 31.4^\circ$, the main barrel $32.2^\circ < \theta < 128.7^\circ$, and the backwards endcap $130.7^\circ < \theta < 155.1^\circ$.

Energy-Dependent Cut

In a first step, an energy-dependent cut in the $\theta_{\text{lab}} - E_{\text{CMS}}$ plane is imposed, taking advantage of the correlation between energy and scattering angle for the distribution of the background events. The cut functions are generic functions fitted using an algorithm designed to minimise background events. It takes advantage of the signal

and background event distributions, maximising the signal to background ratio. In contrast to the cut functions in [59], the cuts used here reduce the background from $\gamma\gamma(\gamma)$ final states. In the following, the work carried out to perform the fits is presented.

When observing the total SM background in Figure 6.5, two prominent regions stand out; the V-shape created by the $\gamma\gamma\gamma$ final state bands, and the areas between the main $e^+e^-\gamma(\gamma)$ background and the bands. The signal for low mass invisible states falls within the first region, but for increasing masses the second region has to be considered. Two fits are therefore performed.

For the high mass fit, the points were found for each photon energy; going from small and large θ_{lab}-values respectively, finding the first bin with less than 10 events. This threshold number was chosen to represent bins with low numbers of events based on the 10^6 simulated events. A similar procedure was done for the low mass fit, this time going from the middle ($\theta_{\text{lab}} \approx 80^\circ$) for both decreasing and increasing θ_{lab}, the last bin with more events than the threshold was found.

Furthermore, the three peaks from the $\gamma\gamma$ final state were of particular interest to avoid due to their large cross-sections. This was ensured by finding the coordinates of the two centre peaks and continuing these points downwards (constant θ_{lab} and decreasing E_{CMS}) until reaching the points found as described above. As the outgoing photon in the case of large m_X has an energy around the $E_{\text{CMS}} \geq 1.8$ GeV threshold imposed, the fit was extended downwards into the area of increased background by including the range of $[60^\circ, 100^\circ]$. The points found are displayed on of the relevant distributions in Figure 6.9 for unpolarised (left panel) and equal helicity beam polarisation (right panel).

The fits of the points were found using Mathematica [125] for a generic function,

$$f(x) = c_1 + c_2\, x + c_3\, x^2 + c_4\, \sqrt{x} + c_5\, x^{-1/2} + c_6\, x^{-1} + c_7\, x^{-2}\,. \tag{6.4.2}$$

The cut functions for the unpolarised SM background are described by eqs. (6.4.3) and (6.4.4) for low and high m_X respectively. For the equal beam helicity, the

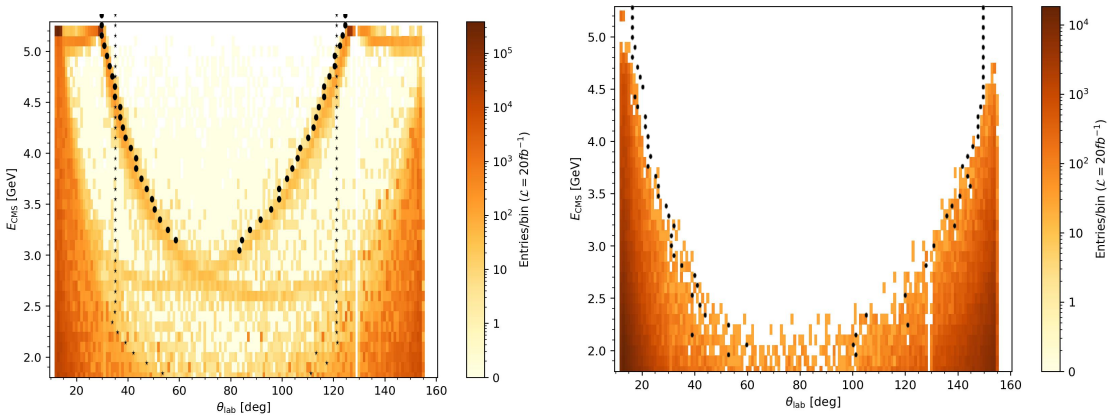

Figure 6.9: Points used for unpolarised (left) with low mass (black circles) and high mass (black stars), and equal beam polarisation (right) background.

photon-only final states were not present, and therefore this opens a big area with little to no background (only from neutrino final states). This allows for a single, much wider fit which include more signal events found in eq. (6.4.5).

$$E_{\text{CMS, low}}(\theta_{\text{lab}}) = -1.753 \times 10^4 - 61.42\,\theta_{\text{lab}} + 4.708 \times 10^{-2}\,\theta_{\text{lab}}^2 + 1.572 \times 10^3 \sqrt{\theta_{\text{lab}}} + \frac{9.795 \times 10^4}{\sqrt{\theta_{\text{lab}}}} - \frac{2.379 \times 10^5}{\theta_{\text{lab}}} + \frac{6.994 \times 10^5}{\theta_{\text{lab}}^2}, \tag{6.4.3}$$

$$E_{\text{CMS, high}}(\theta_{\text{lab}}) = -2.601 \times 10^4 - 1.109 \times 10^2\,\theta_{\text{lab}} + 0.1001\,\theta_{\text{lab}}^2 + 2.583 \times 10^3 \sqrt{\theta_{\text{lab}}} + \frac{1.304 \times 10^5}{\sqrt{\theta_{\text{lab}}}} - \frac{2.826 \times 10^5}{\theta_{\text{lab}}} + \frac{6.573 \times 10^5}{\theta_{\text{lab}}^2}, \tag{6.4.4}$$

$$E_{\text{CMS, equal}}(\theta_{\text{lab}}) = -2.929 \times 10^3 - 13.66\,\theta_{\text{lab}} + 1.293 \times 10^{-2}\,\theta_{\text{lab}}^2 + 3.061 \times 10^2 \sqrt{\theta_{\text{lab}}} + \frac{1.379 \times 10^4}{\sqrt{\theta_{\text{lab}}}} - \frac{2.763 \times 10^4}{\theta_{\text{lab}}} + \frac{5.284 \times 10^4}{\theta_{\text{lab}}^2}. \tag{6.4.5}$$

The fit functions for unpolarised beams are displayed in Figures 6.10, where the dotted black line defines the cut for light invisible states, and the dash-dotted black line defines the cut for heavy invisible states. The parameter space enclosed by these lines is the fiducial region for signal and background events. In the case of polarised beams with the same helicity, the energy-dependent θ_{lab}-cut is shown by the black line in Figure 6.11. The reduced background allows for a large fiducial region compared to the unpolarised case, so the separation for different mass regions is unnecessary.

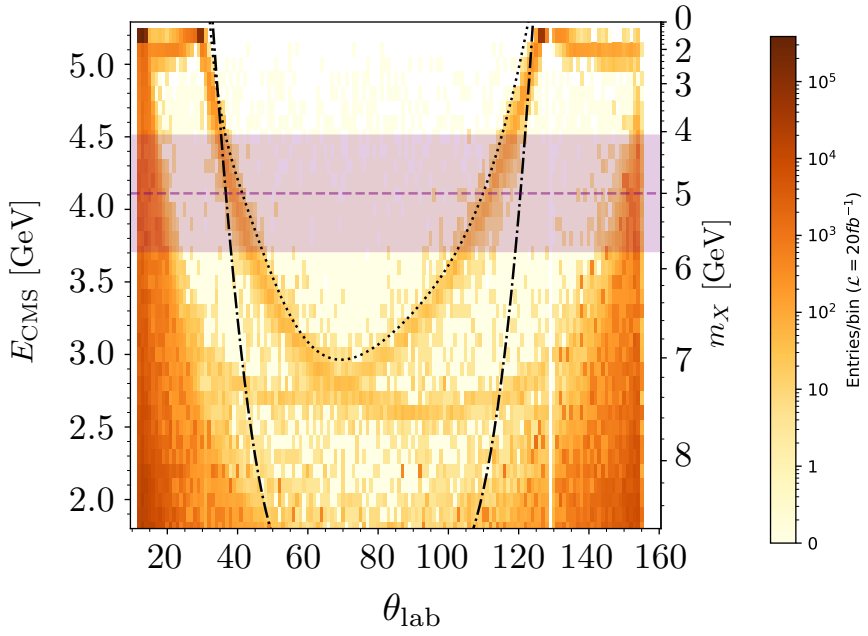

Figure 6.10: Event selection for unpolarised beams and the E_{CMS} envelope used to define cuts in the search for a 5 GeV invisible state.

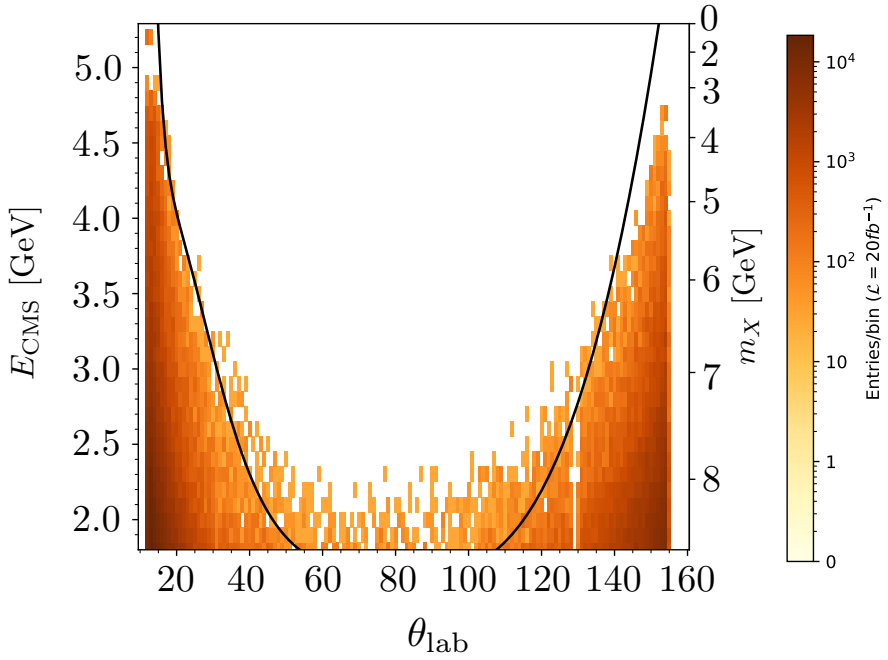

Figure 6.11: Event selection for equal helicities polarised beams.

Mass-Dependent Cut

In a second step, a mass-dependent cut on E_{CMS} is introduced. The fixed relation between the final state photon energy and the mass of the invisible state, see

eq. (6.4.1), is shown by the alternative y-axis in Figure 6.10. It allows a more targeted search, since the locations of the signal events are predicted by the invisible state mass. The inclusion of higher-order corrections causes a smearing in the final state photon energy, and hence in addition to the energy-dependent θ_{lab}-cut, the events in a window of $E_{\text{CMS}} \pm 0.4$ GeV ($\Delta E_{\text{CMS}} = 0.4$ GeV) are selected. This window is shown in Figure 6.10 for the case of $m_X = 5$ GeV.

In Figure 6.12, it can be seen that the size of ΔE_{CMS} has a considerable influence on the exclusion limit produced. Here $g_{\Delta E \to \infty}$ is the value for the critical coupling found when no mass-dependent cut is implemented and all background events inside the energy-dependent cut function are included. This is the largest value for the exclusion limit. The narrower mass-dependent windows with small ΔE_{CMS} have a smaller value and the displayed ratio increases. For $\Delta E_{\text{CMS}} = 0$ GeV, when only background events which satisfy eq. (6.4.1) are included, an improvement of up to a factor of ≈ 10 for the high mass fit is seen. As the size of the window increases with ΔE_{CMS}, the number of background events included increases and the value of the critical coupling $g_{\Delta E}$ tends to $g_{\Delta E \to \infty}$.

The presence of low statistics can be seen in the jumps between ΔE_{CMS}-values; one additional bin included can drastically change the value of the critical coupling.

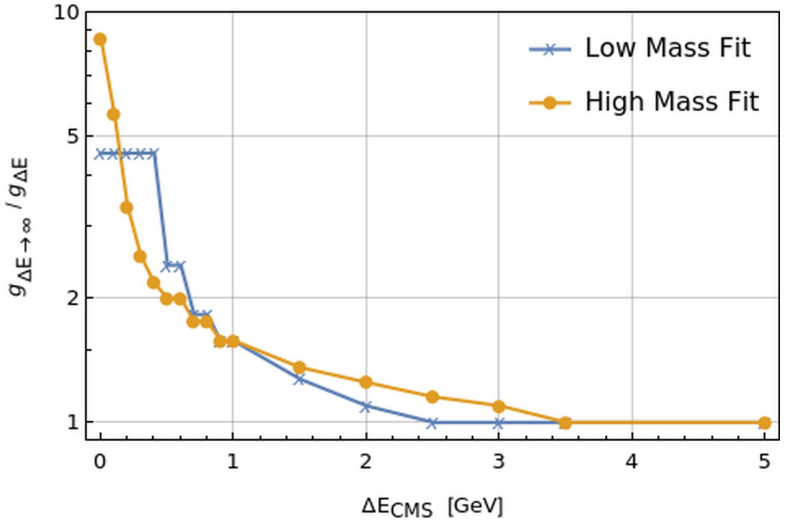

Figure 6.12: Effect of energy band size ΔE_{CMS} on the final coupling constant value g for $m_X = 1$ GeV.

The value of $\Delta E_{\text{CMS}} = 0.4$ GeV was chosen in order to avoid the significant jump in number of background events seen for the low mass fit at $\Delta E_{\text{CMS}} = 0.5$ GeV.

This mass cut window is comparable to the energy window used in [59], and a comparison to the analysis used in [100] will now be performed.

The Novosibirsk function,

$$F(x) = N\exp\left(-\frac{1}{2\sigma_0^2}\ln\left[1-\frac{x-x_p}{\sigma_R}\eta\right]-\frac{\sigma_0^2}{2}\right), \tag{6.4.6}$$

was originally found by convoluting a Compton energy spectrum with a logarithmic Gaussian function, implementing the instrumentational limitations with a resolution function [126]. The function is defined for peak value x_p, asymmetry parameter η, normalisation factor N, and $\xi = 2\sqrt{\ln 4}$. The resolution σ_R found by dividing the full-width at half-maximum (FWHM) with ξ, and

$$\sigma_0 = \frac{2}{\xi}\sinh^{-1}\left(\frac{\eta\xi}{2}\right). \tag{6.4.7}$$

The energy of the photon recoiling of the invisible state is expected to be smeared with a Novosibirsk function, and hence the invisible state mass reconstructed from the photon energy will also be smeared. The reconstructed recoil mass squared distribution at $m_X = 7$ GeV can be seen as the simulated data in Figure 6.13, where a Novosibirsk function with $x_p = 49.089$, $\sigma_R = 1.152$, $N \approx 730$, and $\eta \approx -0.5$ is fitted to the data. Here the mean x_p and spread σ_R are from Figure 208 in [100], and the corresponding mean and spread of the photon energy are $\mu_E = 2.97647$ GeV and $\sigma_E = 0.0544269$ GeV.

Figure 6.13 displays how the window used in this analysis, $E_{\text{CMS}} \in [\mu_E - 0.4, \mu_E + 0.4]$ $\Rightarrow m_X^2 \in [40.53, 57.47]$ GeV^2, captures most of the signal. The window is bigger than the one used by the Belle II collaboration, $E_{\text{CMS}} \in [\mu_E - 3\sigma_E, \mu_E + 1.5\sigma_E]$ $\Rightarrow m_X^2 \in [47.27, 52.46]$ GeV^2. By integrating over the area of the Novosibirsk function for the window used, it is found that the window captures more than 95% of the signal for the example given for $m_X = 7$ GeV. It is not expected that this result should change significantly for lighter or heavier invisible state masses.

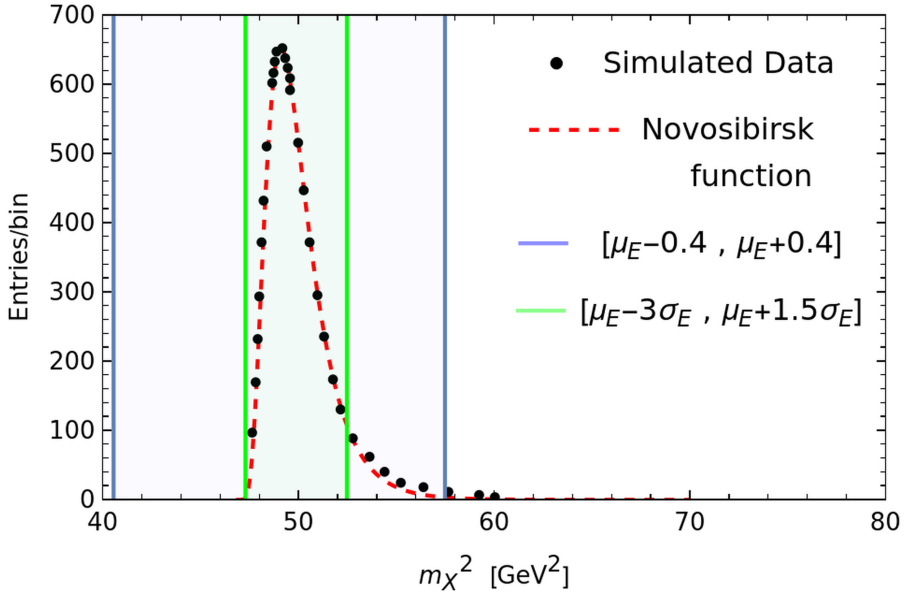

Figure 6.13: Fit of Novosibirsk function to data and energy band (green) from [100] with the energy band used in analysis (blue).

Trigger Efficiency

Using the $E_{\mathrm{CMS}} - \theta$ cut functions and the ΔE_{CMS} window described above, the number of signal and background events within the enclosed region is found. As the components of the detector are not perfect, a trigger efficiency, ϵ_s, is implemented, which is taken from Figure 206 in [100] and interpolated for different masses as shown in Figure 6.14. In the case of polarised beams, the conservative choice to use the trigger efficiency for the low-mass region is made, which is worse than the efficiency expected for the high-mass region as long as $m_X < 8$ GeV. The final sensitivity projections will later be presented in section 6.6.

6.5 Polarisation of the Final State Photon

The angular distribution together with the polarisation of the incoming beams can be used to distinguish between the dark photon, ALP coupling to photons, and ALP coupling to electron contributions. The polarisation of the beams can be used to significantly reduce the background for the ALP coupling to electrons, but leaves

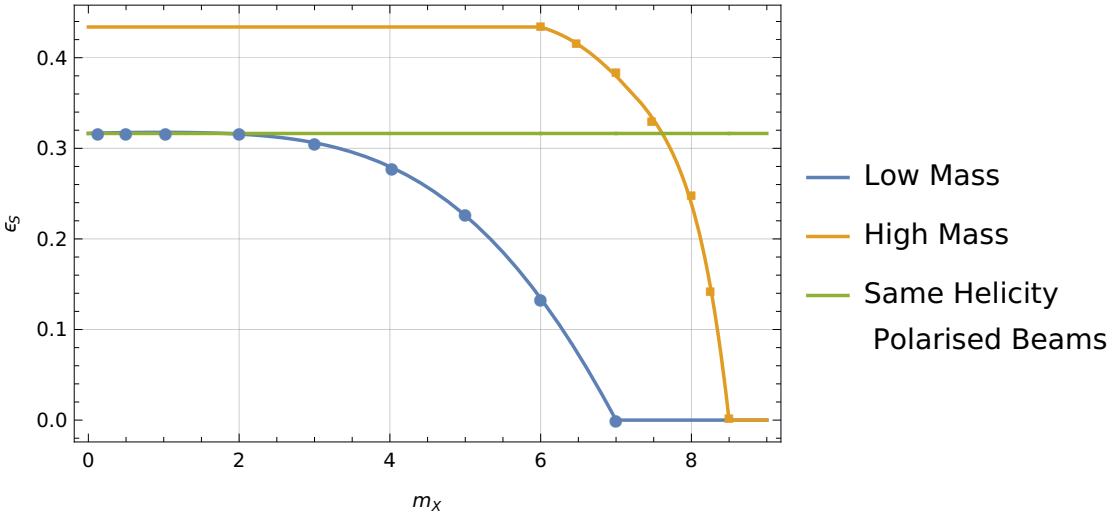

Figure 6.14: Trigger efficiency for the low- and high mass region and the fixed efficiency used for the analysis with polarised beams.

the background for the other two invisible state contributions essentially unchanged. Therefore, it will now be considered how the helicity of the outgoing photon can be used as a complementary discriminator.

Figure 6.15 displays the percentage of outgoing photons with helicity equivalent to that of the incoming electron for 100% polarised beams as a function of the angle of the photon in the lab frame θ_{lab},

$$P = \frac{|\mathcal{M}|^2(P_{e^-} = \alpha_\gamma = 1)}{|\mathcal{M}|^2(P_{e^\pm} = \alpha_\gamma = 0)}, \tag{6.5.1}$$

where $P_{e^\pm}$ is the beam polarisations defined in eq. (2.6.13) and α_γ the degree of photon polarisation in eq. (2.6.14).

As $|\mathcal{M}|^2(\alpha_\gamma = 0) = |\mathcal{M}|^2(\alpha_\gamma = 1) + |\mathcal{M}|^2(\alpha_\gamma = -1)$, at each $\cos\theta_{\text{lab}}$-value the distribution indicates that for X photons detected at this angle $P \times X$ of them will have the same helicity as the incoming electron beam, and $(P-1) \times X$ will have the opposite helicity. From now on, this distribution will be referred to as the helicity fraction distribution. The error-bars shown are calculated using,

$$P_i = \frac{N_i}{N_{\text{tot}}} \qquad \Rightarrow \qquad \delta P_i = \frac{N_i}{N_{\text{tot}}} \sqrt{\frac{1}{N_i} + \frac{1}{N_{\text{tot}}}}, \tag{6.5.2}$$

for N_i number of events for each $\cos\theta_{\text{lab}}$ and total number of events N_{tot}.

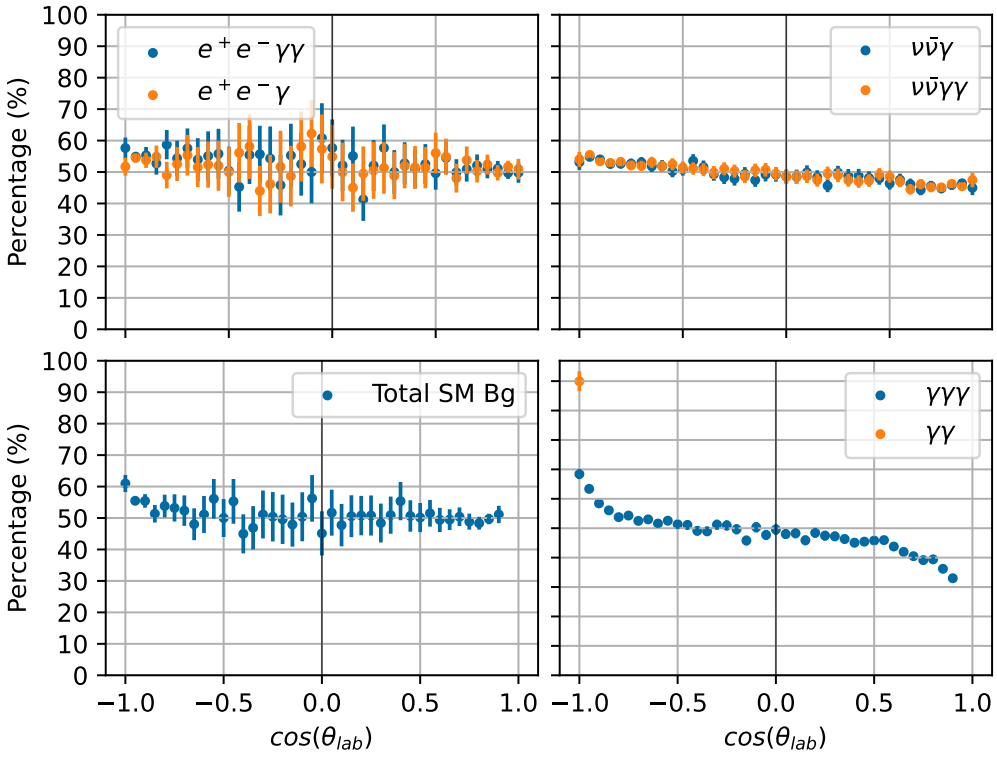

Figure 6.15: Helicity fraction distribution of the outgoing photon for SM background processes.

6.5.1 Standard Model Background

The helicity fraction distribution for the background has contributions from every SM background process, each with their own tendencies which will be described in this section. The simplest case is $e^+e^- \to \gamma\gamma$, where the incoming electron and positron must have parallel spin vectors (opposite helicities) due to the emission of two photons not changing the direction of the spin. Figure 6.16 is a 2D representation of the process with a horizontal z-axis and arbitrary vertical axis in the x-y plane. Without loss of generality, the electron is assumed to have positive helicity, and two combinations of incoming beam helicities are possible; the electron and positron spin vectors are parallel ($\lambda_{e^+} = -\lambda_{e^-}$) or antiparallel ($\lambda_{e^+} = \lambda_{e^-}$).

It can be seen that the z-components of the spin vectors of the outgoing photons will have the same sign as the incoming fermions. The direction of the photon therefore determines its helicity; if emitted in the same direction as the electron, the helicity will match that of the electron, and vice versa if emitted in the positron direction.

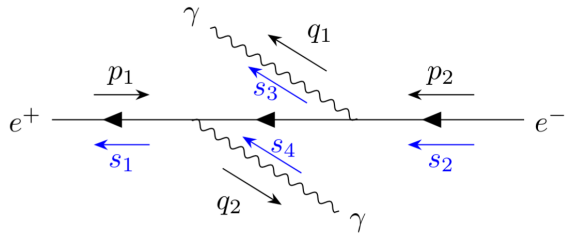

Figure 6.16: Helicity visualisation for $e^+e^- \to \gamma\gamma$

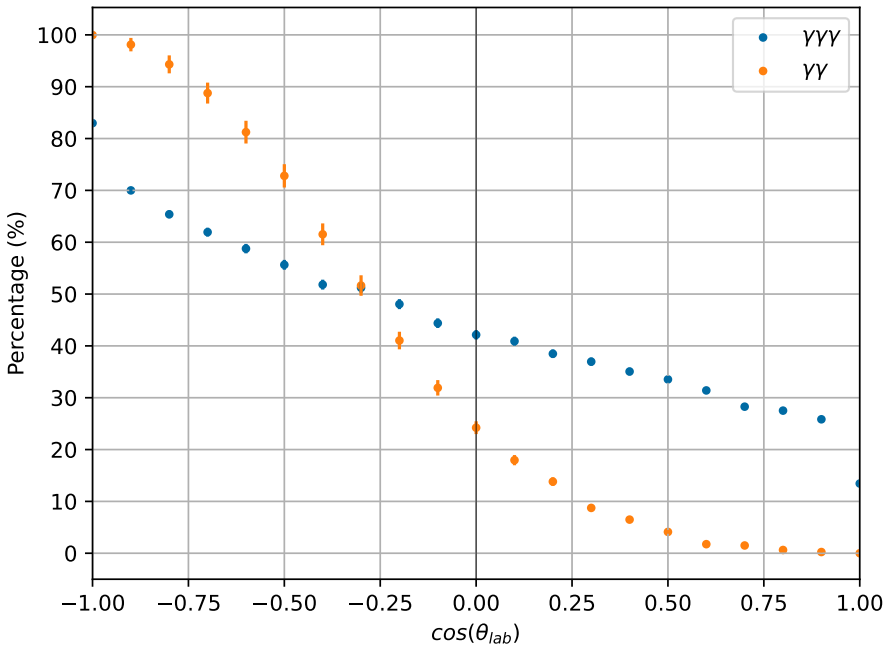

Figure 6.17: Helicity fraction distributions for $e^+e^- \to \gamma\gamma(\gamma)$ with no cuts.

Hence, the helicity fraction distribution has the s-shape seen in Figure 6.17, due to the photon being more likely to travel in the same direction as the fermion which it was emitted from. At $\cos\theta_{\text{lab}} = -1$, all photons detected will have the same helicity as the incoming electron. In the opposite direction, $\cos\theta_{\text{lab}} = +1$, none of the photons have matching helicity, as it matches that of the incoming positron. The skew away from the centre line is due to the unequal beam energies at Belle II, for equal energies the shape will be centred around $(0, 50\%)$.

The spin vector diagram in Figure 6.16, looks similar for $e^+e^- \to \gamma\gamma\gamma$. The fermions are still required to have opposite helicities, but the helicities of the outgoing photons are more random due to the 3-particle final state. Therefore, the correlation between direction and helicity fraction reduces, and the distribution is closer to 50%.

Figure 6.17 displays the helicity fraction distribution for $e^+e^- \to \gamma\gamma(\gamma)$ without any cuts applied. When implementing the criteria that only one photon can be detected, the few cases allowed for $e^+e^- \to \gamma\gamma$ are due to the asymmetric angular coverage of the detector and the gaps between the barrel and end-caps. As seen on the bottom right panel of Figure 6.15, this corresponds to the two points around $\cos\theta_{\text{lab}} \approx -1$ and another set at $\cos\theta_{\text{lab}} \approx 0.6$.

The helicities involved in the main background process, $e^+e^- \to e^+e^-\gamma(\gamma)$, are much more complex due to many contributions and interferences between them, some of which require the incoming helicities to be opposite and others equal. The resulting helicity fraction distribution, upper left panel of Figure 6.15, does not show any directional/angular dependence. Similar arguments can be made for $e^+e^- \to \nu\bar{\nu}\gamma(\gamma)$, and as seen on the upper right panel of Figure 6.15, the process has a slight $\cos\theta_{\text{lab}}$-dependence but mostly resides around 50%.

As $e^+e^- \to e^+e^-\gamma$ is the dominating process, the full background results, the bottom left panel of Figure 6.15, looks very similar. The slight upwards motion at $\cos\theta_{\text{lab}} \approx -1$ and outlying point around $\cos\theta_{\text{lab}} \approx 0.6$ are due to the large $e^+e^- \to \gamma\gamma$ contribution. It can therefore be concluded that any significant variation from 50% would indicate the presence of New Physics.

6.5.2 Dark Photon

The dark photon interacts similarly to the SM photon, and hence the incoming fermions are required to have opposite helicities. Two scenarios are possible; the photon and dark photon travel in opposite directions along the z-axis (Figure 6.16 with one γ replaced with a dark photon X), or due to the unequal beam energies they travel in the same direction (see Figure 6.18). The direction of the spin vectors involved remain the same, but as the direction of the momentum changes the photon helicity differs between the two scenarios.

For small m_X effectively only scenario one happens, resulting in the photon direction and helicity being strongly coupled; the helicity of the photon will match the helicity of the fermion travelling in the same direction. But as the dark photon mass increases, the accompanying photon becomes softer and its direction more random. This introduces occurrences of scenario two, pushing the helicity fraction distribution towards 50%. The results for the dark photon can be seen in Figure 6.19. Here the points for both the dark photon and the SM background were found from Monte Carlo simulations, the lines through the dark photons results are the analytical results found from the helicity amplitude calculations described earlier, and the SM line is the average of the SM points.

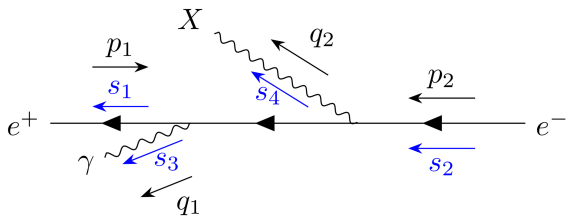

Figure 6.18: Helicity visualisation for the production of dark photons for large m_X.

6.5.3 Axion-Like Particles

As the two ALP contributions have different spin structures, they will be described separately. For ALP coupling to photons, the incoming electron-positron pair annihilate into a virtual photon which then emits an ALP. The leptons are required to have the same direction spin vector, which the virtual photon inherits. The outgoing photon helicity is determined by its direction after the ALP emission, see left panel of Figure 6.20, and depends on whether it is in the same direction as the electron or positron.

Hence, the helicity fraction distribution, seen in Figure 6.21, is the s-shape seen before. The distribution is not influenced by the mass of the ALP as it factorises out and becomes a part of the coupling constant for the process, see eq. (6.3.17) where

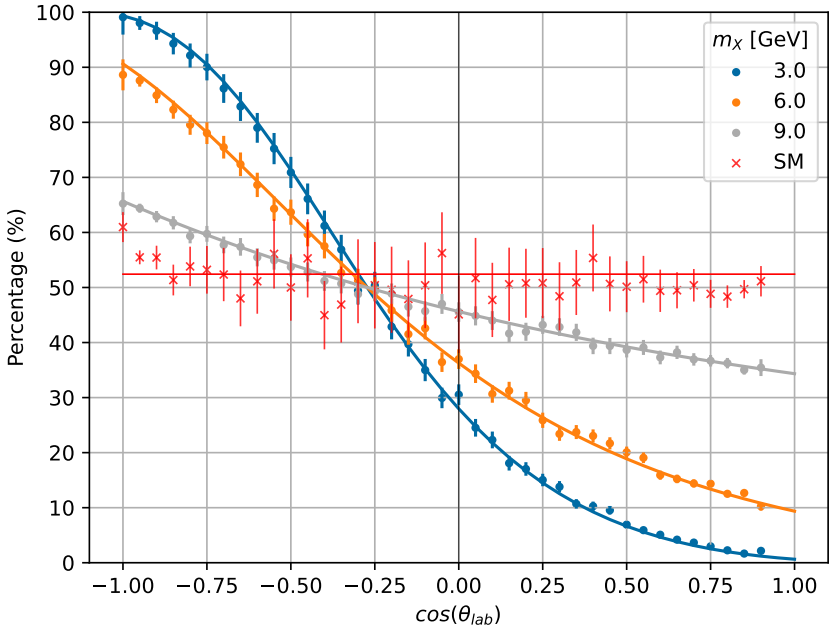

Figure 6.19: Helicity fraction distribution of the outgoing photon for dark photon for $m_X = 3, 6$, and 9 GeV as a function of the angle $\cos\theta_{\text{lab}}$.

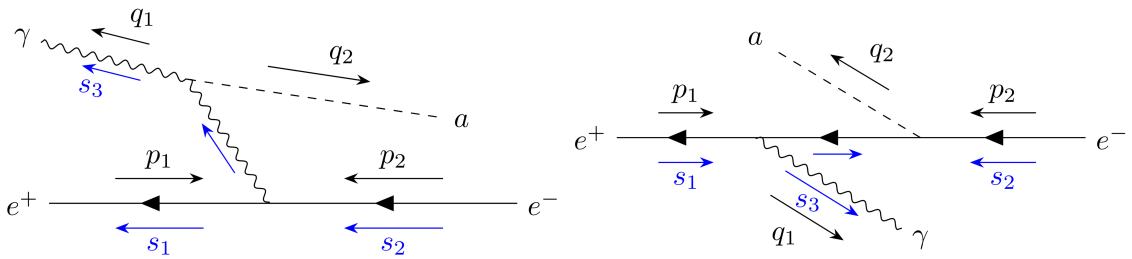

Figure 6.20: Helicity visualisation for the production of ALP-photon (left) and ALP-electrons (right) couplings.

$\tau_X = m_X^2/s$ only enters as in the first fraction. Therefore, when calculating the ratio P in eq. (6.5.1), any dependence on the ALP mass disappears. The s-shape helicity distribution is substantially different to the constant Standard Model background, and can therefore be used to distinguish the signal and provide improved exclusion limits. This will not be carried this out due to the unknown detector setup needed to measure the helicity of the outgoing photon.

The ALP coupling to electrons consists of t/u-channel diagrams like the dark photon, but as the interaction introduces a helicity flip for the incoming fermions (right panel of Figure 6.20), their helicities are equal. Therefore, the photon helicity will match both fermions or neither, resulting in no angular dependence as seen in Figure 6.22.

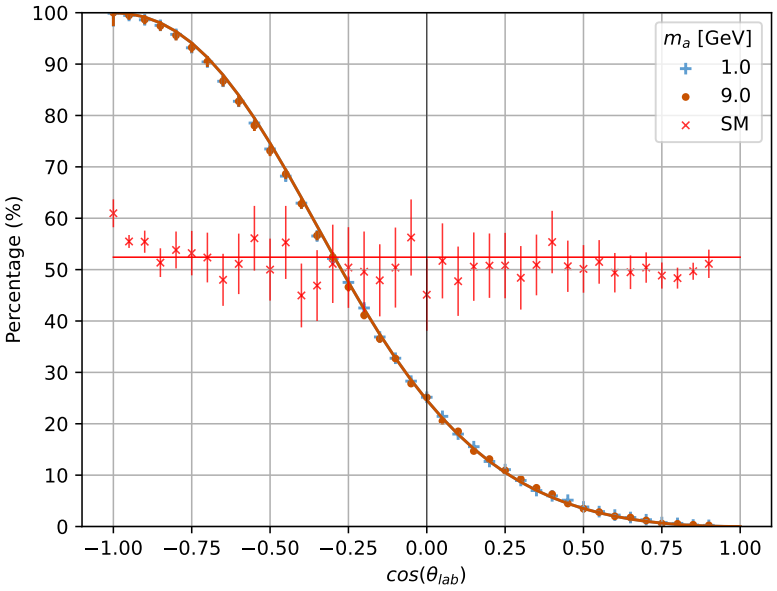

Figure 6.21: Helicity fraction distributions of the outgoing photon for ALP-photon coupling for $m_X = 3, 6$, and 9 GeV.

For small m_a, the photon helicity always matches the incoming fermions, resulting in a constant percentage of 100%. But as described before for the dark photon, as the ALP mass increases the photon direction becomes more random, resulting in the helicity fraction approaching 50%. The ALP coupling to electrons will cause a shift in the distribution, and hence it can easily be distinguished from the other to dark matter contributions, but would be difficult to separate from the background.

6.5.4 Degree of Photon Polarisation

Using the helicity fraction distributions discussed above, the overall degree of photon polarisation $\mathcal{A}_\gamma$ can be determined by integrating over the polar angle θ,

$$\mathcal{A}_\gamma = \int_{\theta_1}^{\theta_2} \alpha_\gamma \, d\theta \,, \tag{6.5.3}$$

for angles $\theta_{1,2}$, which for example can be the angular coverage of the detector. In addition to the beam polarisation, the polarisation of the final state photon can be used to determine the Dirac structure in the production amplitude. This has been successfully used to examine the chiral structure of the operator responsible for $b \to s\gamma$ transitions at LHCb [127]. Measuring the final state photon polarisation

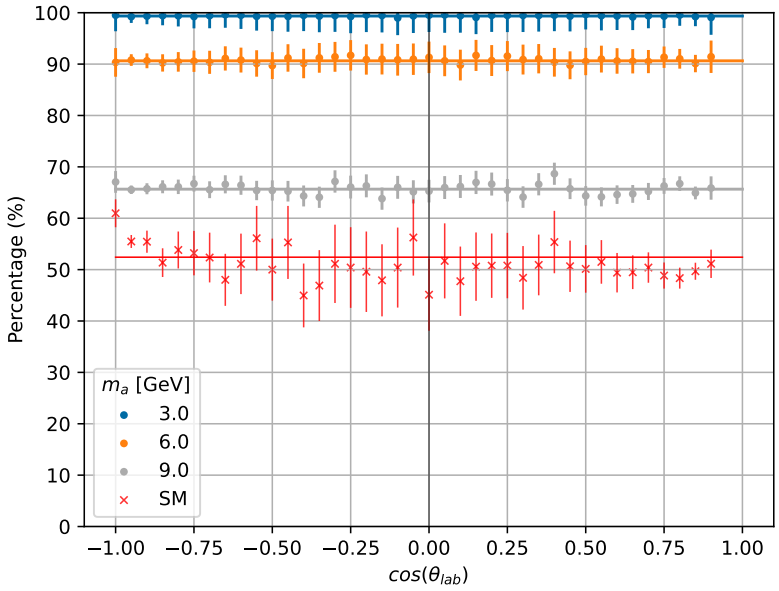

Figure 6.22: Helicity fraction distributions of the outgoing photon for ALP-electrons coupling for $m_X = 3, 6$, and 9 GeV.

is extremely challenging, but if possible it could provide an additional handle on the spin of the dark matter state. The degree of photon polarisation is defined in eq. (2.6.14) and is the ratio of the two polarisation states.

For the Standard Model background, $\mathcal{A}_\gamma = 0.5$ is expected for random photon polarisation. If only one beam is polarised, all invisible state contributions will have the same degree of photon polarisation as the background, but this result can be significantly changed when polarising both beams.

At order $\mathcal{O}(m_e^0)$, the degree of photon polarisation for the dark photon is found to be,

$$\alpha_\gamma = \frac{\left(P_{e^-} - P_{e^+}\right)}{\left(P_{e^-}P_{e^+} - 1\right)} f\left(E_1, E_2, m_X, \theta_{\text{lab}}\right) , \tag{6.5.4}$$

where the largest α_γ-value is found for small m_X and fully oppositely polarised beams. As seen in the helicity fraction distributions for the dark photon, Figure 6.19, it is possible to affect the photon polarisation by applying angular cuts in the forwards or backwards directions with $|\mathcal{A}_\gamma| \geq 0.8$ for $m_X \leq 4$ GeV.

For the ALP coupling to photons the degree of photon polarisation is

$$\alpha_\gamma = \frac{\left(P_{e^-} - P_{e^+}\right)}{\left(P_{e^-}P_{e^+} - 1\right)} f\left(E_1, E_2, \theta_{\text{lab}}\right) , \tag{6.5.5}$$

which, unlike the case of the dark photon expression, does not dependent on the ALP mass as implied by the helicity fraction distribution. Values of $|\mathcal{A}_\gamma| \approx +1$ are achieved for all m_a when applying a forward angular cut ($10^\circ \leq \theta_{\text{lab}} \leq 50^\circ$). For the ALP coupling to electrons,

$$\alpha_\gamma = \frac{\left(P_{e^-} + P_{e^+}\right)\left(s^2 - m_a^4\right)}{\left(P_{e^-}P_{e^+} + 1\right)\left(m_a^4 + s^2\right)} , \tag{6.5.6}$$

it can be seen that the degree of photon polarisation is independent of the angle of the outgoing photon, θ_{lab}. The maximum magnitude is found for small m_a and fully polarised beams, and $|\mathcal{A}_\gamma| \approx +1$ for $m_a \leq 2$ GeV with no angular cuts applied.

6.6 Sensitivity to New Physics

In the following, the sensitivity reach of Belle II for dark photons and ALPs interacting with photons or electrons for unpolarised and polarised beams is discussed. It is assumed that the new invisible states are stable on collider scales, by for example decaying into a wider dark sector. The expected 90% CL upper limit on the observed number of signal events (μ_S) is obtained by demanding that the Poisson probability of observing no more than the number of background events (μ_B), if $\mu_B + \mu_S$ events are expected is $P(\mu_B, \mu_S + \mu_B) > 0.1$ as in [100].

As described in section 4.3.1, the needed number of signal events is given by

$$\mu_S = Q^{-1}\left(N + 1, F[N, \mu_B + \mu_S]\right) - \mu_B , \tag{6.6.1}$$

Here N is the integer closest to μ_B, and μ_B is the number of SM background events found within both the $\theta_{\text{lab}} - E_{\text{CMS}}$ cut and the energy window around the dark matter signal for $\Delta E_{\text{CMS}} = 0.4$ GeV. The function *scipy.special.gammainccinv*(a, y) from the Python Scipy Module, which is the inverse of the regularised upper incomplete

gamma function, is used. The sensitivity projections are found for

$$g_{crit} = \sqrt{\frac{\sigma_{crit}}{\sigma_i}} g_i = \sqrt{\frac{\mu_S}{\epsilon_S * \mathcal{L} * \sigma_i}} g_i \,. \tag{6.6.2}$$

where the signal efficiency (ϵ_S) is taken from Figure 6.14, σ_i is the cross-section for a given mass m_X and coupling constant g_i.

Figure 6.23 shows the sensitivity reach of Belle II for the dark photon (left) and ALP-photon coupling (right) for $\mathcal{L} = 20$ fb^{-1} (orange line) and $\mathcal{L} = 50$ ab^{-1} (dashed orange line) and unpolarised beams. It is worth nothing that the projected sensitivity for masses $m_X < 2$ GeV at 50 ab^{-1} can only be achieved if backgrounds from cosmic rays are fully understood [107].

For comparison, the limits from a search for dark photons by BaBar [108], limits from beam-dumps experiments E787, E949 [128–131] and NA64 [132], are shown. The right panel shows BaBar limits on ALPs from single-photon decays of $\Upsilon(1)$ [103] and mono-photon searches by LEP [133,134], taken from [105], as well as constraints from the supernova SN1987A [135,136].

Similar colour-coding is used for the ALP coupling to electrons, where the improved sensitivity using polarised beams is shown by the red line in Figure 6.24. The bounds shown are from the neutrinoless double-beta decay experiment Gerda [137], the

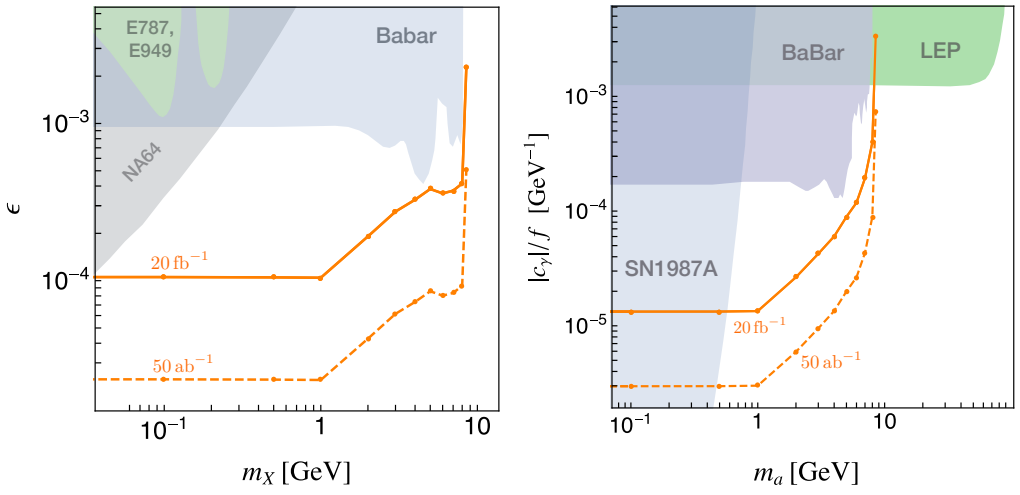

Figure 6.23: Belle II sensitivity to dark photons (left), ALPs coupling to photons (right). Details are in the text.

helioscope Edelweiss [138] taken from [139], together with the bounds by NA64 [140], BaBar [108] and LEP [134], taken from [106]. Note that the bounds from Edelweiss and Gerda require the ALP to be stable on astrophysical scales and therefore only constrain $m_a < 2m_e$.

The projected sensitivity reach exceeds the existing constraints for all three models by at least about an order of magnitude. In all models the sensitivity drops with larger mass m_X for which backgrounds are larger. In the case of ALP-strahlung, this drop is particularly steep because the cross-section drops for large masses as shown in the right panel of Figure 6.2. The slight improvement of sensitivity for masses $m_X > 6$ GeV is a consequence of the better trigger sensitivity.

The results can be compared with previous analyses of the sensitivity reach of Belle II. In general, the analysis presented here largely follows [100], that also sets constraints on an invisible spin 1 state. The main differences being that different $\theta_{\text{lab}} - E_{\text{CMS}}$ cut functions are implemented, and a constant mass-dependent window as opposed to previous estimates in [100] that consider higher-order effects and a more sophisticated detector simulation. As a consequence of this and the simplified

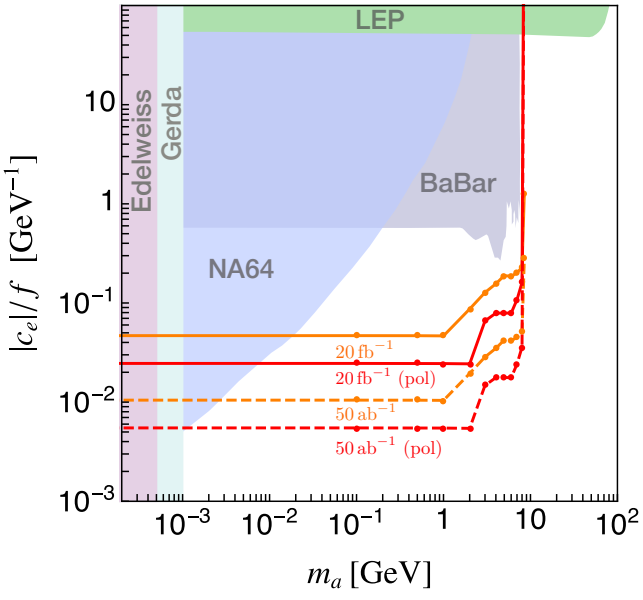

Figure 6.24: Belle II sensitivity to ALPs coupling to electrons. Details are in the text.

detector geometry used, the projections obtained in this section are roughly a factor three better. An analysis that translates the projection for the case of ALPs produced in ALP-strahlung can be found in [105, 106]. The improvement with the method used is again roughly a factor three in the projected sensitivity, consistent with the dark photon case. A recast for ALPs interacting with electrons has been performed in [106], and it is found again that the projections are roughly 3–4 times better using the improved cuts.

If a signal is observed at Belle II, it is possible in principle to determine whether the invisible state is a vector boson (g_X), an ALP interacting with photons (c_γ), or an ALP interacting with electrons (c_e). The angular distribution of the signal events can distinguish between c_γ and $\{c_e, g_X\}$, whereas the beam polarisation suppresses the signal for $\{g_X, c_\gamma\}$ and does not affect the signal for c_e.

6.7 Outlook

The results presented above assumed the incoming beams of the SuperKEKB collider to acquire 100% polarisation. Currently, the Chiral Belle Programme expects to be able to achieve 70% polarisation for the electron beam only. Hence, a study of the degree of beam polarisation needed to separate the invisible signals is vital. For example, would 70% polarisation of both beams lead to statistically significant suppression of the invisible state signals such that they can be distinguished? The improvement of the ALP-fermion coupling projection is due to the decrease in the Standard Model background processes, but the correlation between the degree of beam polarisation and reduction in background has yet to be studied.

The novel method of exploiting the beam polarisation can be implemented at other particle colliders, though most have unpolarised incoming beams. Two examples of colliders with one polarised beam are the *Hadron–Electron Ring Accelerator* (HERA) and the *Relativistic Heavy Ion Collider* (RHIC). HERA operated between 1992 and 2005 with $\sqrt{s} \approx 320$ GeV with electron-proton collisions and polarised electrons up

to 60%. RHIC is located at Brookhaven National Laboratory (BNL) and collides heavy-ions with protons polarised up to 55% [34].

A future collider to consider is the electron-ion collider (EIC) which is currently under development at BNL. It will have both the electron and nucleon beam polarised up to 70% with centre-of-mass energies of up to 100 GeV. The reasoning for the polarisation of both beams, is the determination of polarised PDFs; how the quarks and gluons are distributed inside the nucleon depending on their spins [141]. In order to fully exploit the EIC, one should consider the possibility to distinguish the signals from invisible states and improve their sensitivity projections. Going from electron-positron to electron-ion collisions would result in a significantly less clean environment, the mono-photon signal considered earlier would not be possible due to the composite nature of the ions. But other signals can be explored.

6.8 Conclusions

Measurement strategies were proposed, that can be used at electron positron colliders to determine the spin, mass, and production mechanism of an invisible state produced in association with a photon $e^+e^- \to \gamma + X$. In particular, dark photons and ALPs that interact with electrons or photons can be distinguished even in the absence of detecting any of their decay products.

The angular distribution of the final state photon is sensitive to the production mechanism and can distinguish s-channel production as in the case of ALP-strahlung from t/u-channel production, e.g. of a dark photon or an ALP produced from interactions with electrons and positrons directly. If both the electron and positron beams can be polarised with equal helicities, the dark photon cross-section is strongly suppressed with respect to the unpolarised cross-section, and only the cross-section for ALPs interacting with electrons remains unchanged. In combination, the angular distribution and the beam polarisation can distinguish between these three models. Further, the dependence of the polarisation of the final state photon on the polar

angle can be used to discriminate between the different models as well as the SM background, if it can be reconstructed with future detectors. For beams with opposite helicities and small masses m_X, both the dark photon and ALP coupling to photons helicity fraction distributions are significantly different from the SM background. While beams with equal helicities can be used to reduce backgrounds for ALPs interacting with electrons, the sensitivity for both ALPs interacting with photons as well as dark photons can be increased if final state photon polarisation can be measured.

The SM background is also significantly reduced if both the electron and positron beams are polarised. A careful analysis of different SM background processes shows that a combination of a universal cut in the plane spanned by the scattering angle θ_{lab} and centre of mass energy E_{CMS} together with a mass-dependent cut could improve the projections for searches at Belle II, assuming the method described in this chapter accounts for smearing effect from higher-order QED. If a run with polarised beams can be performed the sensitivity to ALPs interacting with electrons is further improved by a factor two. The projections are compared with constraints from other experiments and astrophysics, and the parameter space that can be probed at Belle II using the proposed measurement strategy is identified.

Chapter 7

Conclusion

Dark matter has been found to constitute a large proportion of the matter in the university, its nature is still very unknown. Many experiments have been constructed in the search for answers, looking to test the current best theory of visible matter, the Standard Model, in order to find inconsistencies. In the hunt for New Physics, scientists have a responsibility to consider the impact of these experiments. Therefore, making the most out of already existing experiments is an important endeavour. This thesis presented two methods of extending the reach of current dark matter searches at colliders; building a new detector in association with an already existing ones, and a method for using the polarisation of the incoming beams.

In Chapters 2, 3, and 4, the foundations for the remaining chapters were set-out. At first, the Standard Model describing the currently known particles and their interactions, where in particular the Higgs mechanism and Glashow-Weinberg-Salam theory were introduced. It is known that the SM is not final as there are several key components missing. Neutrinos oscillate and therefore have masses, the existence of dark matter, and many others are not contained in the SM.

Next, chapter 3 presented the concept of particle colliders, focusing on circular colliders and their detectors. The Belle II detector at SuperKEKB and the ATLAS detector at LHC were of special interest due to their relevance for the remaining chapters. The layout and purpose of the components of each detector is described,

together with how groupings of particles are detected depending on their interactions and properties. The Chiral Belle II programme, which include the polarisation of one of the incoming beams leaving the other unpolarised, is described. This provided the inspiration for the methods presented in Chapter 6. Dark particles leave collider detectors without detection if they are long-lived or invisible states acting as portals to a wider dark sector. Therefore, many types of searches for New Physics have been developed in order to study these at detectors, the main categories of these were outlined.

The detectors are limited to detect particles within their volume, and thus by building new detectors further away from the interaction point of existing detectors, one can extend their reach. One of these proposals is introduced in Chapter 5; the ANUBIS detector.

Both extensions considered in this thesis concern themselves with dark matter; long-lived dark particles with small masses and couplings to the SM, and invisible states which are portals or mediator particles interacting with both the SM and a wider dark sector. Other theories for dark matter are mentioned in Chapter 4. The specific models of dark photons, axion-like particles, and heavy neutral leptons are presented, describing their underlying theories, mechanisms, and interactions with the particles in the Standard Model. The decay modes of the particles are of interest when considering LLPs, and hence, particularly for HNLs, the possible decay channels and their widths are described.

The general approaches for detecting dark matter, collider, indirect, and direct detection, are covered and lead to a characterisation of the different searches and considerations one has to make, when studying dark matter in a collider. The statistical methods are presented, these are used for making exclusion limits and sensitivity projections for experiments when no evidence of New Physics is found.

The ANUBIS detector is a far detector located above the ATLAS detector with the purpose of detecting long-lived particles, which leave ATLAS without detection. For the proposal and during construction of new detectors, it is important to determine their sensitivity. For ANUBIS, the sensitivity studies currently consist of the development of the software SET-ANUBIS. Each module of the software is described in detail, including the reasoning for the decisions made, and how it is intended to allow anyone to produce projections for any LLP model. Most LLP studies considers one dominating or all visible decay modes of LLPs. With this in mind, the software is separated into segments such that as few generalisations as possible are made, allowing for the study of individual production and decay modes of the LLP, and the possibility of a wider dark sector to be present.

Finally, a new method which makes use of the two polarised beams at Belle II is presented. In $e^+e^- \to \gamma + X$ processes, the signals from invisible dark photons and ALPs are currently indistinguishable. The angular distributions from the two models' t/u-channel contributions from the coupling to electrons are the same, though the s-channel contribution from the ALP coupling to photons, not present for dark photon, is different. As there is no theoretical motivation for only one of the two ALP couplings to be non-zero, the final ALP contribution will be a mixture of the two.

The dependence on the helicity of the incoming leptons of each contribution was examined. It was found that the dark photon coupling to electron and ALP-photon coupling require the helicities to be opposite, whereas the ALP coupling to electrons requires equal. Hence, it is concluded that with both incoming beams polarised, each ALP coupling can be isolated, to leading order approximation. Combining the angular distributions and the polarised beams, the signals from the three couplings are separated. It was shown how the background for beams with equal helicity is significantly reduced, allowing for a significant improvement on the sensitivity to the ALP coupling to fermions.

Additionally, the opportunities that the measurement of the outgoing photon helicity

offer are explored. It was found that the helicity fraction distributions for the dark photon and ALP coupling to photons have a distinctly different shape to the Standard Model background. Therefore, if it were one day possible to measure, the photon helicity can provide an increased sensitivity to the aforementioned couplings.

The two approaches presented offers low-cost methods for extending the reach of detectors. Thus expanding the searches for New Physics whilst limiting the wider environmental impact.

Appendix A

Dark Scalar Model

A.1 Lagrangian

A minimal dark scalar portal model that is utilised in chapter 5 is presented here. The Lagrangian for a dark scalar that interacts with the Higgs boson is given by

$$\mathcal{L} = \mathcal{L}_{\text{SM}} + \mathcal{L}_{\text{DS}} - \left(\mu_S S + \lambda_S S^2\right) H^\dagger H \,, \tag{A.1.1}$$

for Higgs field $H = (v_H + h)/\sqrt{2}$ with vev v_H, and S a dark scalar field with zero vacuum expectation value. The potential is defined as

$$V(S,h) = -\frac{1}{4}\left(h + v_H\right)^2 \left[\lambda_H (h + v_H)^2 - 2\mu_H^2 + 2\,S\left(\lambda_S S + \mu_S\right)\right] ,$$

for λ_H and μ_H the parameters in the SM Higgs potential defined as in section 2.3. The vacuum expectation value for the h field, $v_H^2 = \mu_H^2/\lambda_H$, is found from the potential, and is used to define the masses of the fields, m_H and m_S,

$$V(S,h) \supset \frac{1}{2}\left(-3v_H^2\lambda_H + \mu_H^2\right) h^2 = -\frac{m_H^2}{2} h^2 \qquad \Rightarrow \qquad \lambda_H = \frac{m_H^2}{2v_H^2} \,, \tag{A.1.2}$$

$$V(S,h) \supset -\frac{1}{2} v_H^2 \lambda_S S^2 = -\frac{m_S^2}{2} S^2 \qquad \Rightarrow \qquad \lambda_S = \frac{m_S^2}{v_H^2} \,. \tag{A.1.3}$$

The resulting mass matrix,

$$\mathcal{M}^2 = \begin{pmatrix} m_H^2 & \frac{1}{2}v_H\mu_S \\ \frac{1}{2}v_H\mu_S & m_S^2 \end{pmatrix}, \tag{A.1.4}$$

is diagonalised through the following field re-definitions

$$h_{\rm SM} = h\cos\theta - S\sin\theta \qquad \text{and} \qquad \phi = -h\sin\theta + S\cos\theta\,. \tag{A.1.5}$$

Here $\text{diag}\left(m_{h_{\rm SM}}^2, m_\phi^2\right) = R(\theta)\mathcal{M}^2R(\theta)^T$ and

$$R(\theta) = \begin{pmatrix} \cos\theta & \sin\theta \\ -\sin\theta & \cos\theta \end{pmatrix}. \tag{A.1.6}$$

From this the mixing angle θ is found to be

$$\theta \approx \tan 2\theta = \frac{2\tan\theta}{1-\tan\theta} = \frac{v_H\mu_S}{m_H^2 - m_S^2}\,, \tag{A.1.7}$$

found using the elements of R. The masses of the mass eigenstates are

$$m_{h_{\rm SM}} = \frac{1}{2}\left(m_H^2 + m_S^2 - \sqrt{\left(m_H^2 - m_S^2\right)^2 + v_H^2\mu_S^2}\right), \tag{A.1.8}$$

$$m_\phi = \frac{1}{2}\left(m_H^2 + m_S^2 + \sqrt{\left(m_H^2 - m_S^2\right)^2 + v_H^2\mu_S^2}\right). \tag{A.1.9}$$

Therefore, it can be seen, that the new dark scalar mixes with the SM Higgs. From this mixing, the dark scalar has Yukawa-like couplings to SM fermions proportional to the mixing angle $\theta S \times \sum_{\rm SM}\mathcal{O}_h$, where $\mathcal{O}_h$ is the Higgs current to the other SM particles. For further detail see [7, 142, 143].

A.2 Current Limits & Projections

The current exclusion limits and projections can be seen in Figure A.1 for the mixing angle θ as a function of the dark scalar mass where $\lambda = 0$. The colour-coding is the same as the one seen for dark photons in Figure 4.9 in section 4.2.2. The parameter space looks rather restricted, but there are no limits set for $\sin\theta < 10^{-1}$

for masses above 5 GeV, and hence this entire parameter space is yet to be explored. Similarly, for dark scalar masses above 10^{-1} GeV limits and projections do not reach sensitivities lower than $\sin\theta \approx 10^{-6}$.

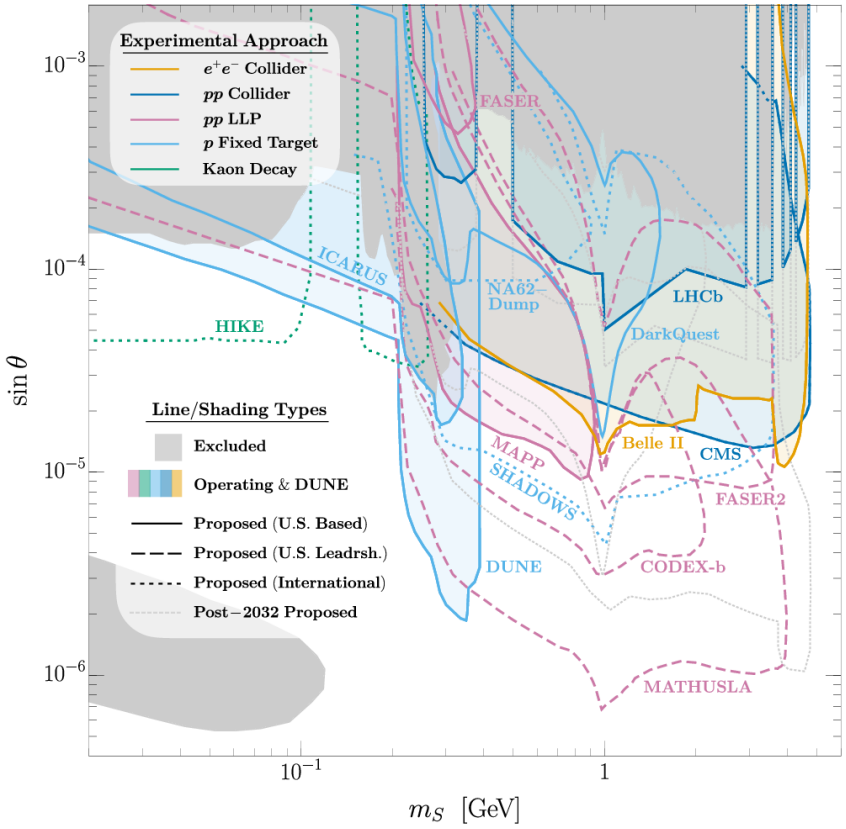

Figure A.1: Current limits and projections on minimal dark scalar with mixing angle θ and $\lambda = 0$ [78].

Appendix B

Heavy Neutral Lepton Decay Width Formulas

In the following, the widths for heavy neutral lepton decays will be presented. At first, the low energy effective field theory used throughout will be introduced.

B.1 Low Energy Effective Field Theory

For low energy processes, where the momentum of particles is much smaller than their masses, $p \ll M$, the heavy mediator boson propagator can be Taylor expanded,

$$\frac{1}{p^2 - M^2} \approx -\frac{1}{M^2} + \frac{p^2}{M^4} + \mathcal{O}\left(\frac{p^4}{M^6}\right) , \tag{B.1.1}$$

where only the first term is not heavily suppressed [144].

The terms in the Standard Model Lagrangian, with the addition of a heavy neutral lepton N, containing the $W^{\pm}$ bosons are given by

$$\begin{aligned} \mathcal{L} \supset m_W^2 W_\mu^+ W^{\mu-} + \frac{g}{\sqrt{2}} \left(W_\mu^+ J_W^{\mu+} + W_\mu^- J_W^{\mu-} \right) \\ - \frac{g}{\sqrt{2}} U_\alpha^* \left(W_\mu^+ \overline{N^c} \gamma^\mu P_L l_\alpha + \text{h.c.} \right) , \end{aligned} \tag{B.1.2}$$

for a sum over leptons $l_\alpha = e, \mu, \tau$, HNL-neutrino mixing angle U_α, and currents defined in eqs. (2.4.11) and (2.4.12).

Without considering the HNL interactions and using the equations-of-motion of the W bosons, it can be shown that $W_\mu^\pm$ can be replaced with $-\frac{1}{m_W^2}\frac{g}{\sqrt{2}}J_{W\mu}^\pm$ resulting in the point-like interaction between an HNL and three fermions,

$$\mathcal{L} \supset -\frac{g}{\sqrt{2}}U_\alpha^*\left[\left(-\frac{1}{m_W^2}\frac{g}{\sqrt{2}}J_W^{\mu+}\right)\overline{N^c}\gamma^\mu P_L l + \text{h.c.}\right] \propto G_F U_\alpha^*\left(\overline{N^c}\gamma^\mu P_L l\right)J_W^{\mu+}\,. \quad \text{(B.1.3)}$$

A similar procedure is carried out for the Z boson, and hence all 3-body decay channel widths in the remainder of this section will be proportional to $G_F^2|U_\alpha|^2$ [12]. The full derivation of the decay width formulas are beyond the scope of this thesis.

In the following section, the results from [70] will be stated; the decay width formula for each decay channel of HNLs with masses below 10 GeV.

B.2 Decays into Fermions

Neutrino-Only Decays

The decay width for neutrino-only HNL decays is given by

$$\Gamma(N \to \nu_\alpha \nu_\beta \overline{\nu}_\beta) = (1+\delta_{\alpha\beta})\frac{G_F^2 M_X^5}{768\pi^3}|U_\alpha|^2\,, \quad \text{(B.2.1)}$$

for HNL mass M_X and Fermi-constant G_F.

Charged Mediator Decays

For integrated out W boson mediators, the decay width for a charged mediator decaying into a lepton and two fermions is

$$\Gamma\left(N \to l_\alpha U\overline{D}\right) = N_W\frac{G_F^2 M_X^5}{192\pi^3}|U_\alpha|^2 I(x_u, x_d, x_l)\,, \quad \text{(B.2.2)}$$

for $x_i = \frac{m_i}{M_X}$ with masses m_i, $i \in \{l_\alpha, U, D\}$, and integral

$$I(x_u, x_d, x_l) = 12 \int_{(x_d+x_l)^2}^{(1-x_u)^2} \frac{dx}{x} \\ (x - x_l^2 - x_d^2)(1 + x_u^2 - x)\sqrt{\lambda(x, x_l^2, x_d^2)\lambda(1, x, x_u^2)}\,. \tag{B.2.3}$$

Here $U\overline{D}$ represents the two options of lepton-only ($\nu_\beta l_\beta^+$) and quark ($u_i \bar{d}_j$) final states, and the Kallen function is defined by

$$\lambda(a, b, c) = a^2 + b^2 + c^2 - 2\,(ab + bc + ac)\ . \tag{B.2.4}$$

N_W is a factor which for lepton-only final state $N_W = 1$ and for quarks is $N_W = N_c|V_{ij}|^2$ with the number of colours $N_c = 3$ and CKM matrix element V_{ij} for u_i and $\bar{d}_j$.

Neutral Mediator Decays

The decay width for neutral mediator decays, mediated by the integrated out Z boson, is defined

$$\Gamma\left(N \to \nu_\alpha f \overline{f}\right) = N_z \frac{G_F^2 M_X^5}{192\pi^3} |U_\alpha|^2 \\ \left[C_1^f \left(\left(1 - 14x^2 - 2x^4 - 12x^6\right) x_{1/2} + 12x^4(x^4 - 1)L(x) \right) \right. \\ \left. + 4C_2^f \left(x^2(2 + 10x^2 - 12x^4)x_{1/2} + 6x^4(1 - 2x^2 + 2x^4)L(x) \right) \right], \tag{B.2.5}$$

for $x = \frac{m_f}{M_X}$ with m_f the mass of the fermion, $x_{1/2} = \sqrt{1 - 4x^2}$, and

$$L(x) = \log\left(\frac{1 - 3x^2 - (1 - x^2)x_{1/2}}{x^2(1 + x_{1/2})} \right). \tag{B.2.6}$$

The factor N_Z is 1 for leptons and N_c for quarks, and the $C_{1,2}^f$ expressions are given in Table B.1 for up-type and down-type quarks, and for the two lepton scenarios respectively. s_W is the sine of the Weinberg angle θ_W.

f	C_1^f	C_f^2
u, c, t	$\frac{1}{4}\left(1 - \frac{8}{3}s_w^2 + \frac{32}{9}s_W^4\right)$	$\frac{1}{3}s_w^2\left(\frac{4}{3}s_w^2 - 1\right)$
d, s, b	$\frac{1}{4}\left(1 - \frac{4}{3}s_w^2 + \frac{8}{9}s_W^4\right)$	$\frac{1}{6}s_w^2\left(\frac{2}{3}s_w^2 - 1\right)$
$l_\beta, \beta \neq \alpha$	$\frac{1}{4}\left(1 - 4s_w^2 + 8s_W^4\right)$	$\frac{1}{2}s_w^2\left(2s_w^2 - 1\right)$
$l_\beta, \beta = \alpha$	$\frac{1}{4}\left(1 + 4s_w^2 + 8s_W^4\right)$	$\frac{1}{2}s_w^2\left(2s_w^2 + 1\right)$

Table B.1: $C_{1,2}^f$ expressions for fermions (From [70]).

B.3 Decays into Hadrons

For decays of heavy neutral leptons into a fermion and a meson, distinctions are made between pseudo-scalar and vector mesons. The decay width for decays into a charged pseudo-scalars and a lepton,

$$\Gamma(N \to l_\alpha^- h_P^+) = \frac{G_F^2 f_h^2 |V_{UD}|^2 |U_\alpha|^2 M_X^3}{16\pi} \left[(1 - x_l^2)^2 - x_h^2(1 + x_l^2)\right] \sqrt{\lambda(1, x_h^2, x_l^2)}\,, \tag{B.3.1}$$

depends on the decay constant of the charged pseudo-scalar meson f_h, and $x_i = \frac{m_i}{M_X}$ as defined above. V_{UD} is the CKM matrix element for the up- and down-type quarks in the pseudo-scalar, and m_h the mass of the meson. For a neutral pseudo-scalar mesons and a neutrino, the decay width is given by

$$\Gamma(N \to \nu_\alpha h_P^0) = \frac{G_F^2 f_h^2 M_X^3}{32\pi} |U_\alpha|^2 (1 - x_h^2)^2\,. \tag{B.3.2}$$

Similarly to charged pseudo-scalar mesons, the decay width into a charged vector meson and a lepton is

$$\Gamma(N \to l_\alpha^- h_V^+) = \frac{G_F^2 g_h^2 |V_{UD}|^2 |U_\alpha|^2 M_X^3}{16\pi m_h^2} \left[(1 - x_l^2)^2 + x_h^2(1 + x_l^2) - 2x_h^4\right] \sqrt{\lambda(1, x_h^2, x_l^2)}\,, \tag{B.3.3}$$

where g_h is the decay constant of the charged vector meson. Whereas for a neutral vector meson and a neutrino, the decay width is

$$\Gamma(N \to \nu_\alpha h_V^0) = \frac{G_F^2 \kappa_h^2 g_h^2 |U_\alpha|^2 M_X^3}{32\pi m_h^2}(1 - x_h^2)^2(1 + 2x_h^2)\,, \tag{B.3.4}$$

with the additional factor κ_h, which values for certain mesons can be found in Table B.2. Values for the decay constants for the various mesons can be found at [2].

h	ρ^0	ω	ϕ	J/ψ
κ_h	$1 - 2\sin\theta_W{}^2$	$\frac{4}{3}\sin\theta_W{}^2$	$\frac{4}{3}\sin\theta_W{}^2 - 1$	$1 - \frac{8}{3}\sin\theta_W{}^2$

Table B.2: κ_h expressions for four neutral vector mesons (From [70]).

B.4 Multi-Hadron Decays

The total hadronic decay width of HNLs is found using the decay width into quarks with a factor, which takes into account loop corrections. This factor, Δ_{QCD}, is taken from calculations of hadronic τ decays using

$$1 + \Delta_{\text{QCD}} = \frac{\Gamma(\tau \to \nu + \text{hadrons})}{\Gamma_{\text{tree}}(\tau \to \nu q\bar{q})}\,, \tag{B.4.1}$$

for quarks q. An additional suppression factor, $\sqrt{1 - 4m_K^2/M_X}$, is added for the s quark and any quarks with larger masses. The correction is given by

$$\Delta_{\text{QCD}} = \frac{\alpha_s}{\pi} + 5.2\left(\frac{\alpha_s}{\pi}\right)^2 + 26.4\left(\frac{\alpha_s}{\pi}\right)^3\,, \tag{B.4.2}$$

for $\alpha_s = \alpha_s(M_X)$, see section. 2.2.3 for the running of α_s[1].

The fully inclusive hadronic final state decay widths are constructed,

$$\Gamma^\nu_{\text{hadronic}} = (1 + \Delta_{\text{QCD}})\Gamma_{\text{tree}}(N \to \nu q\bar{q})\,, \tag{B.4.3}$$

[1]The running of α_s in HNL decays is carried out using `https://github.com/Hyperiso/Hyperiso` in this thesis.

$$\Gamma^{l_\alpha}_{\text{hadronic}} = (1 + \Delta_{\text{QCD}})\Gamma_{\text{tree}}(N \to l_\alpha u\overline{d})\,, \tag{B.4.4}$$

for decay width described above.

The decay of HNLs into multi-hadron states can be found by comparing the total hadronic width to the combined width of all decays into one meson [70]. Therefore, the widths for HNLs decays into multi-hadron final states are

$$\Gamma(N \to \nu \text{ multi-}h_{P,V}) = \Gamma^{\nu}_{\text{hadronic}} - \Gamma(N \to \nu h^0_{P,V})\,, \tag{B.4.5}$$

$$\Gamma(N \to l_\alpha \text{ multi-}h_{P,V}) = \Gamma^{l_\alpha}_{\text{hadronic}} - \Gamma(N \to l^{\mp}_\alpha h^{\pm}_{P,V})\,. \tag{B.4.6}$$

Appendix C

Proofs

C.1 Poisson & Gamma Distributions

In the following, the proof for the link between Poisson and gamma distribution functions is shown. The proof follows [145]. Starting from the incomplete gamma function,

$$\Gamma(y,\lambda) = \int_{\lambda}^{\infty} t^{y-1}e^{-t}dt \qquad \Rightarrow \qquad \Gamma(y+1,\lambda) = \int_{\lambda}^{\infty} t^{y}e^{-t}dt\,, \tag{C.1.1}$$

a change of variables is performed,

$$t = \lambda + u \qquad \Rightarrow \qquad \frac{\mathrm{d}\,t}{\mathrm{d}\,u} = 1 \qquad \Rightarrow \qquad \mathrm{d}\,t = \mathrm{d}\,u\,, \tag{C.1.2}$$

where when $t = \lambda$ then $u = 0$. Therefore, the integral becomes

$$\Gamma(y+1,\lambda) = \int_{0}^{\infty} (\lambda+u)^{y}e^{-(\lambda+u)}du = e^{-\lambda}\int_{0}^{\infty} (\lambda+u)^{y}e^{-u}du\,. \tag{C.1.3}$$

Using the Binomial theorem defined by

$$(x+y)^{n} = \sum_{k=0}^{n}\binom{n}{k}x^{n-k}y^{k}\,, \tag{C.1.4}$$

the integrand is rewritten,

$$\Gamma(y+1,\lambda) = e^{-\lambda}\int_{0}^{\infty}\sum_{k=0}^{y}\binom{y}{k}u^{y-k}\lambda^{k}e^{-u}du\,,$$

$$
\begin{aligned}
&= e^{-\lambda} \sum_{k=0}^{y} \binom{y}{k} \lambda^k \int_0^\infty u^{y-k} e^{-u} du \,, \\
&= e^{-\lambda} \sum_{k=0}^{y} \binom{y}{k} \lambda^k \, \Gamma(y-k+1) = e^{-\lambda} \sum_{k=0}^{y} \binom{y}{k} \lambda^k (y-k)! \,.
\end{aligned}
$$

Here, the definition of the gamma function,

$$
\Gamma(y) = \int_0^\infty u^{y-1} e^{-u} du = (y-1)! \,, \tag{C.1.5}
$$

has been used. Re-writing using, $\binom{n}{k} = \frac{n!}{k!(n-k)!}$, incomplete gamma function becomes

$$
\begin{aligned}
\Gamma(y+1,\lambda) &= e^{-\lambda} \sum_{k=0}^{y} \frac{y!}{k!} \lambda^k \,, \\
\Rightarrow \Gamma(y,\lambda) &= \sum_{k=0}^{y-1} \frac{(y-1)!}{k!} e^{-\lambda} \lambda^k = \sum_{k=0}^{y-1} \Gamma(y) \frac{e^{-\lambda} \lambda^k}{k!} \,.
\end{aligned} \tag{C.1.6}
$$

Therefore, it can be seen that the Poisson cumulative distribution function is given by the regularised upper gamma function.

Appendix D

Dark Matter Limits & Projections

D.1 Axion-Like Particles Limits & Projections

In the following, the current limits and projections for axion-like particles are displayed. The couplings on the figures are given in terms of $g_Y = \frac{c_f v_H}{f_a}$ and $f_G^{-1} = \frac{2\alpha_s c_{\tilde{G}}}{\pi f_a}$ for the couplings presented in section 4.2.3.

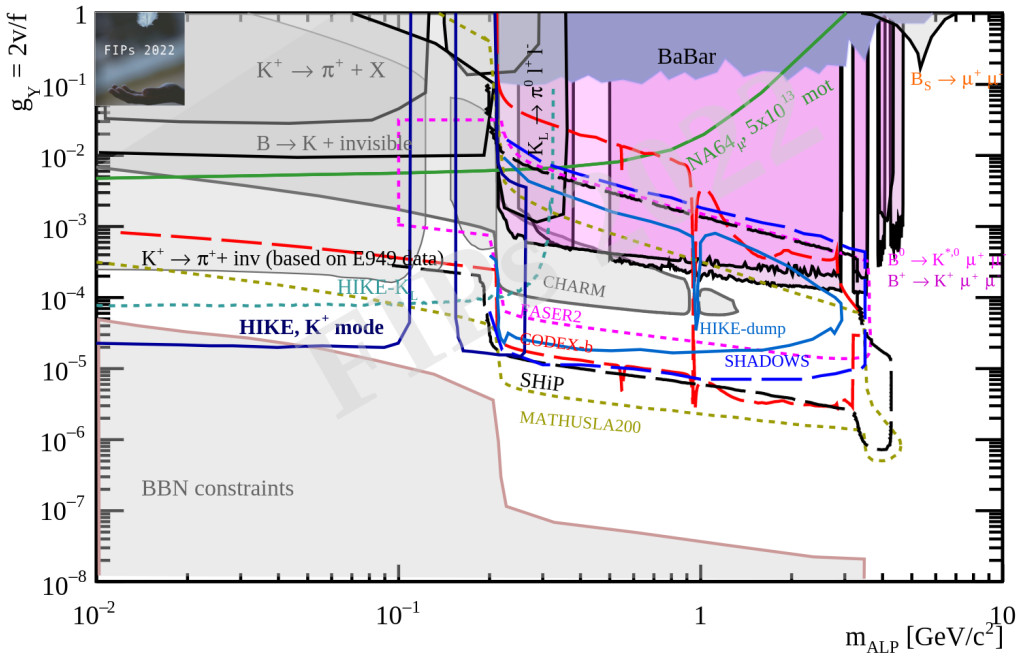

Figure D.1: Current limits and projections for the ALP-fermion coupling (From [54]).

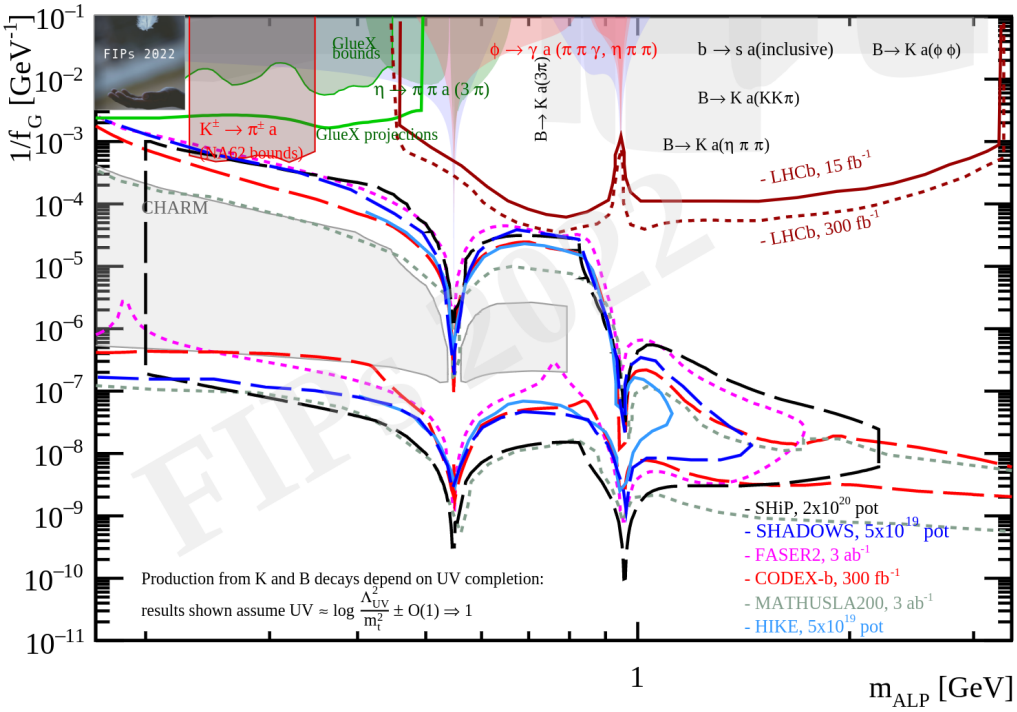

Figure D.2: Current limits and projections for the ALP-gluon coupling (From [54]).

D.2 Heavy-Neutral-Lepton Limits & Projections

In the following, the current limits and projections for heavy neutral leptons are displayed. The couplings on the figures are the same as the ones described in section 4.2.4.

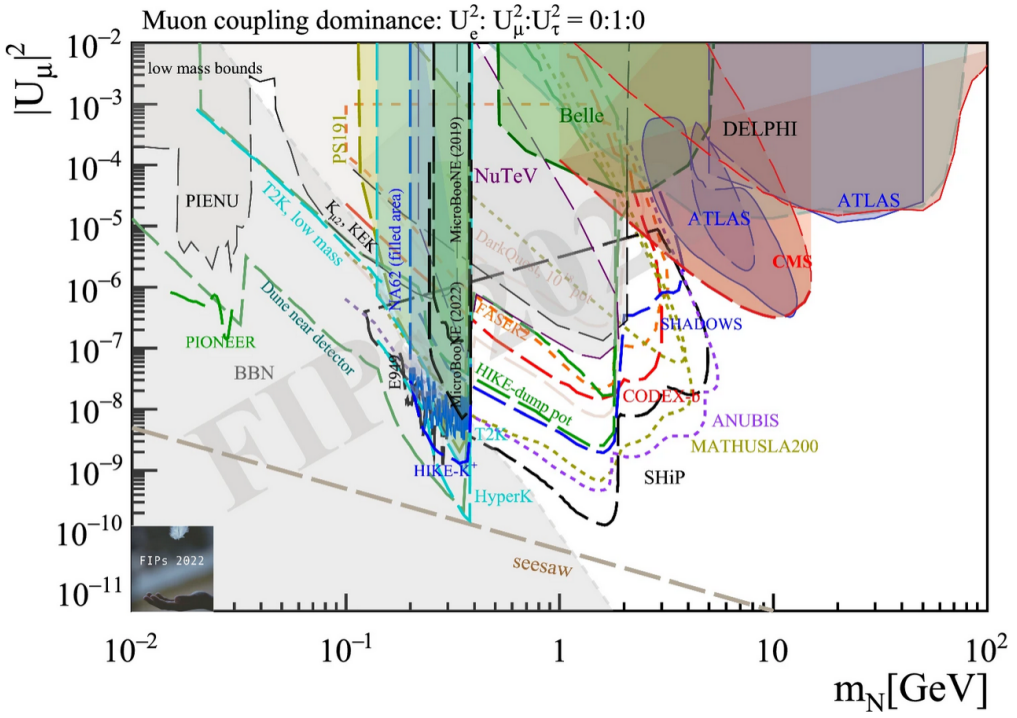

Figure D.3: Current limits and projections on minimal HNL models for muon-dominated mixing (From [54]).

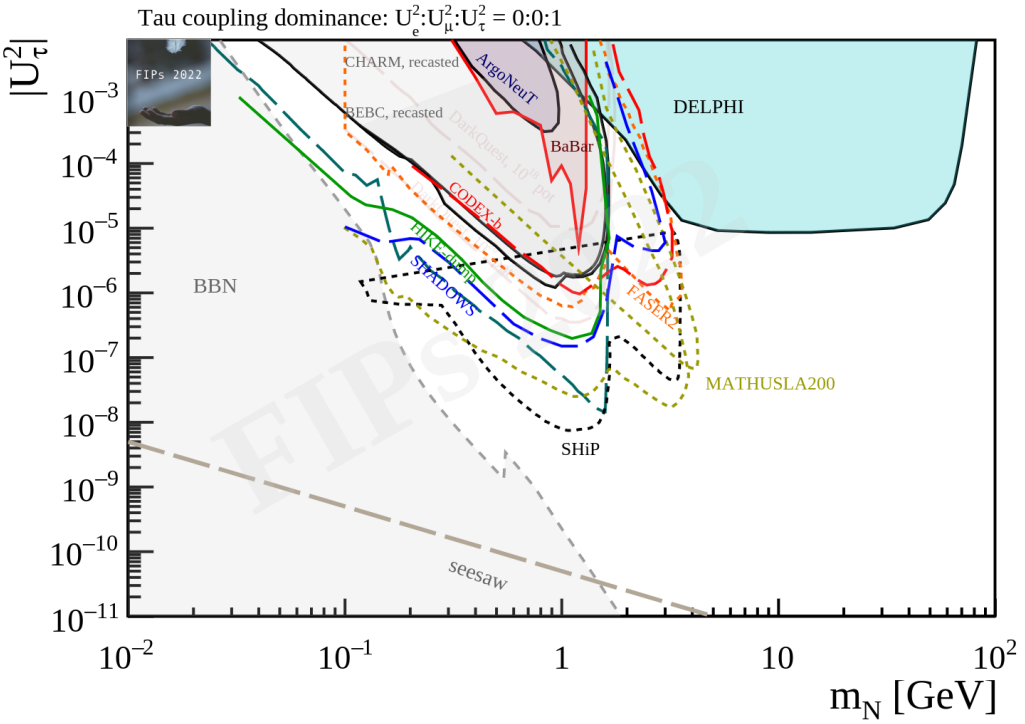

Figure D.4: Current limits and projections on minimal HNL models for tau-dominated mixing (From [54]).

Appendix E

Standard Model Background

In the following, the individual $\theta_{\text{lab}} - E_{\text{CMS}}$ distributions for the four distinct contributions to the SM background discussed in section 6.4.1 are displayed. Each distribution has an individual colour coding. The explanation for the features of each distribution can be found in the aforementioned section.

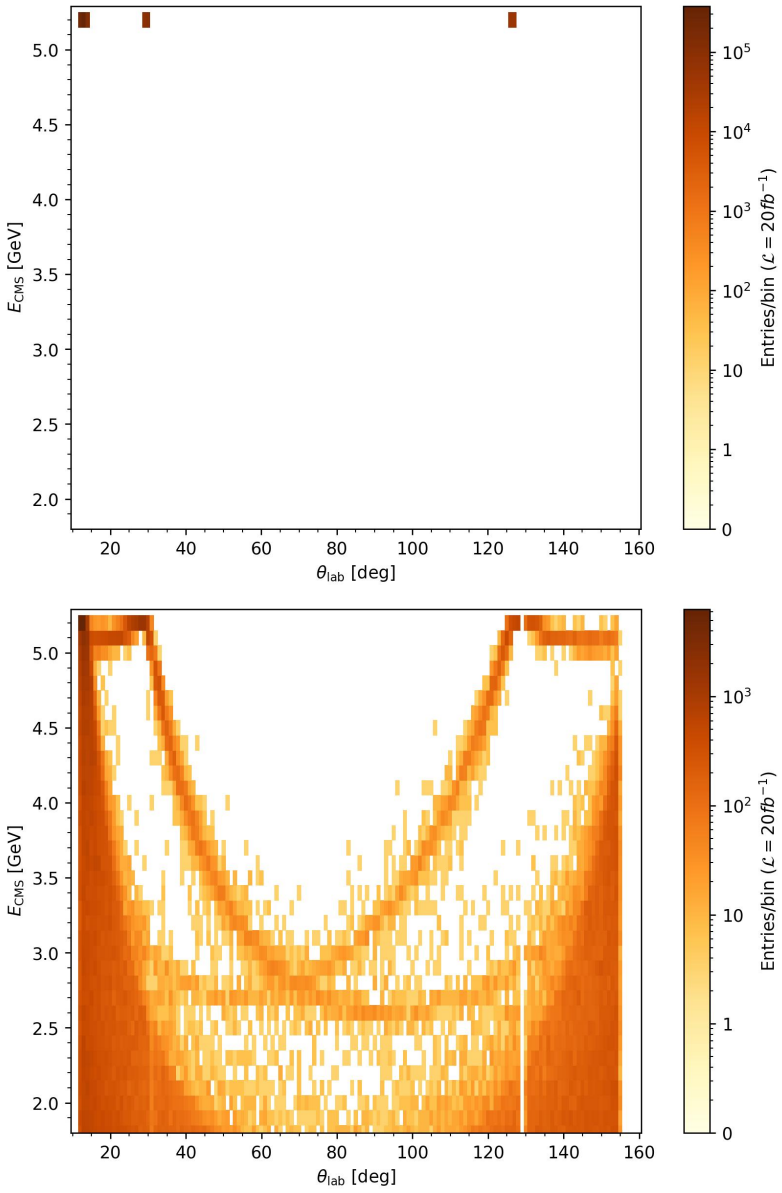

Figure E.1: SM background distributions for $e^+e^- \to \gamma\gamma$ (top) and $\gamma\gamma\gamma$ (bottom).

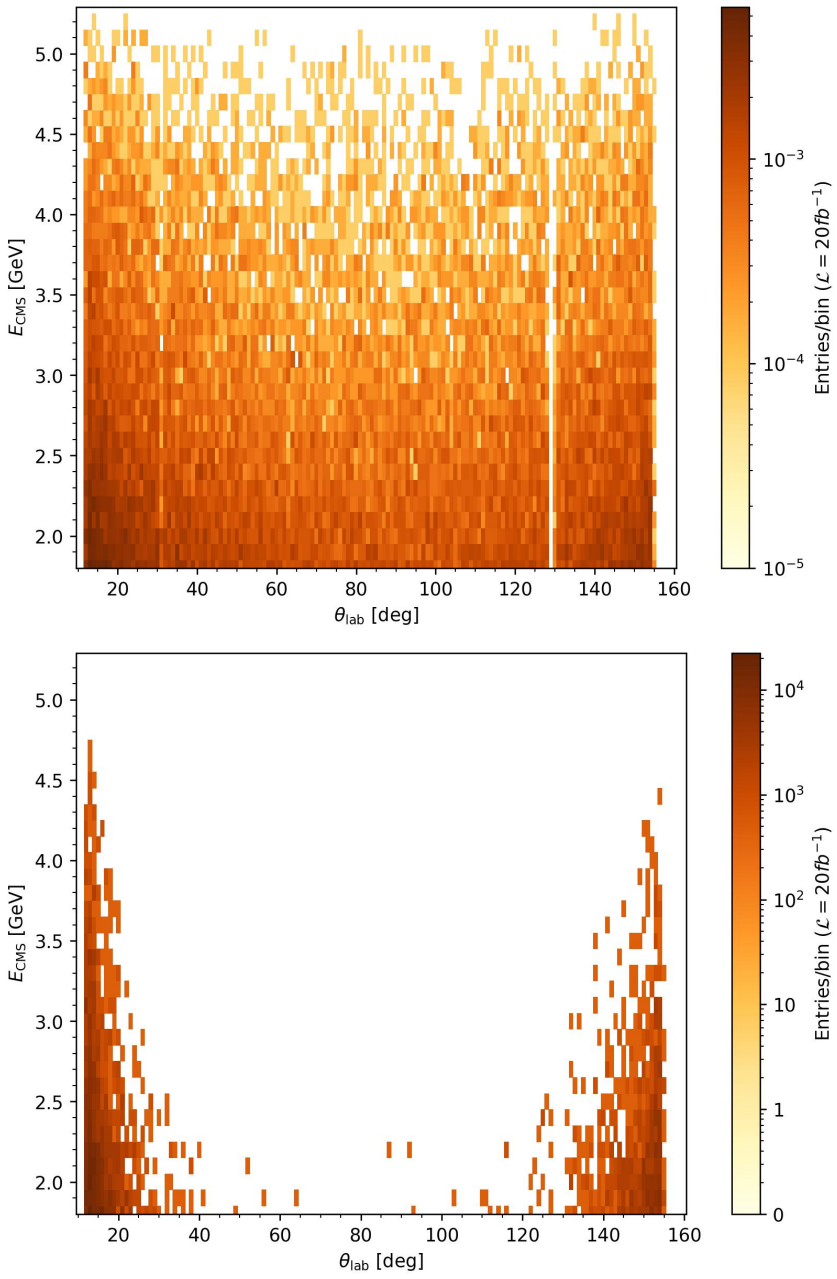

Figure E.2: SM background distributions for $\nu\bar{\nu}\gamma(\gamma)$ (top) and $e^+e^-\gamma(\gamma)$ (bottom).

Bibliography

[1] M. Bauer and S. N. Erner, *How to measure the spin of invisible states in* $e^+e^- \to \gamma + X$, [2308.09746].

[2] Particle Data Group collaboration, P. Zyla et al., *Review of particle physics*, *PTEP* (2020) 083C01.

[3] L. Hoddeson, *The rise of the standard model : particle physics in the 1960s and 1970s*. Cambridge University Press, Cambridge, 1997.

[4] Super-Kamiokande collaboration, Y. Fukuda et al., *Evidence for oscillation of atmospheric neutrinos*, *Phys. Rev. Lett.* **81** (1998) 1562–1567, [hep-ex/9807003].

[5] A. Arbey and F. Mahmoudi, *Dark matter and the early Universe: a review*, *Prog. Part. Nucl. Phys.* **119** (2021) 103865, [2104.11488].

[6] K. N. Abazajian et al., *Inflation Physics from the Cosmic Microwave Background and Large Scale Structure*, *Astropart. Phys.* **63** (2015) 55–65, [1309.5381].

[7] J. Beacham et al., *Physics Beyond Colliders at CERN: Beyond the Standard Model Working Group Report*, *J. Phys. G* **47** (2020) 010501, [1901.09966].

[8] C. P. Burgess, *Introduction to Effective Field Theory*, *Ann. Rev. Nucl. Part. Sci.* **57** (2007) 329–362, [hep-th/0701053].

[9] A. M. Green, *Dark matter in astrophysics/cosmology*, *SciPost Phys. Lect. Notes* **37** (2022) 1, [2109.05854].

[10] L. J. Hall, K. Jedamzik, J. March-Russell and S. M. West, *Freeze-In Production of FIMP Dark Matter*, *JHEP* **03** (2010) 080, [0911.1120].

[11] J. I. Read, *The Local Dark Matter Density*, *J. Phys. G* **41** (2014) 063101, [1404.1938].

[12] M. E. Peskin and D. V. Schroeder, *An Introduction to quantum field theory*. Addison-Wesley, Reading, USA, 1995.

[13] C. Burgess and G. Moore, *The Standard Model: A Primer*. Cambridge University Press, 2006, 10.1017/CBO9780511819698.

[14] W. Foundation, "Standard model." https://en.wikipedia.org/wiki/Standard_Model, Accessed: 02/01/2024.

[15] J. C. Romao and J. P. Silva, *A resource for signs and Feynman diagrams of the Standard Model*, *Int. J. Mod. Phys. A* **27** (2012) 1230025, [1209.6213].

[16] M. D. Schwartz, *Quantum field theory and the standard model*. Cambridge University Press, Cambridge, 2014.

[17] D. Barry, J.-Y. Parlange, L. Li, H. Prommer, C. Cunningham and F. Stagnitti, *Analytical approximations for real values of the lambert w-function*, *Mathematics and Computers in Simulation* **53** (2000) 95–103.

[18] A. Deur, S. J. Brodsky and G. F. de Teramond, *The QCD Running Coupling*, *Nucl. Phys.* **90** (2016) 1, [1604.08082].

[19] H. E. Haber, *Spin formalism and applications to new physics searches*, in *21st Annual SLAC Summer Institute on Particle Physics: Spin Structure in High-energy Processes (School: 26 Jul - 3 Aug, Topical Conference: 4-6 Aug) (SSI 93)*, pp. 231–272, 4, 1994, hep-ph/9405376.

[20] G. Moortgat-Pick et al., *The Role of polarized positrons and electrons in revealing fundamental interactions at the linear collider*, *Phys. Rept.* **460** (2008) 131–243, [hep-ph/0507011].

[21] K. Hagiwara, R. Peccei, D. Zeppenfeld and K. Hikasa, *Probing the weak boson sector in $e^+e^- \to w^+w^-$*, *Nuclear Physics B* **282** (1987) 253–307.

[22] J. F. e. a. Gunion, *The Higgs hunter's guide*. Frontiers in physics ; 80. Addison-Wesley, Redwood City, Calif. ;, 1990.

[23] M. E. Peskin, *Lectures on the Theory of the Weak Interaction*, in *2016 European School of High-Energy Physics*, pp. 1–70, 2017, 1708.09043, DOI.

[24] I. Sample, *The long story of how the boson got only Higgs's name*, *Nature* **466** (2010) 689.

[25] A. Atre, T. Han, S. Pascoli and B. Zhang, *The Search for Heavy Majorana Neutrinos*, *JHEP* **05** (2009) 030, [0901.3589].

[26] UC Riverside; Department of Mathematics collaboration, J. Baez, 12, 2020. https://math.ucr.edu/home//baez/neutrinos.html.

[27] I. Esteban, M. C. Gonzalez-Garcia, M. Maltoni, T. Schwetz and A. Zhou, *The fate of hints: updated global analysis of three-flavor neutrino oscillations*, *JHEP* **09** (2020) 178, [2007.14792].

[28] A. Buckley, C. White and M. White, *Practical Collider Physics*. IOP, 12, 2021, 10.1088/978-0-7503-2444-1.

[29] H. Schmickler, *Colliders*, [2011.01638].

[30] A. Alloul, N. D. Christensen, C. Degrande, C. Duhr and B. Fuks, *FeynRules 2.0 - A complete toolbox for tree-level phenomenology*, *Comput. Phys. Commun.* **185** (2014) 2250–2300, [1310.1921].

[31] T. Bandyopadhyay, S. Chakraborty and S. Trifinopoulos, *Displaced searches for light vector bosons at Belle II*, *JHEP* **05** (2022) 141, [2203.03280].

[32] W. Commons, *Main page — wikimedia commons, the free media repository*, 2024. https://commons.wikimedia.org/w/index.php?title=Main_Page&oldid=847663279, [Online; accessed 26-February-2024].

[33] B. Batell, M. Pospelov and A. Ritz, *Probing a secluded u(1) at b-factories*, *Physical Review D* **79** (7, 2009) .

[34] V. Shiltsev and F. Zimmermann, *Modern and Future Colliders*, *Rev. Mod. Phys.* **93** (2021) 015006, [2003.09084].

[35] C. Bierlich, S. Chakraborty, N. Desai, L. Gellersen, I. Helenius, P. Ilten et al., *A comprehensive guide to the physics and usage of pythia 8.3*, .

[36] J. Alwall, R. Frederix, S. Frixione, V. Hirschi, F. Maltoni, O. Mattelaer et al., *The automated computation of tree-level and next-to-leading order differential cross sections, and their matching to parton shower simulations*, *JHEP* **07** (2014) 079, [1405.0301].

[37] A. Papaefstathiou, *How-to: write a parton-level Monte Carlo particle physics event generator*, *Eur. Phys. J. Plus* **135** (2020) 497, [1412.4677].

[38] A. Accardi, D. M. Asner, H. Atmacan, R. Baartman, S. Banerjee, A. Beaubien et al., *Snowmass 2021 white paper on upgrading superkekb with a polarized electron beam: Discovery potential and proposed implementation*, .

[39] R. Siemann, *B factories*, *Conf. Proc. C* **910625** (1991) 497–501.

[40] E. K. et al, *The belle II physics book*, *Progress of Theoretical and Experimental Physics* **2019** (12, 2019) .

[41] S. Robertson, *The belle ii experiment*, *Journal of Physics: Conference Series* **1271** (07, 2019) 012011.

[42] SuperB Collaboration, M. E. Biagini, P. Raimondi and J. Seeman, *Superb progress reports – accelerator*, .

[43] US Belle II Group, Belle II/SuperKEKB e^- Polarization Upgrade Working Group collaboration, D. M. Asner et al., *Snowmass 2021 White Paper on Upgrading SuperKEKB with a Polarized Electron Beam: Discovery Potential and Proposed Implementation*, in *Snowmass 2021*, 5, 2022, 2205.12847.

[44] A. Aleksejevs, S. Barkanova, C. Miller, J. M. Roney and V. Zykunov, *NLO radiative corrections for Forward-Backward and Left-Right Asymmetries at a B-Factory*, *Phys. Rev. D* **101** (2020) 053003, [1801.08510].

[45] ATLAS collaboration, *ATLAS: Letter of intent for a general purpose pp experiment at the large hadron collider at CERN*, 1992. http://cds.cern.ch/record/291061.

[46] J. Pequenao and P. Schaffner, *How atlas detects particles: Diagram of particle paths in the detector*, 1, 2013. https://cds.cern.ch/record/1505342, Accessed: 02/01/2024.

[47] ATLAS collaboration, G. Aad et al., *Standalone vertex finding in the ATLAS muon spectrometer*, *JINST* **9** (2014) P02001, [1311.7070].

[48] T. P. Satterthwaite, *Sensitivity of the anubis and atlas detectors to neutral long-lived particles produced in pp collisions at the large hadron collider*, 2022. https://cds.cern.ch/record/2839063.

[49] C. O'Hare, "cajohare/axionlimits: Axionlimits." https://cajohare.github.io/AxionLimits/, July, 2020. 10.5281/zenodo.3932430.

[50] X. Calmet and F. Kuipers, *Theoretical bounds on dark matter masses*, *Phys. Lett. B* **814** (2021) 136068, [2009.11575].

[51] (DEAP Collaboration)‡, DEAP collaboration, P. Adhikari et al., *First Direct Detection Constraints on Planck-Scale Mass Dark Matter with Multiple-Scatter Signatures Using the DEAP-3600 Detector*, *Phys. Rev. Lett.* **128** (2022) 011801, [2108.09405].

[52] A. V. Manohar, *Introduction to Effective Field Theories*, [1804.05863].

[53] B. Batell, M. Pospelov and A. Ritz, *Exploring Portals to a Hidden Sector Through Fixed Targets*, *Phys. Rev. D* **80** (2009) 095024, [0906.5614].

[54] C. Antel et al., *Feebly Interacting Particles: FIPs 2022 workshop report*, *Eur. Phys. J. C* **83** (2023) 1122, [2305.01715].

[55] M. Fabbrichesi, E. Gabrielli and G. Lanfranchi, *The Dark Photon*, [2005.01515].

[56] T. Araki, S. Hoshino, T. Ota, J. Sato and T. Shimomura, *Detecting the $l_\mu - l_\tau$ gauge boson at belle II*, *Physical Review D* **95** (3, 2017) .

[57] M. Bauer, P. Foldenauer and J. Jaeckel, *Hunting all the hidden photons*, *Journal of High Energy Physics* **2018** (7, 2018) .

[58] M. Bauer, P. Foldenauer and J. Jaeckel, *Hunting all the hidden photons*, *Journal of High Energy Physics* **2018** (7, 2018) .

[59] M. Duerr, T. Ferber, C. Hearty, F. Kahlhoefer, K. Schmidt-Hoberg and P. Tunney, *Invisible and displaced dark matter signatures at Belle II*, *JHEP* **02** (2020) 039, [1911.03176].

[60] I. G. Irastorza, *An introduction to axions and their detection*, *SciPost Physics Lecture Notes* (3, 2022) .

[61] I. Brivio, M. B. Gavela, L. Merlo, K. Mimasu, J. M. No, R. del Rey et al., *Alps effective field theory and collider signatures*, *The European Physical Journal C* **77** (8, 2017) .

[62] M. Bauer, M. Neubert, S. Renner, M. Schnubel and A. Thamm, *The Low-Energy Effective Theory of Axions and ALPs*, *JHEP* **04** (2021) 063, [2012.12272].

[63] M. Bauer, M. Neubert and A. Thamm, *Collider Probes of Axion-Like Particles*, *JHEP* **12** (2017) 044, [1708.00443].

[64] E. K. Akhmedov, G. C. Branco and M. N. Rebelo, *Seesaw mechanism and structure of neutrino mass matrix*, *Phys. Lett. B* **478** (2000) 215–223, [hep-ph/9911364].

[65] C. Amsler, *Nuclear and Particle Physics*. 2053-2563. IOP Publishing, 2015, 10.1088/978-0-7503-1140-3.

[66] S. Bilenky, *Seesaw Mechanism of the Neutrino Mass Generation*, pp. 79–88. Springer International Publishing, Cham, 2018. 10.1007/978-3-319-74802-3_5.

[67] S. Alekhin et al., *A facility to Search for Hidden Particles at the CERN SPS: the SHiP physics case*, *Rept. Prog. Phys.* **79** (2016) 124201, [1504.04855].

[68] M. Chianese, D. F. G. Fiorillo, G. Miele and S. Morisi, *Investigating two heavy neutral leptons neutrino seesaw mechanism at SHiP*, *Int. J. Mod. Phys. A* **34** (2019) 1950047, [1812.01994].

[69] C. Degrande, O. Mattelaer, R. Ruiz and J. Turner, *Fully-Automated Precision Predictions for Heavy Neutrino Production Mechanisms at Hadron Colliders*, *Phys. Rev. D* **94** (2016) 053002, [1602.06957].

[70] K. Bondarenko, A. Boyarsky, D. Gorbunov and O. Ruchayskiy, *Phenomenology of GeV-scale Heavy Neutral Leptons*, *JHEP* **11** (2018) 032, [1805.08567].

[71] P. Coloma, E. Fernández-Martínez, M. González-López, J. Hernández-García and Z. Pavlovic, *GeV-scale neutrinos: interactions with mesons and DUNE sensitivity*, *Eur. Phys. J. C* **81** (2021) 78, [2007.03701].

[72] F. S. Queiroz, *Dark Matter Overview: Collider, Direct and Indirect Detection Searches*, in *51st Rencontres de Moriond on EW Interactions and Unified Theories*, pp. 427–436, ARISF, 2016, 1605.08788.

[73] MATHUSLA collaboration, H. Lubatti et al., *Explore the lifetime frontier with MATHUSLA*, *JINST* **15** (2020) C06026, [1901.04040].

[74] FASER collaboration, A. Ariga et al., *Technical Proposal for FASER: ForwArd Search ExpeRiment at the LHC*, [1812.09139].

[75] G. Aielli et al., *Expression of interest for the CODEX-b detector*, *Eur. Phys. J. C* **80** (2020) 1177, [1911.00481].

[76] D. D. Wackerly, W. Mendenhall and R. L. Scheaffer, *Mathematical statistics with applications*. Thomson Brooks/Cole, Belmont, CA, 7th ed. ed., 2008.

[77] T. Junk, *Confidence level computation for combining searches with small statistics*, *Nucl. Instrum. Meth. A* **434** (1999) 435–443, [hep-ex/9902006].

[78] B. Batell, N. Blinov, C. Hearty and R. McGehee, *Exploring Dark Sector Portals with High Intensity Experiments*, in *Snowmass 2021*, 7, 2022, 2207.06905.

[79] K. Jedamzik and M. Pospelov, *Big Bang Nucleosynthesis and Particle Dark Matter*, *New J. Phys.* **11** (2009) 105028, [0906.2087].

[80] J.-T. Li, G. M. Fuller and E. Grohs, *Probing dark photons in the early universe with big bang nucleosynthesis*, *JCAP* **12** (2020) 049, [2009.14325].

[81] P. Coloma, J. López-Pavón, L. Molina-Bueno and S. Urrea, *New physics searches using ProtoDUNE and the CERN SPS accelerator*, *JHEP* **01** (2024) 134, [2304.06765].

[82] M. Bauer, O. Brandt, L. Lee and C. Ohm, *ANUBIS: Proposal to search for long-lived neutral particles in CERN service shafts*, [1909.13022].

[83] CERN, "ANUBIS Website." https://twiki.cern.ch/twiki/bin/view/ANUBIS/, Accessed: 02/01/2024.

[84] *ANUBIS: a guide into the dark sector*, 6, 2023. https://ep-news.web.cern.ch/content/anubis-guide-dark-sector, Accessed: 02/01/2024.

[85] ANUBIS collaboration, A. Shah, *Searches for long-lived particles with the ANUBIS experiment*, [2401.11604].

[86] R. Beltrán, J. Günther, M. Hirsch, A. Titov and Z. S. Wang, *Heavy neutral leptons from kaons in effective field theory*, [2309.11546].

[87] Y.-n. Mao, K. Wang and Z. S. Wang, *Can we discover lepton number violation with the LHC far detectors?*, *Phys. Rev. D* **108** (2023) 095025, [2305.03908].

[88] J. De Vries, H. K. Dreiner, J. Y. Günther, Z. S. Wang and G. Zhou, *Long-lived Sterile Neutrinos at the LHC in Effective Field Theory*, *JHEP* **03** (2021) 148, [2010.07305].

[89] G. Cottin, J. C. Helo, M. Hirsch, A. Titov and Z. S. Wang, *Heavy neutral leptons in effective field theory and the high-luminosity LHC*, *JHEP* **09** (2021) 039, [2105.13851].

[90] H. K. Dreiner, J. Y. Günther and Z. S. Wang, *R-parity violation and light neutralinos at ANUBIS and MAPP*, *Phys. Rev. D* **103** (2021) 075013, [2008.07539].

[91] E. Bertuzzo, A. Scaffidi and M. Taoso, *Searching for inelastic dark matter with future LHC experiments*, *JHEP* **08** (2022) 100, [2201.12253].

[92] M. Hirsch and Z. S. Wang, *Heavy neutral leptons at ANUBIS*, *Phys. Rev. D* **101** (2020) 055034, [2001.04750].

[93] C. Degrande, C. Duhr, B. Fuks, D. Grellscheid, O. Mattelaer and T. Reiter, *UFO - The Universal FeynRules Output*, *Comput. Phys. Commun.* **183** (2012) 1201–1214, [1108.2040].

[94] W. R. Inc., "Mathematica, Version 14.0." https://www.wolfram.com/mathematica, Champaign, IL, 2024.

[95] SHiP collaboration, **SHiP** Collaboration, "*FairShip*." https://github.com/ShipSoft/FairShip.

[96] M. Cacciari, G. P. Salam and G. Soyez, *FastJet User Manual*, *Eur. Phys. J. C* **72** (2012) 1896, [1111.6097].

[97] W. Abdallah, A. Hammad, A. Kasem and S. Khalil, *Long-lived B-L symmetric SSM particles at the LHC*, *Phys. Rev. D* **98** (2018) 095019, [1804.09778].

[98] I. Krasnov, *DUNE prospects in the search for sterile neutrinos*, *Phys. Rev. D* **100** (2019) 075023, [1902.06099].

[99] D. Dercks, J. De Vries, H. K. Dreiner and Z. S. Wang, *R-parity Violation and Light Neutralinos at CODEX-b, FASER, and MATHUSLA*, *Phys. Rev. D* **99** (2019) 055039, [1810.03617].

[100] E. K. et al, *The belle II physics book*, *Progress of Theoretical and Experimental Physics* **2019** (12, 2019) .

[101] F. Wilczek, *Decays of heavy vector mesons into higgs particles*, *Phys. Rev. Lett.* **39** (Nov, 1977) 1304–1306.

[102] R. e. a. Balest, Υ*(1s)*$\rightarrow\gamma$*+noninteracting particles*, *Phys. Rev. D* **51** (Mar, 1995) 2053–2060.

[103] BaBar collaboration, B. Aubert et al., *Search for Invisible Decays of a Light Scalar in Radiative Transitions* $v_{3S} \rightarrow \gamma$ *A0*, in *34th International Conference on High Energy Physics*, 7, 2008, 0808.0017.

[104] BABAR Collaboration collaboration, del Amo Sanchez et al., *Search for production of invisible final states in single-photon decays of $\Upsilon(1s)$*, *Phys. Rev. Lett.* **107** (Jul, 2011) 021804.

[105] M. J. Dolan, T. Ferber, C. Hearty, F. Kahlhoefer and K. Schmidt-Hoberg, *Revised constraints and belle II sensitivity for visible and invisible axion-like particles*, *Journal of High Energy Physics* **2017** (12, 2017) .

[106] L. Darmé, F. Giacchino, E. Nardi and M. Raggi, *Invisible decays of axion-like particles: constraints and prospects*, *JHEP* **06** (2021) 009, [2012.07894].

[107] Belle-II collaboration, L. Aggarwal et al., *Snowmass White Paper: Belle II physics reach and plans for the next decade and beyond*, [2207.06307].

[108] BaBar collaboration, J. P. Lees et al., *Search for invisible decays of a dark photon produced in e^+e^- collisions at babar*, *Phys. Rev. Lett.* **119** (2017) 131804, [1702.03327].

[109] B. Holdom, *Two U(1)'s and Epsilon Charge Shifts*, *Phys. Lett. B* **166** (1986) 196–198.

[110] R. Foot, *New Physics From Electric Charge Quantization?*, *Mod. Phys. Lett. A* **6** (1991) 527–530.

[111] X. G. He, G. C. Joshi, H. Lew and R. R. Volkas, *NEW Z-prime PHENOMENOLOGY*, *Phys. Rev. D* **43** (1991) 22–24.

[112] X.-G. He, G. C. Joshi, H. Lew and R. R. Volkas, *Simplest Z-prime model*, *Phys. Rev. D* **44** (1991) 2118–2132.

[113] M. Bauer and P. Foldenauer, *Consistent Theory of Kinetic Mixing and the Higgs Low-Energy Theorem*, *Phys. Rev. Lett.* **129** (2022) 171801, [2207.00023].

[114] V. Shtabovenko, R. Mertig and F. Orellana, *FeynCalc 9.3: New features and improvements*, *Computer Physics Communications* **256** (11, 2020) 107478.

[115] Belle-II collaboration, F. Forti, *Snowmass Whitepaper: The Belle II Detector Upgrade Program*, in *Snowmass 2021*, 3, 2022, 2203.11349.

[116] F.-F. Lee, G.-L. Lin and V. Q. Nhat, *Polarization effects in the search for dark vector boson at e^+e^- colliders*, *Phys. Rev. D* **103** (2021) 015016, [2008.07769].

[117] F. M. Renard, *Tests of Neutral Gauge Boson Selfcouplings With $e^+e^- \to \gamma Z$*, *Nucl. Phys. B* **196** (1982) 93–108.

[118] K.-i. Hikasa, *Transverse Polarization Effects in e^+e^- Collisions: The Role of Chiral Symmetry*, *Phys. Rev. D* **33** (1986) 3203.

[119] B. Ananthanarayan and S. D. Rindani, *Transverse beam polarization and CP violation in $e^+e^- \to \gamma Z$ with contact interactions*, *Phys. Lett. B* **606** (2005) 107–115, [hep-ph/0410084].

[120] M. Wakai, *Search for invisible decays of dark photon at belle ii*, 10, 2021. https://open.library.ubc.ca/media/stream/pdf/24/1.0402550/4.

[121] I. Brivio, M. B. Gavela, L. Merlo, K. Mimasu, J. M. No, R. del Rey et al., "Effective theories for a light axion-light-particle (alp)." http://feynrules.irmp.ucl.ac.be/wiki/ALPsEFT.

[122] W. Liu and L. Basso, "B-l-sm – feynrules." http://feynrules.irmp.ucl.ac.be/wiki/B-L-SM#no1.

[123] S. Amrith, J. M. Butterworth, F. F. Deppisch, W. Liu, A. Varma and D. Yallup, *LHC constraints on a b - l gauge model using contur*, *Journal of High Energy Physics* **2019** (5, 2019) , [1811.11452].

[124] F. F. Deppisch, W. Liu and M. Mitra, *Long-lived heavy neutrinos from higgs decays*, *Journal of High Energy Physics* **2018** (8, 2018) , [1804.04075].

[125] W. R. Inc., "Mathematica, Version 14.0." https://www.wolfram.com/mathematica, Champaign, IL, 2024.

[126] Belle collaboration, H. Ikeda et al., *A detailed test of the CsI(Tl) calorimeter for BELLE with photon beams of energy between 20-MeV and 5.4-GeV*, *Nucl. Instrum. Meth. A* **441** (2000) 401–426.

[127] LHCb collaboration, R. Aaij et al., *Measurement of the photon polarization in $\Lambda_b^0 \to \Lambda\ \gamma$ decays*, *Phys. Rev. D* **105** (2022) L051104, [2111.10194].

[128] H. Davoudiasl, H.-S. Lee and W. J. Marciano, *Muon $g-2$, rare kaon decays, and parity violation from dark bosons*, *Phys. Rev. D* **89** (2014) 095006, [1402.3620].

[129] R. Essig, J. Mardon, M. Papucci, T. Volansky and Y.-M. Zhong, *Constraining light dark matter with low-energy e^+e^- colliders*, *JHEP* **11** (2, 2013) 167, [1309.5084].

[130] E787 collaboration, S. Adler et al., *Further search for the decay $K^+ \to \pi + \nu\bar{\nu}$ in the momentum region $P < 195 MeV/c$*, *Phys. Rev. D* **70** (2004) 037102, [hep-ex/0403034].

[131] BNL-E949 collaboration, A. V. Artamonov et al., *Study of the decay $K^+ \to \pi^+\nu\bar{\nu}$ in the momentum region $140 < P_\pi < 199$ MeV/c*, *Phys. Rev. D* **79** (2009) 092004, [0903.0030].

[132] D. Banerjee et al., *Dark matter search in missing energy events with NA64*, *Phys. Rev. Lett.* **123** (2019) 121801, [1906.00176].

[133] P. J. Fox, R. Harnik, J. Kopp and Y. Tsai, *LEP Shines Light on Dark Matter*, *Phys. Rev. D* **84** (2011) 014028, [1103.0240].

[134] DELPHI collaboration, J. Abdallah et al., *Search for one large extra dimension with the DELPHI detector at LEP*, *Eur. Phys. J. C* **60** (2009) 17–23, [0901.4486].

[135] J. H. Chang, R. Essig and S. D. McDermott, *Revisiting Supernova 1987A Constraints on Dark Photons*, *JHEP* **01** (2017) 107, [1611.03864].

[136] G. Lucente and P. Carenza, *Supernova bound on axionlike particles coupled with electrons*, *Phys. Rev. D* **104** (2021) 103007, [2107.12393].

[137] GERDA collaboration, M. Agostini et al., *First Search for Bosonic Superweakly Interacting Massive Particles with Masses up to 1 MeV/c^2 with GERDA*, *Phys. Rev. Lett.* **125** (2020) 011801, [2005.14184].

[138] EDELWEISS collaboration, E. Armengaud et al., *Searches for electron interactions induced by new physics in the EDELWEISS-III Germanium bolometers*, *Phys. Rev. D* **98** (2018) 082004, [1808.02340].

[139] M. Bauer, M. Neubert, S. Renner, M. Schnubel and A. Thamm, *Flavor probes of axion-like particles*, *JHEP* **09** (2022) 056, [2110.10698].

[140] NA64 Collaboration collaboration, D. Banerjee, J. Bernhard, V. E. Burtsev, A. G. Chumakov, D. Cooke, P. Crivelli et al., *Search for axionlike and scalar particles with the na64 experiment*, *Phys. Rev. Lett.* **125** (Aug, 2020) 081801.

[141] EIC collaboration, A. Deshpande, *Physics of an Electron Ion Collider*, *Nucl. Phys. A* **904-905** (2013) 302c–309c.

[142] M. W. Winkler, *Decay and detection of a light scalar boson mixing with the higgs boson*, *Physical Review D* **99** (Jan., 2019) .

[143] F. Bezrukov and D. Gorbunov, *Light inflaton Hunter's Guide*, *JHEP* **05** (2010) 010, [0912.0390].

[144] D. B. Kaplan, *Five lectures on effective field theory*, 2005.

[145] G. J. O. Jameson, *The incomplete gamma functions*, *The Mathematical Gazette* **100** (2016) 298–306.